Development of a DFIG Wind Energy System for Grid Integration Studies

By: Manuella Maria Amilha D'Oliviera Pio

Supervised by: **Associate Professor Azeem Khan**

Co-Supervised by: **Associate Professor Paul Barendse**

A thesis submitted in fulfilment of the requirements for the degree of

Master of Science in Electrical Engineering at the University of Cape Town

October 2013

Declaration

I declare that this is my own work. Information and research gathered and used has been properly referenced.

This thesis is being submitted for the degree of Masters of Science in Engineering at the University of Cape Town.

This thesis has not been submitted for any other degree or examination in another university.

Manuella Maria Amilha D'Oliviera Pio .....

Signed by candidate

Signature Removed

Date: October 2013

ACKNOWLEDGEMENTS

All the glory goes to my Lord Jesus Christ for granting me the opportunity and capability to complete my Master's degree.

Special thanks go to my mum, Elizabeth, for always being there for me and for your support and advice and earnest prayers. I would also like to thank the rest of my family for being there for me always.

My appreciation and many thanks go to my supervisor Associate Professor Azeem Khan for his patience, guidance, encouragement and financial support throughout my degree. Thanks also to my co-supervisor Associate Professor Paul Barendse, your insight and suggestions were always extremely helpful and well received.

A special acknowledgement and thanks go to Chris Wozniak for your technical expertise, patience and willingness to help. The advice you offered was not just relevant for my project for my career in this field as well. Much appreciated.

Many thanks go to Shireen Sabodien, for taking care of all the administrative requirements. Very much appreciated.

I would also like to thank Jacques for your help throughout my project. Thanks also go to Chris De Beer and the rest of my AMES Research Group family for your encouragement, support and technical help throughout my master's degree. Thanks to Akrama, Hossein, Anesu, Daleel, Oladapo, Ramzi and everyone else in the group. Your friendship made for a good working environment and made my studies enjoyable in the Research group.

EXECUTIVE SUMMARY

Doubly Fed Induction Generators (DFIGs) are common for use in wind power generation. This can be attributed to factors such as the variable speed operation of the rotor, which can be adjusted through control systems with varying wind speed, ensuring more efficient power conversion.

The stator windings in a DFIG are directly connected to the grid while the rotor windings are connected to the grid via back to back converters. This allows for independent active and reactive power control through the rotor side convertor and lower rating of converter which leads to lower cost of the system. The system below is a schematic of experimental set-up of the doubly fed induction generator connected to the grid.

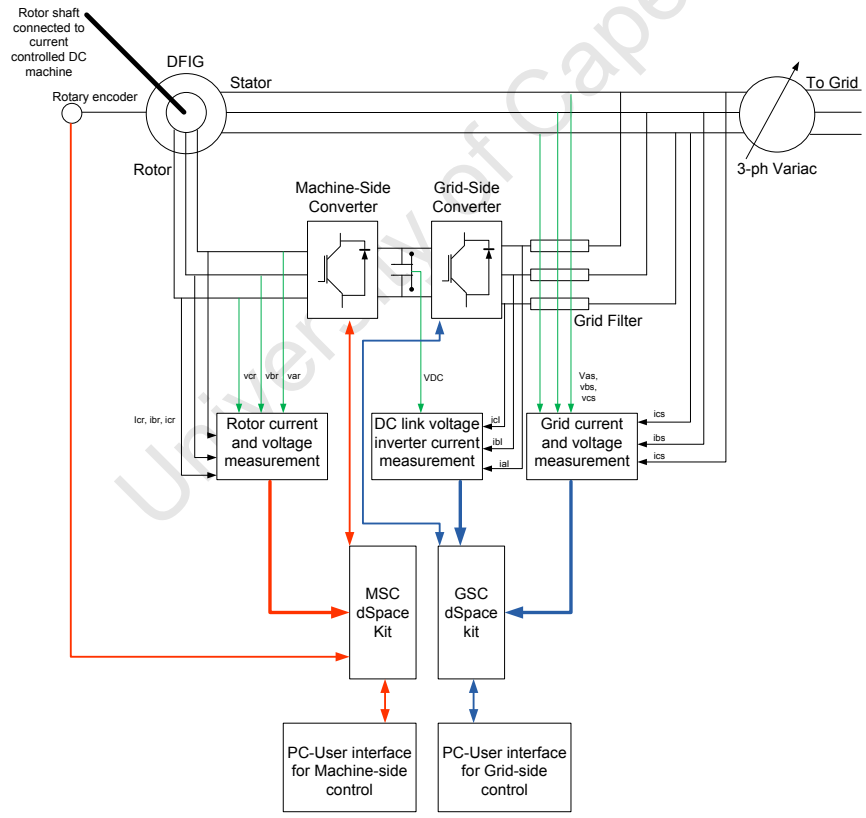

Figure A: Schematic of experimental set-up of doubly fed induction generator connected to the grid

In this dissertation, the dynamic model and control of a doubly fed induction generator is presented. Figure A above shows the schematic of the experimental setup of the doubly fed induction generator connected to the grid as well as to measuring devices, dSpace kits and PC User Interfaces. The vector controlled DFIG was modelled from fundamental equations which are laid out in Chapter 2. The grid-side control was also developed from first principles. It was shown how this system can be used as a test bench for further improvements in wind energy technology in South Africa where wind energy use is on the increase, as well as the rest of the world. Matlab Simulink was used for the software implementation of the system and Control desk was used for the hardware implementation of the system.

The experimental set up was assembled by the author and this fulfilled the objective to add a doubly fed induction generator test system to the AMES Research Group. An LCL filter was designed for the system and the inductors were then procured according to the design parameters. The capacitors used were obtained from the Machines laboratory.

The system was simulated in software and implemented on hardware both with balanced and unbalanced grid and the results obtained were compared so as to see how the system behaves and to validate its operation. A 30% over voltage and 50% voltage dip were implemented in software while a type B voltage dip was implemented in hardware. It was shown that by implementing dual vector current control the system remains stable and the currents are balanced despite unbalance being present.

To validate the operation of the control, the machine–side converter and grid–side converter were first tested in isolation after the whole system was tested. It was found that the system was operational and remained stable during the test conditions. The reactive power capability of the system was also verified by simulated and experimental results which show the system being able to produce positive and negative quadrature axis current.

TABLE OF CONTENTS

LIST OF FIGURES

Chapter 3

Chapter 4

Chapter 5

LIST OF TABLES

LIST OF ABBREVIATIONS

ADC	Analogue to Digital Conversion
d-axis	Direct axis
DFIG	Doubly Fed Induction Generator
DVCC	Dual Vector Current Control
HCC	Hysteresis Current Control
LEM	Line Entrance Module
PLL	Phase Lock Loop
PWM	Pulse Width Modulation
q-axis	quadrature axis
SVM	Space vector Modulation
TSR	Tip Speed Ratio
WECS	Wind Energy Conversion System

1. Introduction

1.1. Project Overview

This project adds to the scope of the work the AMES Research Group is working into and serves as a test bench for grid integration studies as well as future studies on the control of doubly fed induction generators for wind energy applications.

A system for grid integration studies of a Doubly Fed Induction Generator (DFIG) is developed, and as this is for wind energy applications, a DC machine and drive was used to emulate the wind turbine blades. The DFIG was modelled from fundamental equations and from these equations the control of the machine was developed in the synchronous reference frame. Matlab Simulink was then used for the modelling of the system in software and control desk in hardware. Once the system was set up in software, various tests such as speed control tests and tests with balanced and unbalanced grid conditions were implemented so as to demonstrate and confirm the operation of the model. The same tests were also implemented in hardware so to validate the model and it was then observed how the experimental results compared with the simulated results.

1.2. Background to Research

With current trends in South Africa moving towards renewable energy; wind energy in particular, the AMES research is looking to answer very prevalent questions and to come up with solutions to these questions which include; better efficiency, greater power extraction from the wind, better integration of wind power systems to the grid as well as providing ancillary services such as reactive power compensation to the grid during unbalanced grid conditions.

Work on wind turbine control under different wind speed conditions using a Permanent Magnet Synchronous Generator has been carried out previously by two

post graduate students from the AMES Research Group in fulfilment of their Master of Science degree requirements for Electrical Engineering. This project therefore looks to add to the work the research group is doing by developing a control system for a doubly fed induction generator that will be used to improve grid integration of DFIGs into the utility grid as well as provide ancillary services to the grid. Literature is now reviewed in the following section so as to see the current work being done in this area and to ensure that this project is both relevant and up to date.

1.3. Literature Review

Wind energy has been on the increase and looking at some figures according to the European Wind Energy Association (EWEA), there has been significant increase in the total installed capacity in the EU with the high figure of up to 105.6GW total installed capacity in 2012 this represent 26 % of all installed power capacity in that year [1]. Figure 1.1 below shows annual increases in wind power installations in the EU from the year 2000 to 2012 according to the 2012 report "Wind in Power: 2012 European Statistics", released in February 2013. Further details can be found at [2]

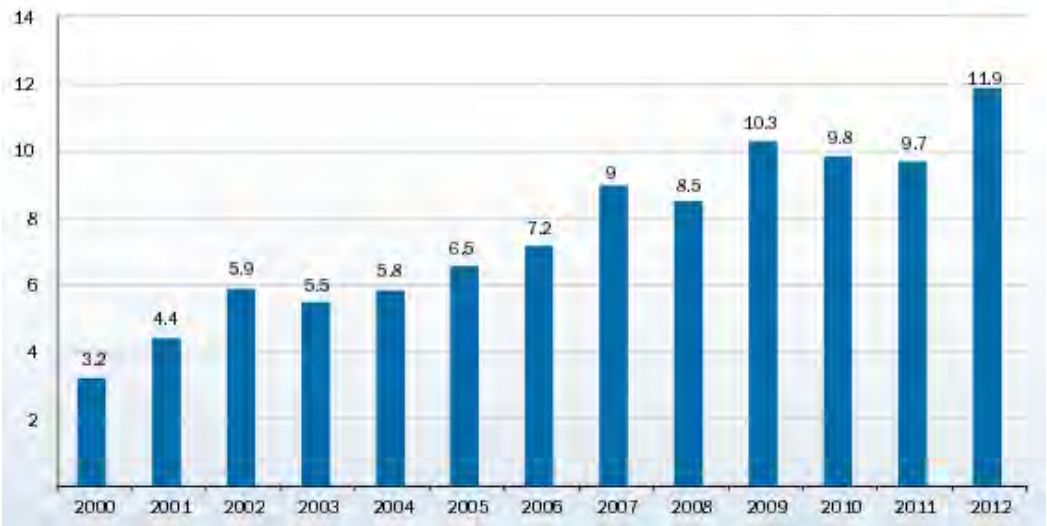

Figure 1.1: Wind power installations in the EU from 2010 to 2012 [2]

Figure 1.2 below shows job creation due to increasing wind power installation which is also another benefit.

Figure 1.2: Job increases in the EU due to Wind Power [1]

In South Africa, there is an urgency to add renewable energy sources so as to meet the increasing energy demand and reduce the carbon emissions. Table 1.1 below shows revised balanced scenario capacity according to the IRP in the "INTEGRATED RESOURCE PLAN FOR ELECTRICITY, 2010 -2030, Revision 2. Final Report" released on 25 March 2011 [3].

Table 1.1: Revised balanced scenario capacity for 2010 – 2030 [3]

	Total generating capacity in 2030		Capacity added (including committed) from 2010 to 2030		New (uncommitted) capacity options from 2010 to 2030	
	MW	%	MW	%	MW	%
Coal	41074	48.2	16386	31.4	6253	16.3
OCGT	9170	10.8	6770	13.0	5750	15.0
CCGT	1896	2.2	1896	3.6	1896	5.0
Pumped Storage	2912	3.4	1332	2.5	0	0.0
Nuclear	11400	13.4	9600	18.4	9600	25.1
Hydro	5499	6.5	3399	6.5	3349	8.8
Wind[1]	11800	13.8	11800	22.6	11000	28.8
CSP	600	0.7	600	1.1	400	1.0
PV	0	0.0	0	0.0	0	0.0
Other	890	1.0	465	0.8	0	0.0
Total	85241		52248		38248	

Notes: (1) Wind includes the "Renewables" bucket identified in the RBS after 2019

Factors that are driving this growth both in Europe and the rest of the world include; attractive economics, i.e., there has been a drop in the costs of the process involved in wind energy extraction [4]. This drop in cost can be attributed to the development in the manufacture of wind turbines, such as; improvement in blade design which results in greater energy capture, reduction in raw materials used which leads to lighter

weight wind turbines, and turbine capacity has been increased [4]. Further, there has been a tremendous advancement in the power electronics and control systems of wind turbines which makes integration to the grid easier [4].

The fact that wind energy conversion is a sustainable technology also makes it attractive as it is a solution that leads to the resolve of some critical issues associated with traditional fossil fuels, such as global warming, market volatility and political uncertainty in countries which they are located [5].

In addition, more governments are supporting the move towards wind energy in their countries and more customers and power utilities are more aware of the environmental aspects of electric power [4].

One disadvantage of wind energy however, is that the primary source, the wind, is uncontrollable. The challenge therefore is to get good quality electrical energy from this irregular source, as well as other instability due to faults on the grid to which the wind energy conversion system is connected.

This thesis addresses the second issue, the power quality problems that arise due to faults or voltage unbalance on the grid, and demonstrates how a system on which these and any other such problems arising in industry can be tested and solved before being implemented on a large scale.

The type of generator that has been chosen for the project is the Doubly Fed Induction Generator (DFIG). Some of the reasons for this include the fact that the convertor size is reduced to about 25% of the full power rating, which corresponds to the slip of the rotor [6]. Other contributing factors are; decoupled active and reactive power control that improves integration into the grid, reduced acoustic noise and mechanical stress as well as the increase in the efficiency of energy capture by the machine achieved via pitch control of the blades [7].

1.4. Objectives of this Thesis

The objectives of this thesis are to;

- Conduct a literature review on wind energy technology and some wind energy conversion topologies.
- Model a vector controlled doubly fed induction machine from fundamental principles in the synchronous reference frame.
- Model a vector controlled grid-side system from fundamental principles including grid filter design.
- Implement the DFIG system in Matlab Simulink.
- Conduct tests to observe the response of the control to rotor speed, DC link voltage changes as well as to balanced and unbalanced grid conditions.
- Implement the DFIG system experimentally on hardware to validate its operation.
- Compare results from the simulated model with those from the experimental model and draw conclusions on the DFIG controllability.

1.5. Scope of Work

The wound rotor induction machine and DC machine available for this project have a rating of 2.2 kW.

All equipment used was based on what was available in the lab except for the inductors used in the LCL filter as they were designed and procured to suit the requirements of the project. A DC Bus voltage of 600 V was used in Matlab Simulink model but due to physical constraint of the variac in hardware, the bus could achieve a maximum value of 300 V.

1.6. Outline of Thesis

The rest of this dissertation is laid out as follows;

Chapter 2: This chapter lays out the fundamentals of wind power making mention of the equations that govern wind power extraction. The different Wind Energy Conversion (WECs) Topologies are then presented for the Squirrel Cage Induction Machine (SCIM), the Permanent Magnet Synchronous Machine and finally the DFIG.

Details of the modelling of the vector controlled DFIG is then laid out in detail firstly explaining the modelling of the machine in steady state so as to set the foundation, and then going on to model it dynamically in the $\alpha\beta$ reference frame and then in the synchronous (DQ) reference frame.

The vector controlled grid model is also presented from fundamentals. The pattern followed is the same as that of the modelling of the DFIG; first by modelling the grid in steady state and then going on to model it dynamically. Along with the grid model, the Filter design is also given mathematically and in the s-plane.

Chapter 3: This chapter gives the details of how the system was set up in software using Matlab Simulink as well as experimentally in the Machines laboratory. Sections 3.2 and 3.3 give the Simulink models of the Grid – side converter control and Rotor – side converter control. The Phase Locked Loop (PLL) and Proportional Integral (PI) controllers are given in a bit more detail. The calculation of the inductances for the LCL filter is also presented here.

Section 3.4 then lays out the hardware set-up and presents some of the components used as well as the calculations used for the selection of these components.

Chapter 4: Here all the results obtained from the simulations are presented. The rotor – side converter control and DFIG are first simulated in isolation and it is shown that the speed and torque control is operating as expected.

The grid – side converter control results are then given showing specifically the DC link voltage control as well as the independent control of the direct and quadrature axis current components. The complete system is the simulated and results recorded

showing the response of the control to speed changes well as balanced grid and to unbalanced grid.

Chapter 5: In this chapter, the tests that were performed in Chapter 4 for the simulated system are now performed here for the experimental validation. Below are some of the operating modes for the experimental validation.

Transient operation of the DFIG

In this mode of operation, the rotor speed is stepped up from sub-synchronous to super synchronous speed, and the stepped down from super-synchronous speed to sub-synchronous speed. The operating rotor three phase currents are recorded during this transient operation. The signals recorded validate the sub-system operation of the machine–side converter control.

Reactive power capability

The ability of the whole system operation and reactive power capability are verified by steeping the reactive current, q current component, to -3 A. The real and reactive powers are calculated respectively. The independent control of the d and q current components are also demonstrated in that, there is no change in the d current component when the q current component is set to -3 A.

Dual Vector Current Control during a Type B Voltage unbalance

Dual vector current control is implemented and the positive and negative sequences of the direct and quadrature axis current components are recorded. During grid voltage imbalances, DVCC is able to control the separate d and q negative and positive components, and hence is able to maintain the quadrature axis current component as well as the negative sequence current components at zero which would otherwise cause imbalances in the current signals and render the control unstable if it were at any other value.

Chapter 6: The simulated and experimental results are compared and discussed in this chapter.

Chapter 7: Conclusions, based on the discussion in Chapter 6, are drawn and presented in this chapter.

Chapter 8: Recommendations for future work are made.

2. MODELLING AND CONTROL OF DOUBLY FED INDUCTION GENERATOR

2.1. Introduction

This chapter will detail the modelling of the machine. The machine model is simplified by using equivalent circuits and reference frames so as to reduce the machine into a state from which it is easy to get the necessary parameters for controlling it.

The machine will be modelled dynamically from fundamentals in the direct, quadrature and zero axes, commonly referred to as the dq model. This process could be lengthy and difficult but will be simplified.

Firstly, an overview of the fundamentals of wind power is discussed below.

2.2. Fundamentals of Wind Power

Over the past centuries, wind turbines have evolved tremendously. Initially wind turbines, that were commonly called windmills, took advantage of the power found in the wind and were used for grinding grain and pumping water, but these have almost completely died away. The technology of using the wind to drive blades for the production of electrical power has taken their place and is greatly advancing.

This increase can be attributed to support from governments and power utilities in the move towards renewable energy, as well as increasing awareness of the environmental aspects of power production [4]. Further, a lot of research into improvement of wind energy technology is currently on going and this has led to more efficient and cost effective power production from wind energy, making it more attractive.

Wind turbines can either be vertical axis or horizontal axis turbines. Three blade horizontal wind turbines are the most common [8]. As wind turbine technology has been improved, the turbines themselves have been made larger and hence able to capture more wind power. This concept is proven in the following equations.

Kinetic energy found in the wind is given by [9];

$$\frac{1}{2}\, x\, (air\ mass)\, x\, (air\ velocity)^2 \tag{2.1}$$

The theoretical power available for extraction by the blades is thereby;

$$P_\omega = \frac{1}{2}\, x\, \rho A v\, x\, v^2 \tag{2.2}$$

Where; A is the cross section area through which this power is extracted. v is the air velocity and ρ is the air density.

The larger the blades, the greater the area and hence the greater the theoretical power that can be extracted [9].

But in practice, only a fraction of this power can be extracted and the governing equation is developed below based on Figure 2.1.

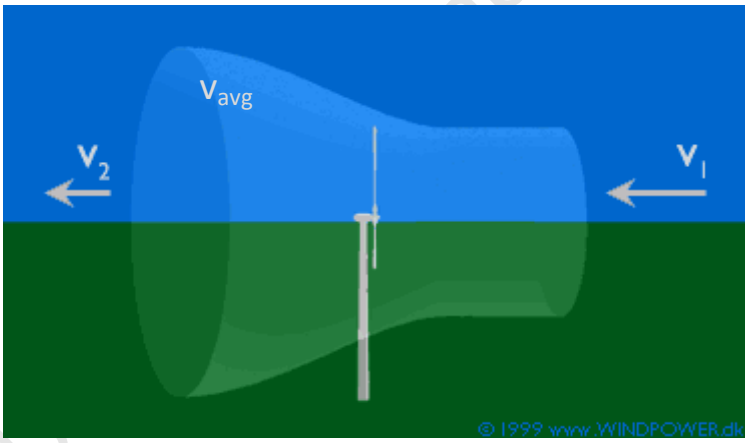

Figure 2.1: Wind deflection by turbine; wind velocities before and after wind turbine [10]

From Figure 2.1 above, the power that is extracted by the turbine is given by [11];

v_1 is the velocity of the wind before the wind turbine and v_2 is the velocity of the wind after it goes through the wind turbine. v_{avg} is the average of the two velocities v_1 and v_2

$$P = \frac{1}{2} m(v_1{}^2 - v_2{}^2) \tag{2.3}$$

Where $m = \rho A \mathrm{v}_{\mathrm{avg}}$ and $\mathrm{v}_{\mathrm{avg}} \approx \frac{1}{2}(\mathrm{v}_1 + \mathrm{v}_2)$

Using the above definitions for m and $\mathrm{v}_{\mathrm{avg}}$, equation (2.3) is expanded and becomes equation 2.4 below.

$$P = 0.5\,\rho A\ {}^{3}[\tfrac{1}{2}(1 + \quad)\big(1 - \quad{}^{2}\big)] \tag{2.4}$$

From [11] we know that;

$$C\ (\ ) = \tfrac{1}{2}(1 + \quad)\big(1 - \quad{}^{2}\big) \tag{2.5}$$

By substituting equation (2.5) into (2.4) and using Bet'z law, the maximum power that can be extracted from the wind is related to the wind speed by the following equation [11]

$$\mathrm{P} = 0.5 \quad \mathrm{R}^2\ {}^{3}\mathrm{C} \tag{2.6}$$

Where is the air density.

R is the radius of the turbine

v is the wind speed

C_p is the power coefficient

is the tip speed ratio (TSR).

The highest value that C_p can attain theoretically is 0.5926; hence the maximum power that can be extracted is approximately 60 % of the cubed wind speed [5]. The figure below shows the relationship of the power coefficient, Cp, and the tip speed ratio, λ [5].

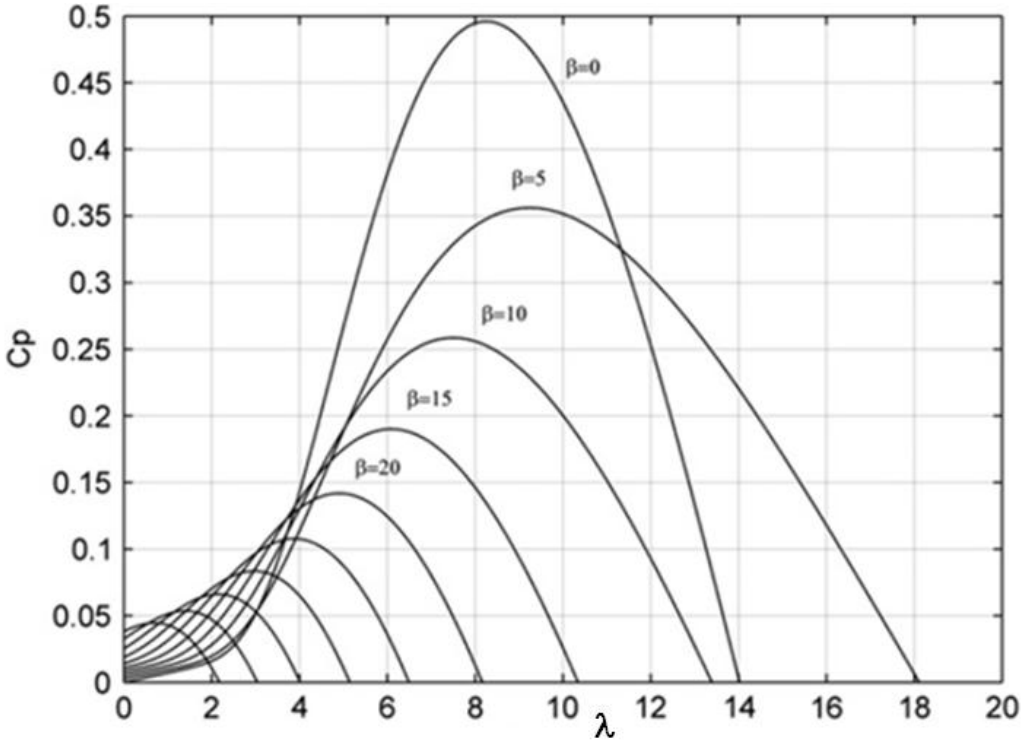

Figure 2.2: Power coefficient Cp versus λ [12]

From [13], the torque is given by;

$$T_w = \frac{r^2 v^3 C_p}{2 \ _w} \tag{2.7}$$

Where $_w$ *is the angular speed of the wind.*

The turbine model of the DFIG system comprises of the blades, the low speed shaft, the gearbox, and the high speed shaft. Power is extracted from the wind when the blades of the turbine turn due to the force exerted on them by the wind [7].

2.3. WECS Topologies

Wind Energy Conversion Systems (WECS) have several different topologies depending on the type of machine used as well as the application. WECS can also be classified according to their speed of operation, that is, fixed-speed or variable-speed operation of the systems.

The simple design and low maintenance of fixed-speed WECS made them popular in the past. This type of system consists of an induction machine connected directly to the grid. The term fixed speed is due to the fact that there is no speed control in this system and the operating speed is constant and not dependent on the changing wind speed. This means they can only achieve optimal aerodynamic efficiency at a single wind speed [14].

Variable speed WECS are more preferred owing to the ability for independent speed control. This is due to the technological advances in power converters. Furthermore, the ability to change the speed of operation of the generator allows the system to operate at higher aerodynamic efficiencies over a wider range of wind speeds [14].

In this section, some common topologies are discussed and then the one that is used for this dissertation is outlined.

2.3.1. Squirrel Cage Induction Machine

Squirrel Cage Induction machines are used for variable speed operation. The back to back converter is connected to the stator windings and has to be rated for the full machine power [15]. Figure 2.3 below shows the layout of the Squirrel Cage Induction Generator (SCIG) WECS topology with full bridge back to back converters.

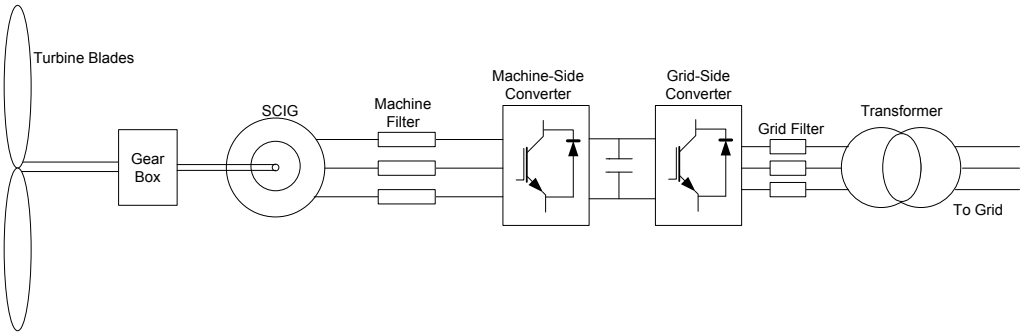

Figure 2.3: Layout out of SCIG WECS topology with full bridge back to back conveters

According to [16] squirrel cage induction machines are not to be overlooked among the WECS technologies. They are low cost and have a low maintenance requirement which further reduces the cost. They are also robust and have the full speed range operation and complete control of active and reactive power [17]. However the full power rating of the converter can be costly.

2.3.2. Permanent Magnet Synchronous Machine

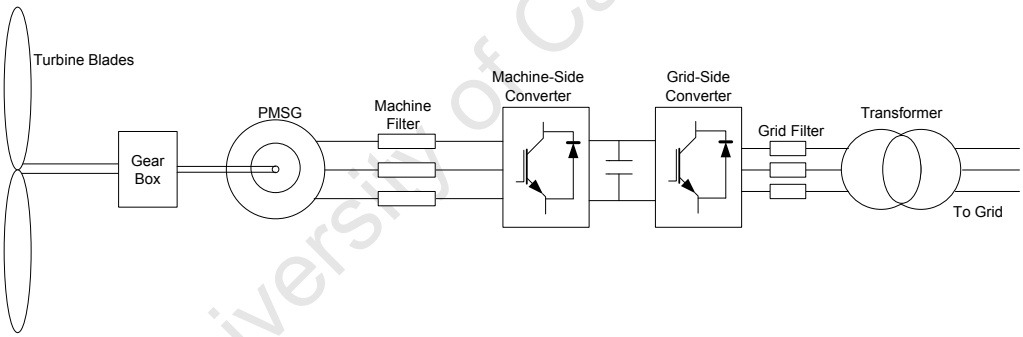

Figure 2.4: Layout of PMSG WECS topology with full bridge back to back converters

Figure 2.4 above shows the layout of Permanent Magnet Synchronous Generator (PMSG) WECS topology with back to back converter [15]. This topology is used for variable speed operation made possible by the power converter. PMSGs do not require reactive power hence they can be connected with various converter topologies. Only two are shown here in Figure 2.4 and Figure 2.5.

PMSGs have the advantage of the full operating speed as well as independent control of active and reactive power exchanged with the grid. They do not require much maintenance because they have no brushes on the generator. However PMSGs consist

of permanent magnets which are rare earth metals, hence they become very expensive to make as the MW capacity increases [13].

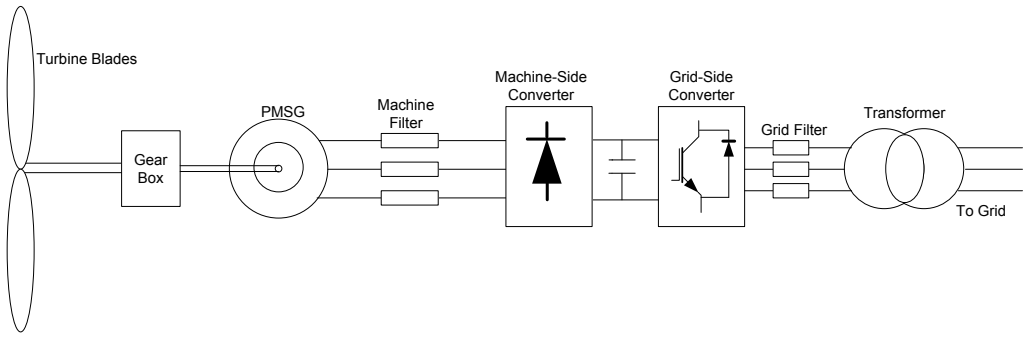

Figure 2.5: Layout of PMSG WECS topology with a Diode Rectifier-VSI converter

In Figure 2.5 showing the layout of the PMSG WEC topology, one converter has been replaced with a diode rectifier which greatly simplifies the control and reduces the cost of the system [15]. This topology is possible because the PMSG does not require reactive power and a bidirectional converter can be done away with.

2.3.3. Doubly Fed Induction Machine

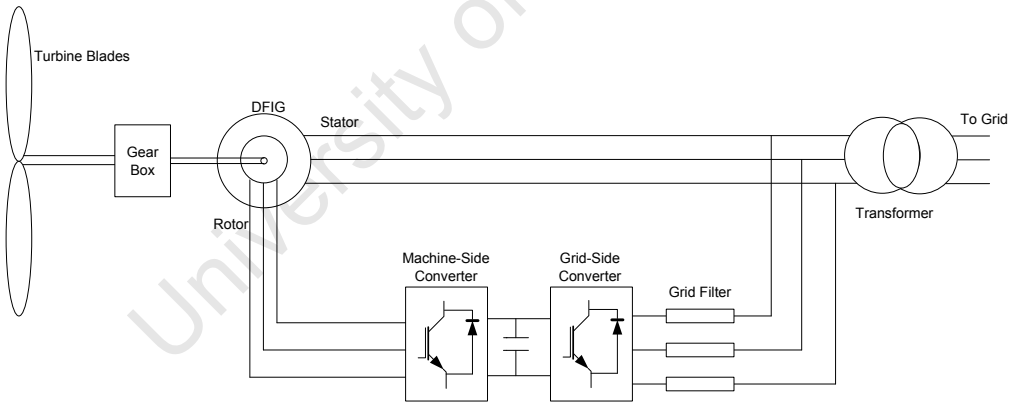

Figure 2.6: Layout of DFIG WECS Topology with Full bridge back to back converters

A DFIG WECS topology is the basis of this project. In this topology the back to back converter is connected to the rotor windings resulting in a much lower rating for the converter, about 30 % of the stator power, which reduces the cost of the converter [15]. The stator is connected directly to the grid. There is independent control of the

active and reactive power as well as a wide range of operating speed which is controlled by the machine side converter.

2.4. Machine Side Modelling and Control

This section will discuss the detailed model of the doubly fed induction machine from fundamental equations. The equations that represent the machine will be derived by using the principle of phasors and the different reference frames that the phasors can be represented in. Most of the equations and modelling methods in the preceding sections have been adapted from [13], which gives a clear and concise way of modelling the system.

2.4.1. Steady State Model of the Doubly Fed Induction Machine

In order to set a good basis for understanding of the machine behaviour, a brief look at the steady state model is presented below. The dynamic behaviour of the machine will then be developed with this understanding.

The following assumptions are made about the machine so as to allow for it to be modelled in steady state [13];

1. The stator is supplied by balanced and constant three-phase ac signals from the grid, i.e. frequency and voltage amplitude.
2. The rotor is also supplied by balanced and constant three-phase ac signals through the back to back power converters independently from the stator.

The above assumptions are incorporated into the development of the electric models and derivations of the electric equations.

The doubly fed induction machine is made of a stator and a rotor each carrying three-phase windings which are spatially shifted by 120°. The rotor is mounted on bearings and separated from the stator by a gap known as the airgap. The two sets of windings are independently supplied and below are the equations of the balanced three-phase currents flowing through the windings [13].

$$i_a = I_m Cos(\omega t) \tag{2.8}$$

$$i_b = I_m Cos(\omega t - 120°) \tag{2.9}$$

$$i_c = I_m Cos(\omega t + 120°) \tag{2.10}$$

In the stator, when the windings are supplied by a balanced three-phase voltage at the grid frequency f_s, a stator flux is induced in the air gap and rotates at synchronous speed which is given by [15] and *p* is the number of pole pairs;

$$n_s = \frac{60 f_s}{p} (\frac{revs}{\min}) \tag{2.11}$$

This flux then induces an emf in the rotor windings. The angular frequency of the induced rotor voltages and currents is given by [13] ;

$$\omega_r = \omega_s - \omega_m \tag{2.12}$$

$_r$ is the angular frequency of the voltage that is supplied to the rotor windings externally $_m$ is the machine's electrical angular frequency and is related to the mechanical angular speed Ω_m as has also been represented in [15] as;

$$\omega_m = p\Omega_m \tag{2.13}$$

The relationship between the stator and rotor angular frequency can now be looked at below;

$$s = \frac{\omega_s - \omega_m}{\omega_s} \tag{2.14}$$

s is the slip of the rotor;

$$\omega_r = s\omega_s \tag{2.15}$$

Frequency can also be expressed as;

$$f_r = sf_s \tag{2.16}$$

The machine can be operated in the following three modes and the sign of the slip is determined by the mode in which the machine is operating [15].

Sub-Synchronous Operation $\Rightarrow \omega_m < \omega_s \Rightarrow \omega_r > 0 \Rightarrow s > 0$

Synchronous Operation $\Rightarrow \omega_m = \omega_s \Rightarrow \omega_r = 0 \Rightarrow s = 0$

Super-Synchronous Operation $\Rightarrow \omega_m > \omega_s \Rightarrow \omega_r < 0 \Rightarrow s < 0$

2.4.2. Dynamic Modelling of the Doubly Fed Induction Machine

The steady state model of the induction machine is very useful in testing the performance of the machine in steady sate. But with the DFIG, the steady state is not sufficient because electrical transients cannot be neglected during variable speed operation of the DFIG. Hence the machine will be modelled dynamically in this section.

Below is a representation of an ideal three-phase Doubly Fed Induction Machine (DFIM). The stator windings (outer windings) and the rotor windings (inner windings) are shown together with the current vectors and the voltage across the windings [13].

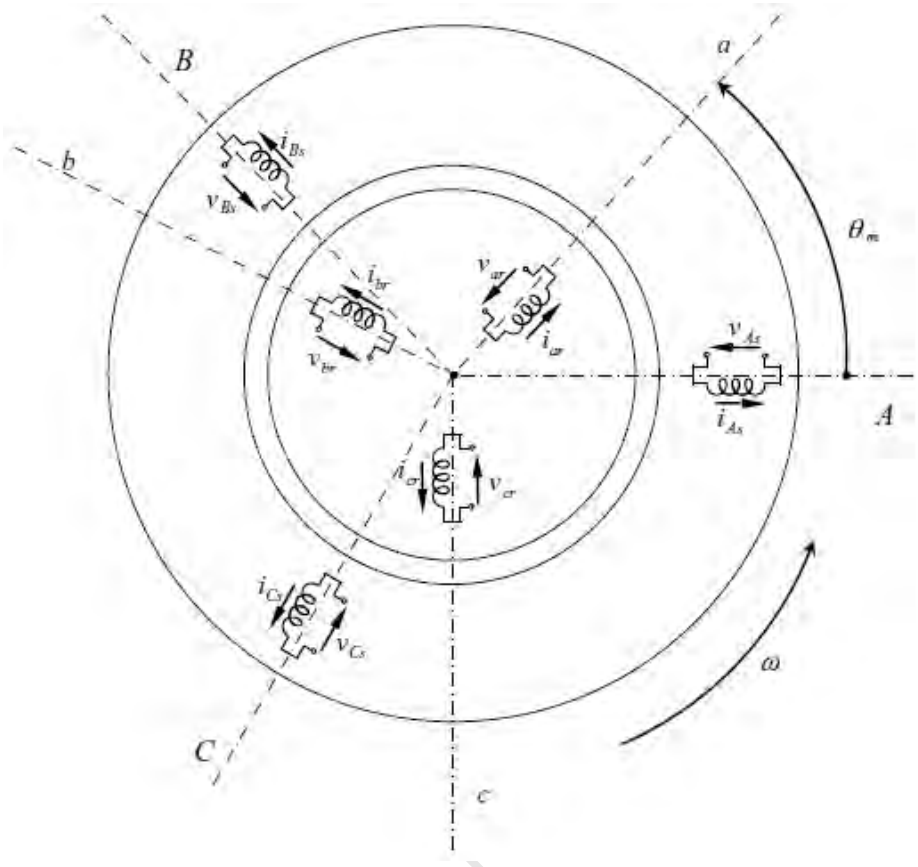

Figure 2.7: Ideal three-phase stator and rotor windings of the DFIG [13**]**

From the ideal model above, the following equations showing the relationship of the instantaneous stator voltages to the currents and fluxes of the machine are obtained [15].

$$v_{As}(t) = R_s i_{As}(t) + \frac{d\ _{as}(t)}{dt} \tag{2.17}$$

$$v_{Bs}(t) = R_s i_{Bs}(t) + \frac{d\ _{bs}(t)}{dt} \tag{2.18}$$

$$v_{Cs}(t) = R_s i_{Cs}(t) + \frac{d\ _{cs}(t)}{dt} \tag{2.19}$$

In the same way, the rotor electric relationships can be described by the equations below [13].

$$V_{ar}(t) = R_r i_{ar}(t) + \frac{d\ _{ar}(t)}{dt} \tag{2.20}$$

$$V_{br}(t) = R_r i_{br}(t) + \frac{d\ _{br}(t)}{dt} \tag{2.21}$$

$$V_{cr}(t) = R_r i_{cr}(t) + \frac{d\ _{cr}(t)}{dt} \tag{2.22}$$

From the above equations, a complete representation of the DFIG can be deduced. The representation is shown below [13];

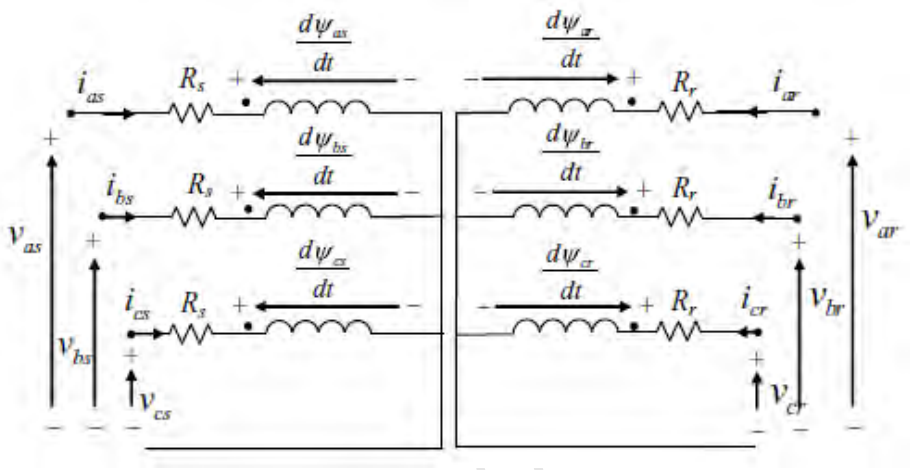

Figure 2.8: Equivalent circuit of the DFIG [13]

Where $_{as}$, $_{bs}$, $_{cs}$ and $_{ar}$, $_{br}$, $_{cr}$ are the stator and rotor fluxes respectively. The following are the rotor parameters to be referred to the stator [13];

Rotor currents; $i_{ar}(t)$, $i_{br}(t)$, $i_{cr}(t)$

Rotor resistance; R_r

Rotor voltages; $v_{ar}(t)$, $v_{br}(t)$, $v_{cr}(t)$

In the dynamic model, unlike the steady state, angular frequency $_r$ is no longer considered to be constant. The relationship between the rotor and stator angular frequency is shown below to be;

$$_r + \ _m = \ _s \tag{2.12}$$

$_m$ is the machine's electrical angular frequency and is related to the mechanical angular speed Ω_m as shown below [13];

$$_m = p\Omega_m \quad (2.23)$$

Where p is the number of pole pairs.

2.5. Three to Two phase Model of Doubly Fed Induction Generator

The concept of dq modelling in induction machines is a concept that is based on the operation of the dc machine. Below is the schematic diagram of a dc machine.

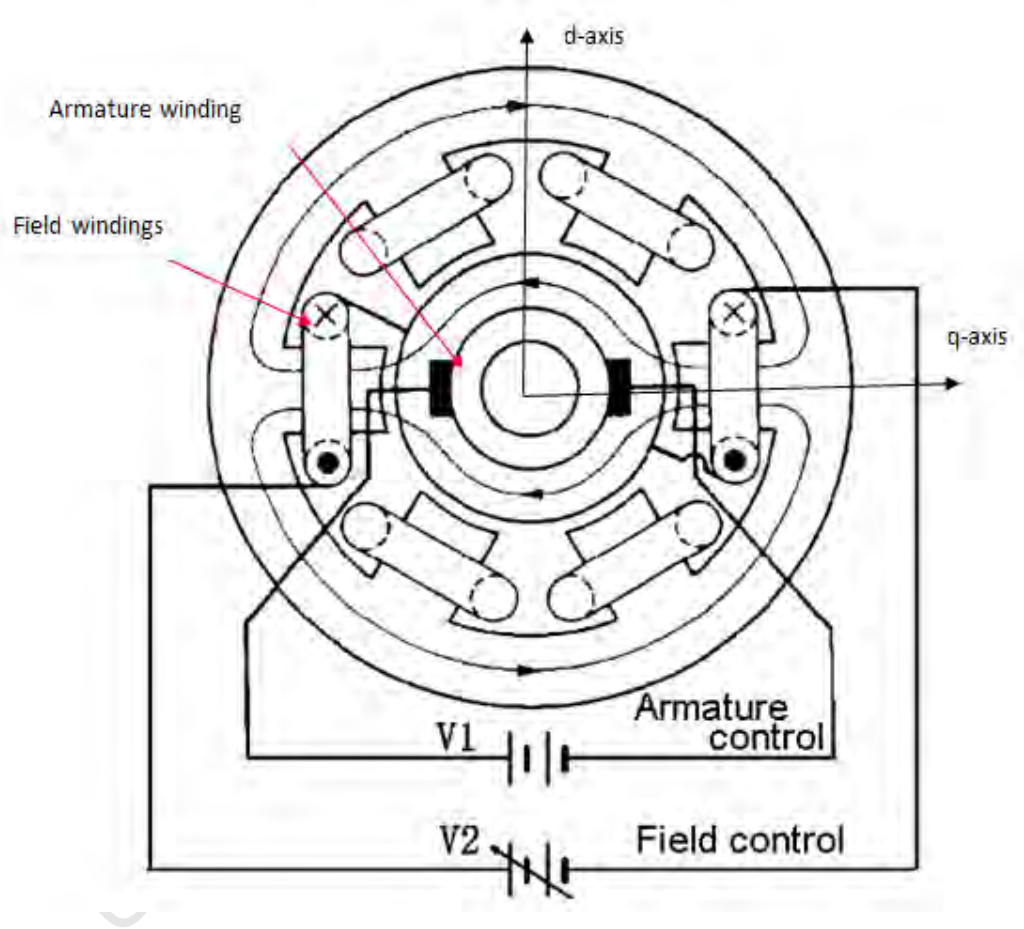

Figure 2.9: Schematic diagram of a DC Machine, d and q axis and control [18]

The dc machine consists of the armature winding, which is placed on the rotor and field windings (shunt and series windings) which are placed on the stator as can be seen in Figure 2.9 above. The mmf due to the armature current is symmetrical about the two adjacent poles called the quadrature axis (q-axis). The field windings produce a flux distribution in the air gap and this flux is symmetrical about the pole axis which is also known as the direct axis (d-axis).

This means that in a dc machine, one has independent access to the torque via the armature windings and magnetic field via the field windings. Further, the physical construction of this machine ensures the perfect conditions for optimal torque production. This is due to the fact that the air gap flux distribution which is symmetrical about the q-axis, is at 90 degrees to the armature current which is symmetrical to the d-axis. Hence the flux vector is perpendicular to the field vector.

In induction machines however, one only has access to the stator windings which are responsible for producing both the magnetic field and armature current. By modelling the machine in the dq reference frame, the torque and armature current can be decoupled and hence controlled independently.

Equivalent circuits, equations and reference frames of DFIM are detailed; finally leading to the DQ model of the machine.

The machine will first be modelled in the stationary reference frame ($\alpha\beta$ model) and then in the synchronous reference frame (dq model).

2.5.1. Stationary $\alpha\beta$ model

In order to simplify the model so far, the three windings can be replaced with two windings. This is called the $\alpha\beta$ model. The $\alpha\beta$ frame is aligned with the stator, since this reference frame is stationary, its rotation speed is zero and the signals produced are time varying signals.

Space vector notation is used to derive the voltage equations of the DFIM. Equations 2.17 and 2.20 are multiplied by $\frac{2}{3}$ [13];

$$\frac{2}{3}V_{as}(t) = \frac{2}{3}R_s i_{as}(t) + \frac{2}{3}\frac{d\ _{as}(t)}{dt} \tag{2.24}$$

$$\frac{2}{3}V_{ar}(t) = \frac{2}{3}R_r i_{ar}(t) + \frac{2}{3}\frac{d\ _{ar}(t)}{dt} \tag{2.25}$$

Equations 2.18 and 2.21 are multiplied by $\frac{2}{3}a$ [13];

$$\frac{2}{3}aV_{bs}(t) = \frac{2}{3}a\,R_s i_{bs}(t) + \frac{2}{3}a\,\frac{d\ _{bs}(t)}{dt} \tag{2.26}$$

$$\frac{2}{3}aV_{br}(t) = \frac{2}{3}aR_r i_{br}(t) + \frac{2}{3}a\,\frac{d\ _{br}(t)}{dt} \tag{2.27}$$

Finally, equations 2.19 and 2.22 are multiplied by $\frac{2}{3}a^2$

$$\frac{2}{3}a^2V_{cs}(t) = \frac{2}{3}a^2R_s i_{cs}(t) + \frac{2}{3}a^2\,\frac{d\ _{cs}(t)}{dt} \tag{2.28}$$

$$\frac{2}{3}a^2V_{cr}(t) = \frac{2}{3}a^2R_r i_{cr}(t) + \frac{2}{3}a^2\,\frac{d\ _{cr}(t)}{dt} \tag{2.29}$$

The resulting stator and rotor equations are then added (stator and rotor equations added separately) to yield the following equations below [13];

$$\tilde{\mathrm{v}}_s^s = R_s\tilde{\mathrm{i}}_s^s + \frac{d\ _s^s}{dt} \tag{2.30}$$

$$\tilde{\mathrm{v}}_r^r = R_r\tilde{\mathrm{i}}_r^r + \frac{d\ _r^r}{dt} \tag{2.31}$$

Where $\tilde{\mathrm{v}}_s^s$ is the space vector of the stator voltage and $\tilde{\mathrm{i}}_s^s$ is the space vector of the stator current and $_s^s$ is the space vector of the stator flux. These are the stator coordinates in the $\alpha\beta$ reference frame [13].

Similarly on the rotor side v_r^r is the space vector of the rotor voltage and $\tilde{\mathrm{i}}_r^r$ is the space vector of the rotor current and finally $_r^r$ is the space vector of the rotor flux. These rotor coordinates are represented in the dq reference frame [13].

s and *r* are reference frames to which the space vectors are referred, that is, the stator and rotor reference frames respectively.

The equations below indicate the relationship between the fluxes and currents [13].

$$_s^s = L_s\tilde{\mathrm{i}}_s^s + L_m\tilde{\mathrm{i}}_r^s \tag{2.32}$$

$$_r^r = L_m\tilde{\mathrm{i}}_s^r + L_r\tilde{\mathrm{i}}_r^r \tag{2.33}$$

And the stator and rotor leakage inductances are related as follows;

$$L_s = L_{\sigma s} + L_m \tag{2.34}$$

$$L_r = L_{\sigma r} + L_m \tag{2.35}$$

It is important to note that in the above equations (2.34) is in the stator reference frame, while (2.35) is in the rotor reference frame.

In order to obtain the αβ model of the DFIM the space vectors are referred to the stator reference frame and equation (2.31) is multiplied by $e^{j\theta_m}$. The following equations are obtained [13];

$$\tilde{v}_s^s = R_s \tilde{i}_s^s + \frac{d\ {}^s_s}{dt} \tag{2.36}$$

$$\tilde{v}_r^s = R_r \tilde{i}_r^s + \frac{d\ {}^s_r}{dt} - j\ {}_m\ {}^s_r \tag{2.37}$$

$${}^s_s = L_s \tilde{i}_s^s + L_m \tilde{i}_r^s \tag{2.38}$$

$${}^s_r = L_m \tilde{i}_s^s + L_r \tilde{i}_r^s \tag{2.39}$$

From the αβ model in the stator reference, the following electrical model is obtained.

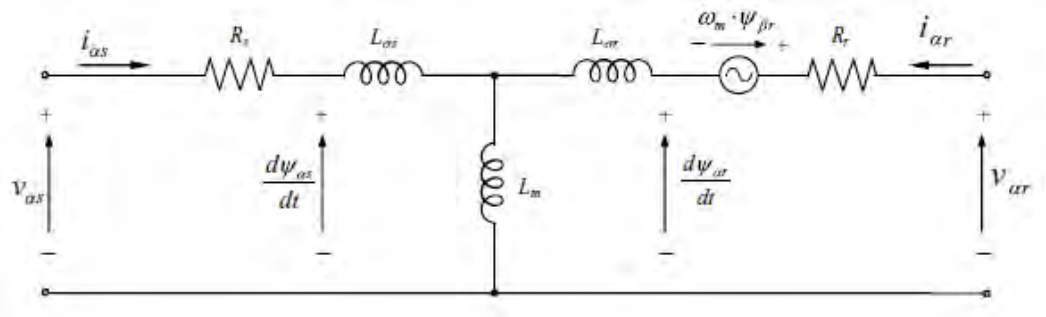

Figure2.10: Equivalent electrical model in the (alpha) α reference frame [13]

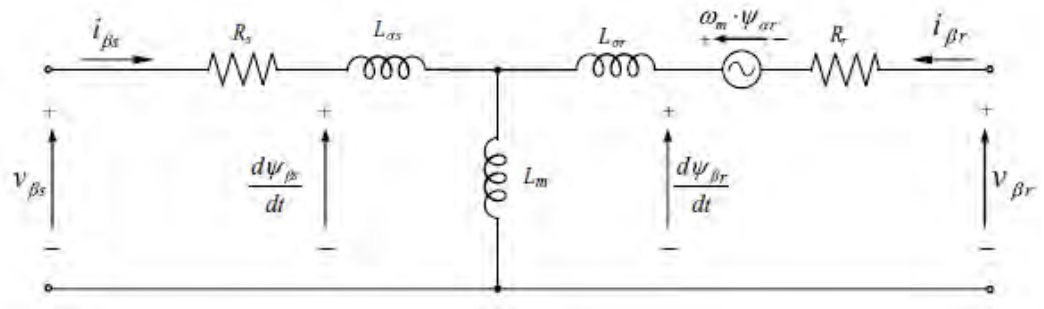

Figure2.11: Equivalent electrical model in the β reference frame [13]

Finally the electromagnetic torque is expressed as;

$$T_{em} = \frac{3}{2} I_m\{ \ _r . \tilde{\imath}_r^* \} = \frac{3}{2} (\ _{\beta r} i_{\alpha r} - \ _{\alpha r} i_{\beta r}) \quad (2.40)$$

2.5.2. Synchronous dq reference frame

In this section, the equations representing the DFIM will be derived in the synchronous reference frame by use of space vector notation as was done with the αβ model.

Equations (2.30) and (2.31) are multiplied by $e^{-j\theta_s}$ and $e^{-j\theta_r}$ respectively to yield

$$\tilde{v}_s^a = R_s \tilde{\imath}_s^a + \frac{d \ _s^a}{dt} + j \ _s \ _s^a \quad (2.41)$$

$$\tilde{v}_r^a = R_r \tilde{\imath}_r^a + \frac{d \ _r^a}{dt} + j(\ _s - \ _m) \ _r^a \quad (2.42)$$

Where $_s - \ _m = \ _r$

The same flux expressions from the αβ model are used [13];

$$_s^a = L_s \tilde{\imath}_s^a + L_m \tilde{\imath}_r^a \quad (2.38)$$

$$_r^a = L_m \tilde{\imath}_s^a + L_r \tilde{\imath}_r^a \quad (2.39)$$

As was mentioned in section 2.5.1 $\alpha\beta$ model components are time varying, that is, they are sinusoidal. But dq components on the other hand are not time varying, hence they are constant signals which is ideal for control systems [13].

The torque and power equations are shown below [13];

$$P_s = \frac{3}{2} Re\{\tilde{v}_s . \tilde{i}_s^*\} = \frac{3}{2}\left(v_{ds} i_{ds} + v_{qs} i_{qs}\right) \tag{2.43}$$

$$P_r = \frac{3}{2} Re\{\tilde{v}_r . \tilde{i}_r^*\} = \frac{3}{2}\left(v_{dr} i_{dr} + v_{qr} i_{qr}\right) \tag{2.44}$$

$$Q_s = \frac{3}{2} Im\{\tilde{v}_s . \tilde{i}_s^*\} = \frac{3}{2}\left(v_{qs} i_{ds} + v_{ds} i_{qs}\right) \tag{2.45}$$

$$Q_r = \frac{3}{2} Im\{\tilde{v}_r . \tilde{i}_r^*\} = \frac{3}{2}\left(v_{qr} i_{dr} + v_{ds} i_{qr}\right) \tag{2.46}$$

$$T_{em} = \frac{3}{2} \frac{L_m}{L_s} I_m\{ \quad_s . \tilde{i}_s^*\} = \frac{3}{2} \frac{L_m}{L_s}(\quad_{qs} i_{dr} - \quad_{ds} i_{qr}) \tag{2.47}$$

2.6. Control of Doubly Fed Induction Machine

Control techniques for the Doubly Fed Induction Machine will be looked at in this section. Two control techniques are discussed here, hysteresis current control and vector control. Under vector control there are two orientations in which the machine – side converter can be controlled, that is, stator flux orientation and grid voltage orientation. Both orientations will be discussed.

2.6.1. Hysteresis Current Control

In Hysteresis Current Control (HCC), the principle used is that of a lower current band and an upper current band forming what is called the hysteresis current band. This band determines the confines to which the output of the inverter output current is maintained [19].

The actual current from the inverter is compared to a reference current signal within the band. When the actual current crosses either the upper or lower current bands, a trigger signal is sent to the switches and state of the applicable inverter leg is inverted so as to keep the actual current as close to the reference current value as possible [19].

Below are diagrams showing the operation of HCC [20]

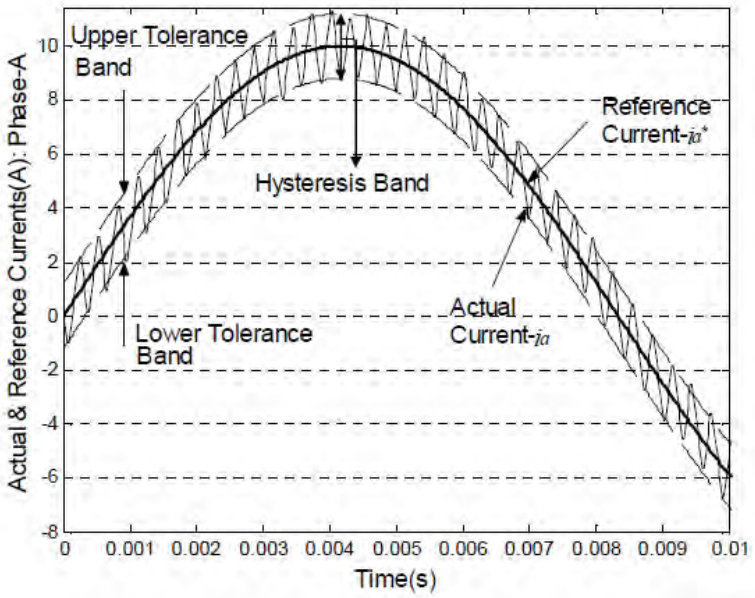

Figure 2.12: Actual and references currents verses time [20**]**

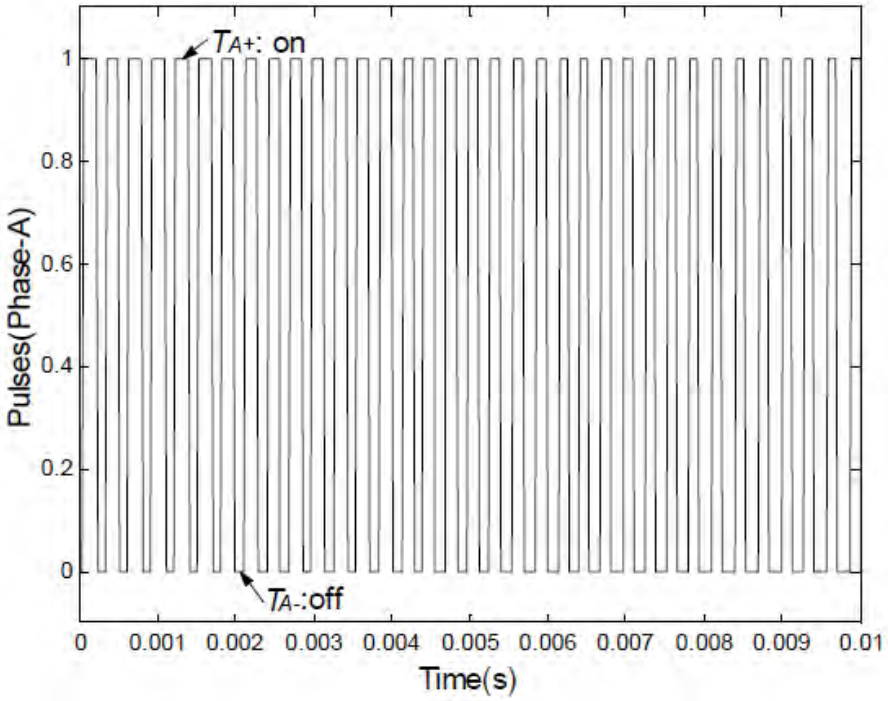

Figure 2.13: Pulses sent to the switches of the converter [20]

In order to maintain the actual current as close to the reference current value as possible, the hysteresis band has to be narrow. But there are some limiting factors to how narrow the band can be, and these are mentioned below;

- The Maximum frequency of the semiconductors used
- The sampling speed of the control
- The Operating speed of the control

This control has the advantage of inherent current control but due to it's requirement for current sensors and fast A/D conversion devices the control scheme is expensive to implement [19]. Further disadvantages that have led to this method not being used in this project are; the operation of this control is random and not smooth which could be damaging to the convertor, and the switching frequency changes with the alternating current wave form and is not constant [21].

2.6.2. Vector Oriented Control with stator Flux Orientation

Space vector control which forms the basis of the control for this project is now looked at in this section. Space vector control is based on aligning the rotor currents in the synchronous reference frame. But even under space vector control, one could align the stator flux to the d-axis, known as stator flux orientation. Or align the grid voltage to the q-axis, known as grid voltage (grid flux) orientation. The two are briefly discussed below.

Stator flux orientation

In stator flux oriented control, the stator flux linkage is aligned along the d-axis as shown in Figure 2.14 below [13].

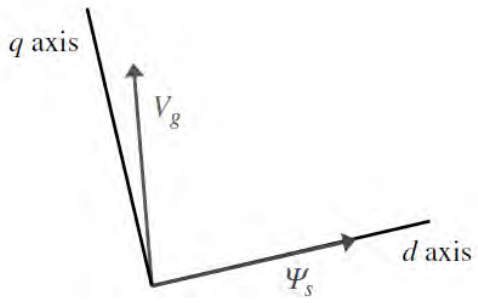

Figure 2.14: Stator Flux orientation [13]

In this orientation, the stator flux position angle is found by first finding the stator flux from stator current and voltage parameters. The stator flux position (angle) is then calculated.

It has been shown in [13] and [22] that the stator flux is influenced by the d component of the rotor current and may become unstable in certain conditions. Analysis in stator flux orientation conducted in [13] shows that during grid voltage unbalances the angle between the flux and the grid voltage, which is 90° under stable conditions, changes. This could render the control unstable if referenced in the stator flux orientation. In depth work on this has been done in [13] and [22].

2.6.3. Vector oriented control with Grid Voltage Orientation

In grid voltage orientation control, the grid voltage is aligned to the q-axis as shown in Figure 2.15 below.

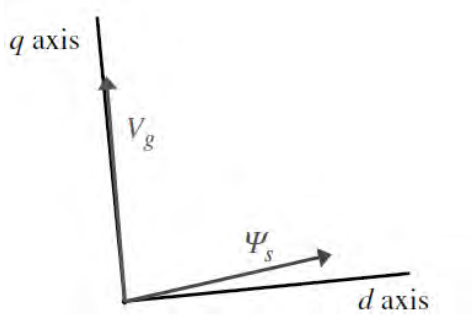

Figure 2.15: Grid Voltage orientation [13]

This method has been shown to be more stable in transient conditions. Further it is possible to produce more reactive power with this method and to operate at a unity power factor [22]. Vector control in grid voltage orientation has also been implemented successfully with fluctuation in the grid voltage in the work done by Choudhury et al [23].

2.6.4. Dual Vector Current Control

During voltage unbalances, standard vector control is not sufficient to ensure stable control. This is due to the fact that during voltage unbalances, a negative component arises in the current and the resulting disturbances in the current causes unbalance in the converter. Hence, for proper control during grid voltage unbalances, the following has to be taken into account and handled by the control algorithm [40];

- Distortion of line currents
- Oscillations in the DC Link
- Phase angle jumps and variations
- Variations in the amplitude of the voltage
- Unstable power factor

- Increase in harmonics in the system

In this section dual vector current control will be looked at. Below are the current vector transformations in the different reference frames [24].

$$I_{dq}^{+} = I_{\alpha s\beta s} e^{-j\omega st}$$

$$I_{dq}^{-} = I_{\alpha s\beta s} e^{j\omega st}$$

$$I_{dq}^{+} = I_{dq}^{-} e^{-2j\omega st}$$

$$I_{dq}^{-} = I_{dq}^{+} e^{2j\omega st}$$

$$I_{dq}^{+} = I_{\alpha r\beta r} e^{-j\omega slip+t}$$

$$I_{dq}^{-} = I_{\alpha r\beta r} e^{j\omega slip-t}$$

2.7. Grid Side Modelling and Control

In this section, the control of the grid side converter will be discussed. Similar to the modelling of the DFIM, firstly the steady state model is developed as well as the relationships between the active and reactive powers, and voltages and currents at the various modes of operation. The modelling techniques are again adapted from [13]

The main objective of the grid side converter is to control the DC Link voltage and reactive power exchange with the grid. The control used is of course vector control and will be achieved in the dq reference frame which is aligned to the grid voltage space vector. A Phase Lock Loop (PLL) is used to synchronise the signals. Details are outlined in the following subsections.

2.7.1. Steady State Model of the Grid System

A brief description of the steady state model of the grid is now given here. The figure below shows a simplified representation of the three-phase grid system.

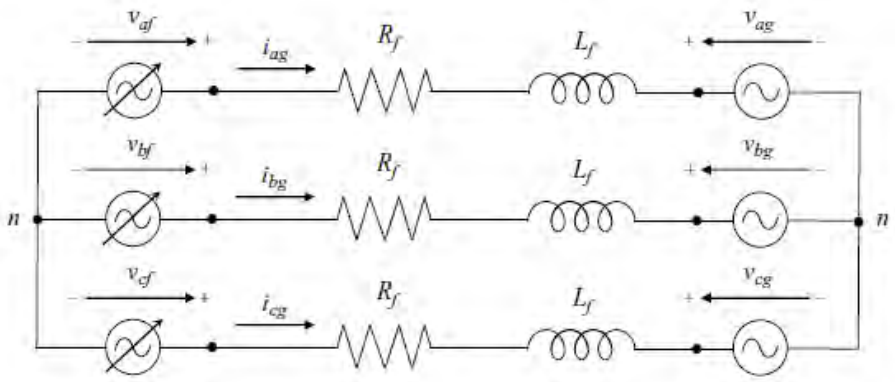

Figure 2.16: Simplified representation of three-phase grid [13]

The components are; the grid voltages v_{ag}, v_{bg}, v_{cg}, and the voltages from the grid side converter v_{af}, v_{bf}, v_{cf}, he filter resistance R_f and the filter inductance L_f. A simple L filter is sufficient for this grid model.

The Maximum voltage that can be obtained from the output of the converter is given by;

$$Max\ (v_{af})_1 = \frac{V_{bus}}{\sqrt{3}} \tag{2.48}$$

The electrical equation representing the system is;

$$V_{af} = V_{ag} + (R_f + jL_f\ \ _s)I_{ag} \tag{2.49}$$

The above equation can be used to model the circuit below. Since in steady state all the phases are considered equal, the simplified model shown in Figure 2.17, of a simple grid side is representative of each phase. P_g and Q_g can now be calculated as follows;

$$P_g = |V_{ag}| . |I_{ag}| . cos\varphi \tag{2.50}$$

$$Q_g = |V_{ag}| . |I_{ag}| . sin\varphi \tag{2.51}$$

P_g > 0 when the converter is delivering power to the grid and,

P_g < 0 when the grid is drawing power from the grid.

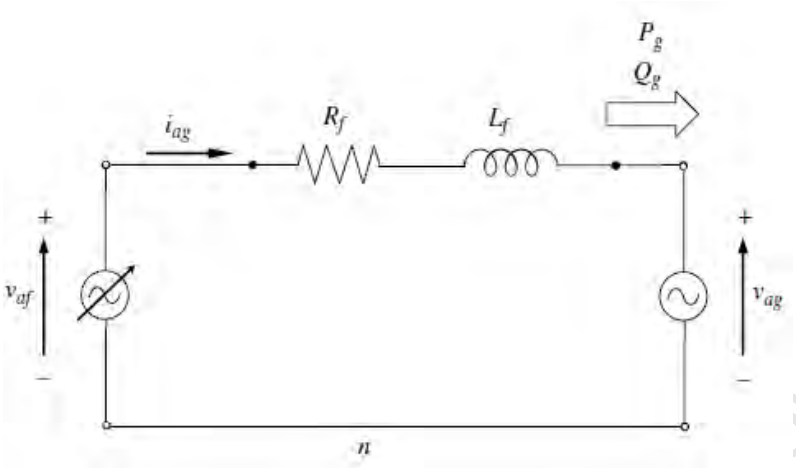

Figure 2.17: Single phase representation of a simple grid [13]

2.7.2. Dynamic Modelling of the grid

The grid will now be modelled using space vector notation first in the αβ and then in the dq frame. The electrical equations below are derived from Figure 2.17

$$v_{af} = R_f i_{ag} + L_f \frac{di_{ag}}{dt} + v_{ag} \tag{2.52}$$

$$v_{bf} = R_f i_{bg} + L_f \frac{di_{bg}}{dt} + v_{bg} \tag{2.53}$$

$$v_{cf} = R_f i_{cg} + L_f \frac{di_{cg}}{dt} + v_{cg} \tag{2.54}$$

These equations will form the basis from which both the αβ and dq models will be derived.

2.7.3. αβ Model

Equations (2.52), (2.53), and (2.54) are multiplied by $\frac{2}{3}$, $\frac{2a}{3}$ and $\frac{2a^2}{3}$ respectively to yield the following equations [13];

$$\frac{2}{3}v_{af} = \frac{2}{3}R_f i_{ag} + \frac{2}{3}L_f \frac{di_{ag}}{dt} + \frac{2}{3}v_{ag} \tag{2.55}$$

$$\frac{2a}{3}v_{bf} = \frac{2a}{3}R_f i_{bg} + \frac{2a}{3}L_f \frac{di_{bg}}{dt} + \frac{2}{3}v_{bg} \tag{2.56}$$

$$\frac{2a^2}{3}v_{cf} = \frac{2a^2}{3}R_f i_{cg} + \frac{2a^2}{3}L_f \frac{di_{cg}}{dt} + \frac{2a^2}{3}v_{cg} \tag{2.57}$$

These are added and the equations below are obtained [13];

$$v_{\alpha f} = R_f i_{\alpha g} + L_f \frac{di_{\alpha f}}{dt} + v_{\alpha g} \tag{2.58}$$

$$v_{\beta f} = R_f i_{\beta g} + L_f \frac{di_{\beta f}}{dt} + v_{\beta g} \tag{2.59}$$

When referred to a stationary reference frame, the above equations can be further reduced to give [13];

$$\tilde{v}_f^s = R_f \tilde{i}_g^s + L_f \frac{d\tilde{i}_g^s}{dt} + \tilde{v}_g^s \tag{2.60}$$

Where;

$$\tilde{v}_f^s = v_{\alpha f} + jv_{\beta f} \tag{2.61}$$

$$\tilde{v}_g^s = v_{\alpha g} + jv_{\beta g} \tag{2.62}$$

$$\tilde{i}_g^s = i_{\alpha g} + ji_{\beta g} \tag{2.63}$$

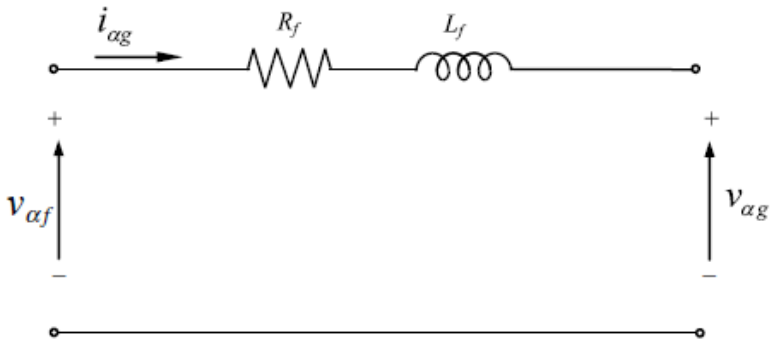

Figure 2.18: Alpha representation [13]

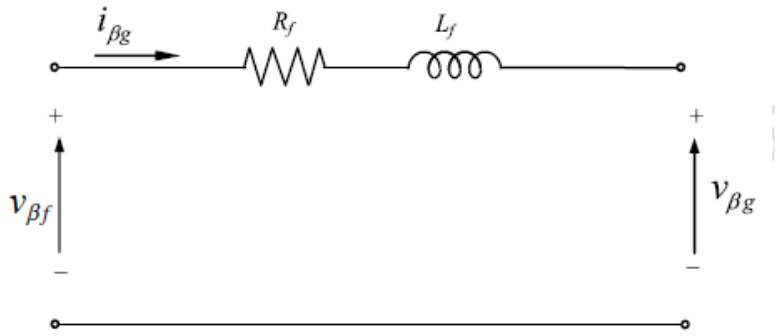

Figure 2.19: Beta representation [13]

2.7.4. DQ Model of Grid Side

Similar to deriving the dq model for the DFIM, equation (2.60) Is multiplied by $e^{-j\theta}$ as shown in equation (2.64) below which then gives equation (2.65)

$$\tilde{v}_f^s e^{-j\theta} = R_f \tilde{i}_g^s e^{-j\theta} + L_f \frac{d\tilde{i}_g^s}{dt} e^{-j\theta} + \tilde{v}_g^s e^{-j\theta} \tag{2.64}$$

$$\tilde{v}_f^a = R_f \tilde{i}_g^a + L_f \frac{d\tilde{i}_g^a}{dt} + \tilde{v}_g^a + j \ {}_a L_f \tilde{i}_g^a \tag{2.65}$$

And now to derive the components for the electric equivalent circuit, the following steps are taken;

It can be noticed that $\theta =$ ${}_{at}$, therefore we have;

$$\frac{d\tilde{i}_g^s}{dt} e^{-j\theta} = \frac{d(\tilde{i}_g^s e^{-j\theta})}{dt} + j \ {}_a \tilde{i}_g^s e^{-j\theta} \tag{2.66}$$

The dq components are;

$$\tilde{v}_f^a = v_{df} + jv_{df} \tag{2.67}$$

$$\tilde{v}_g^a = v_{dg} + jv_{qg} \tag{2.68}$$

$$\tilde{i}_f^a = i_{dg} + ji_{qg} \tag{2.69}$$

The equations for the vector orientation are then obtained and shown below;

$$v_{df} = R_f i_{dg} + L_f \frac{di_{dg}}{dt} + v_{dg} - {}_a L_f i_{qg} \tag{2.70}$$

$$v_{qf} = R_f i_{qg} + L_f \frac{di_{qg}}{dt} + v_{qg} + {}_a L_f i_{dg} \tag{2.71}$$

These can now be represented by the equivalent circuits in Figures 2.20 and 2.21. The figures show the dq model of the grid side system in stationary coordinates.

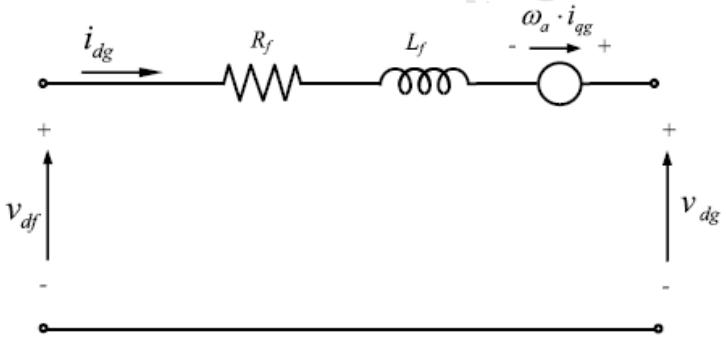

Figure 2.20: Direct-axis representation [13]

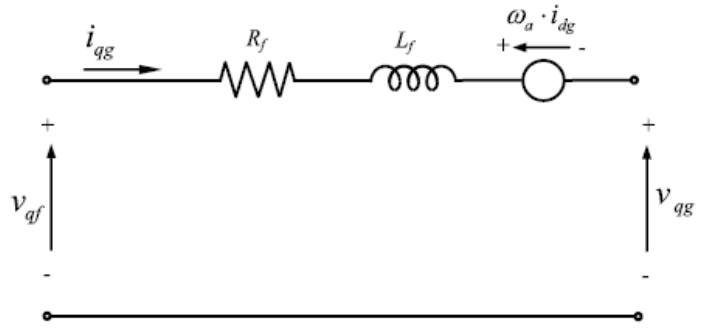

Figure 2.21: Quadrature-axis representation [13]

2.8. Filter Design

Adequate filtering is necessary at the output of the converter so as to limit current harmonics. These come about due to the non-sinusoidal nature of the PWM voltage wave forms [25].

The L filter has been used widely but it has been found that as the power ratings of the wind turbines increase, the L filter is no longer sufficient and can become quite costly as larger inductance is required [25]. The use of a 3rd order LCL filter helps reduce the inductor size. Details of the filter are looked at below.

2.8.1. LCL filter

In single phase, an LCL filter can be represented as shown in the Figure 2.22 below.

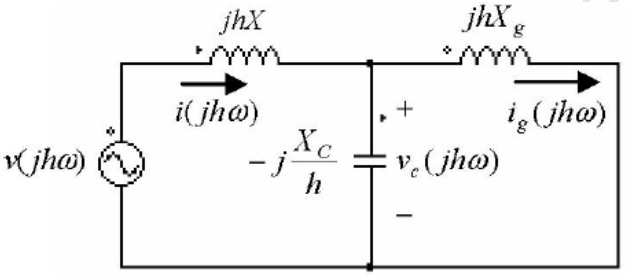

Figure 2.22: Single phase representation of LCL filter [25]

The reactances at fundamental frequency are defined as [25];

$$X = \omega L \tag{2.72}$$

$$X_g = \omega L_g \tag{2.73}$$

$$and\ X_c = \frac{1}{\omega C} \tag{2.74}$$

In three-phase it is connected as shown below;

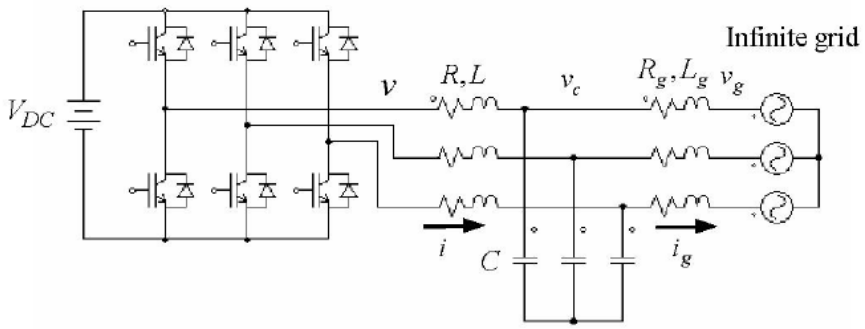

Figure 2.23: Three phase LCL filter connected to the converter and infinite grid [25]

From the above model, the transfer function starting from i_g to v in terms of jh can be obtained as follows;

$$H_{LCL}(jh\omega) = \frac{I_g(jh\omega)}{V(jh\omega)} = \frac{-j}{h\omega(-h^2\omega^2 LL_g C + L + L_g)} \tag{2.75}$$

The above can then be re-written using the reactance at fundamental frequency to obtain the equation below;

$$H_{LCL} = \frac{-j}{h[X + X_g - \frac{XX_g}{X_c}h^2]} \tag{2.76}$$

The magnitude is;

$$|H_{LCL}| = -\frac{1}{h[X + X_g - \frac{XX_g}{X_c}h^2]} \tag{2.77}$$

The LCL filter will now be modelled in the s – plane and the equations for the s – plane filter model are obtained from Figure 2.24: below and shown in the equations [26]

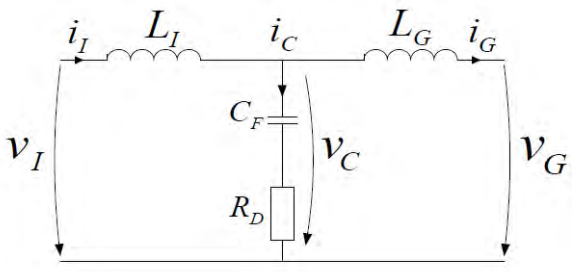

Figure 2.24: Single phase LCL filter [26]

$$i_L - i_C - i_G = 0 \tag{2.78}$$

$$v_I = i_I L_I s + v_C \tag{2.79}$$

$$v_G = -i_G L_G s + v_C \tag{2.80}$$

$$v_C = i_C\left(\frac{1}{C_F s} + R_D\right) \tag{2.81}$$

Where: v_I – inverter voltage

i_I – inverter current

L_I – inverter-side inductance

L_G – grid-side inductance

C_F – grid-side capacitance

R_D – damping series resistor

The filter is now represented as a block diagram in the s-plane (for single phase). The block diagram in given in Figure 2.25 below [26]

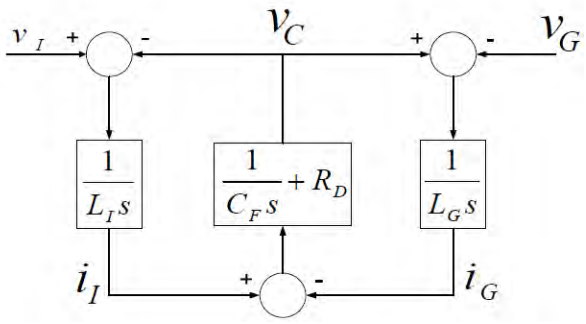

Figure 2.25: Block diagram of LCL filter [26]

The transfer function for the LCL filter in the s-plane is now derived from the information above. $v_G = 0$ for filter analysis;

$$v_I = z_{a1} i_I + z_{a2} i_G \tag{2.82}$$

$$v_G = z_{b1} i_I + z_{b2} i_G \tag{2.83}$$

$$z_{a1} = L_I s + \frac{1}{C_F s} + R_D \tag{2.84}$$

$$z_{a2} = -\left(\frac{1}{C_F s} + R_D\right) \tag{2.85}$$

$$z_{b1} = \frac{1}{C_F s} + R_D \tag{2.86}$$

$$z_{b2} = -\left(L_G s + \frac{1}{C_F s} + R_D\right) \tag{2.87}$$

$$H(s) = \frac{i_I(s)}{v_I(s)} = \frac{L_i C_F s^2 + R_D C_F s + 1}{L_I L_G C_F s^3 + R_D C_F (L_I + L_G) s^3 + (L_I + L_G) s} \tag{2.88}$$

In designing of the LCL filter, the following has to be taken into account [25];

- The ripple currents together with dominant frequency in the different components have to be carefully calculated.
- The closed-loop performance of the entire system has to be analyzed so as to access the influence of the filter on it.
- The resonance frequency also has to be looked at as well as the size of the filter and the cost.

Hence, even though the LCL has a superior harmonic attenuation, it is much more complicated to design as opposed to the L filter.

The LCL Filter will be used in this project however, because of its superior harmonic attenuation and because the system in the project is meant to emulate a larger scale system.

3. Software and Hardware design for Simulation and Experimental Setup

3.1. Introduction

This chapter will outline the software models used in MATLAB/Simulink as well as the hardware setup for the experimental aspect of the project. The MATLAB/Simulink model was developed by the author and the experimental setup was assembled by the author. This fulfils the objective of developing a DFIG system that can be used for grid integration studies.

3.2. Overall system of the Doubly Fed Induction Generator

The schematic of the overall system of the DFIG as it is implemented in software is shown in Figure 3.1. The sections which follow, will present more details about the components of the system. The LCL filter used will be discussed below in section 3.3. The design procedure and filter parameter limitations will be presented followed by the schematic of the grid-side converter as it is set-up experimentally. The Phase Lock Loop (PLL) which is used for the correct synchronising of the grid angle and the inverter angle is presented. A block diagram of the PLL is also provided.

3.3. LCL Filter Parameter limitations and Design Procedure

This section will outline the limitations in the selection of the LCL filter parameter values as well as the procedure followed in the design and calculation of parameter values. This procedure is also used and verified by experimentation in [27]. Table 3.1 below gives the parameters of the system being considered.

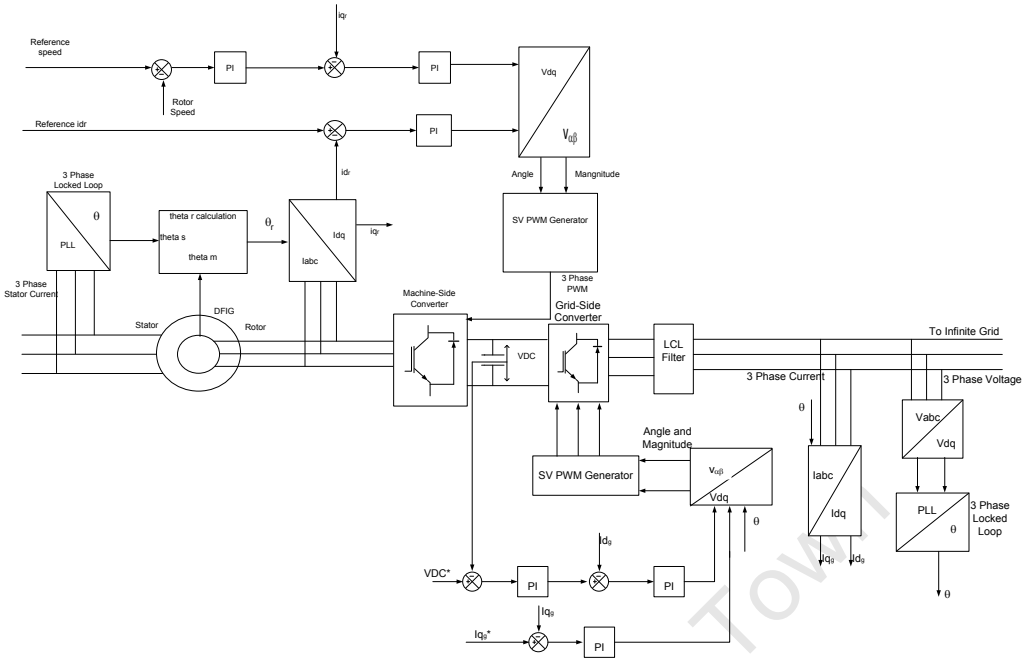

Figure 3.1: Schematic of system implemented in Matlab Simulink

Table 3.1: Specifications of system under consideration

Specification	**Value**
Grid Voltage (line to line) E_n	380V
Output Power P_n (Rotor side)	500W
DC Link Voltage V_{DC}	300V
Line Frequency f	50 Hz
Switching Frequency f_s	5KHz

When choosing LCL filter parameter values, one of the criteria to be considered is that reactive elements should be limited. This is because these elements result in power losses and poor power factor.

Limitations on the LCL filter parameter values [27]

- The value of the capacitor is limited by the power factor decrease at the rated power. This decrease is usually 5% or less.
- In order to limit the ac voltage drop during the system operation, the total inductance value should be chosen so that it is less than 0.1 pu. Higher values will require a higher DC Link voltage to ensure current controllability which leads to higher switching loss.
- To avoid resonance problems in lower and upper parts of the harmonic spectrum, the resonant frequency must be between ten times the grid (line) frequency and half the switching frequency.
- Passive damping should be enough to avoid oscillation. But care should be taken so as not to impede the efficiency of operation.

LCL filter design procedure [27]

1) As was mentioned in limitation 2 above, the converter side inductor is selected. The value of the grid side inductor can be selected so as to be related to L as follows;

$$L_g = rL \tag{3.1}$$

Where;

$$\frac{i_g(h_{sw})}{i(h_{sw})} = \frac{1}{|1+r(1-a.x)|} \tag{3.2}$$

The above equation is the current ripple attenuation and $a = LC_b\omega_{sw}^2$.

2) The capacitor value is determined as follows;

$$C_f = xC_b \tag{3.3}$$

where x is the percentage of the reactive power absorbed under rated conditions.

3) The resonant frequency is obtained by the equation below;

$$\omega_{res} = \sqrt{\frac{L_T}{LL_gC_f}} \tag{3.4}$$

4) The damping resistor is selected so as to satisfy limitation number 4 above [27].

After consideration of the above, the filter values selected are tabulated in Table 3.2 below.

Table 3.2: LCL filter parameters

Parameter	**Value**
Inverter-side inductance L_i	3 mH
Grid-side inductance L_g	6 mH
Filter capacitance C_f	2.4 μF
R_D(damping resistor)	1.4 Ω
Resonant frequency f_{res}	1916 Hz

3.4. Grid – Side Converter Control

Vector control is used to control the grid – side converter with the LCL filter connected to it. The grid – side converter control aims to maintain the DC Link voltage and to regulate the active and reactive power injected into the grid. It also employs a Phase Locked Loop (PLL) to synchronize the grid signals and the inverter signals. The LCL filter ensures that the power delivered to the grid is of high quality.

Vector control on the grid side is inherently grid voltage oriented and the active and reactive powers are governed by the following equations;

$$P = \frac{3}{2}(v_d i_d) \tag{3.5}$$

$$Q = \frac{3}{2}(v_d i_q) \tag{3.6}$$

In stable grid conditions when the there is no variation in the grid voltage frequency, amplitude and phase angle, the aim of the control is to ensure that only active power is delivered to the grid, whilst keeping the reactive power at zero. This is done to achieve unity power factor operation and the DC Link voltage must be maintained at a constant value. Figure 3.2 shows the grid–side converter and its control that was implemented in Matlab/Simulink.

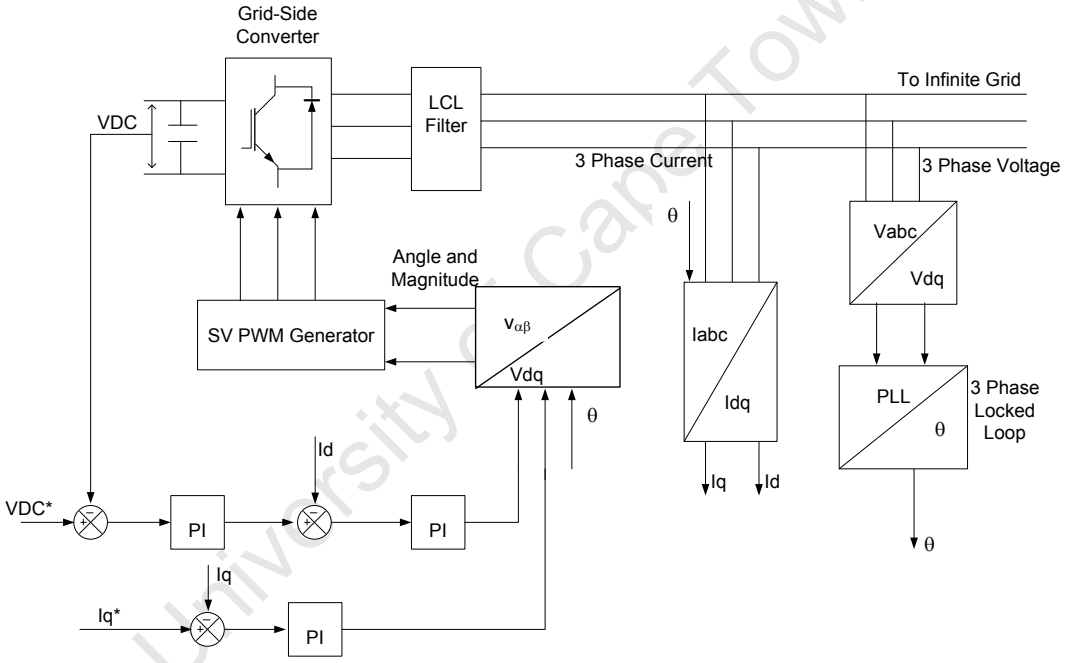

Figure 3.2: Schematic of grid – side converter control implemented in Matlab Simulink

3.4.1. Phase Locked Loop

The phase locked loop is used to provide the inverter with the frequency and the phase angle of the grid, that is, it synchronizes the angle of the grid voltage to that of the inverter [28].

Below is the block diagram of a PLL. Details of the derivatives of the transfer functions can be found in [28]

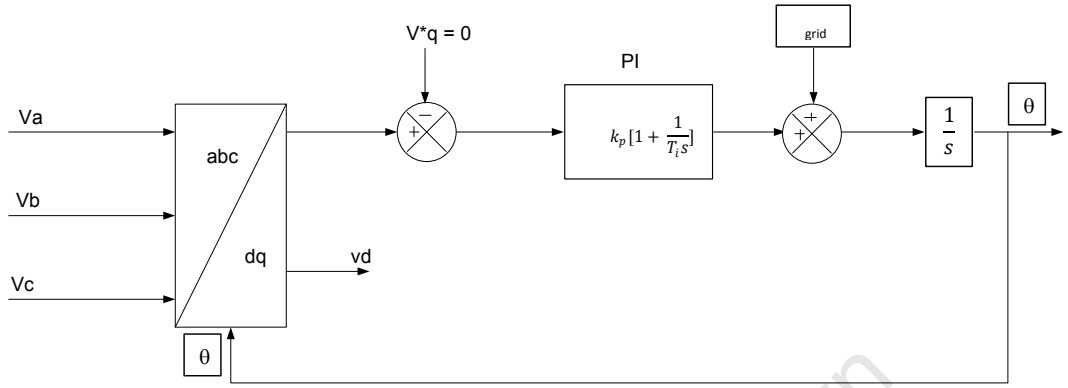

Figure 3.3: Phase Locked Loop (PLL) diagram [28]

3.4.2. PI Controllers

Figure 3.2 above shows a PLL with a PI controller in use. Proportional Plus Integral (PI) controllers are used because of the speed of controllability. The block diagram of a controller is shown below [28].

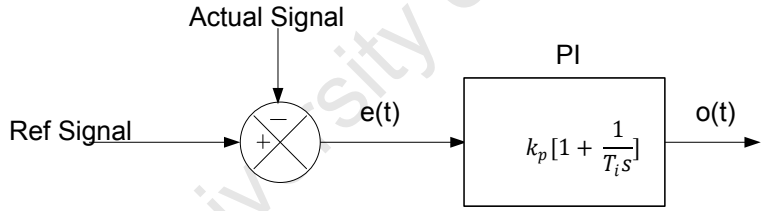

Figure 3.4: Proportional Plus Integral (PI) Controller diagram

The transfer function of the PI controller can be obtained from the diagram above.

$$G_{PI} = K_p[1 + \frac{1}{T_i s}] \tag{3.7}$$

Where K_p is the proportional gain, and T_i is the integral gain [28].

3.5. Rotor – Side Converter Control

The rotor-side converter regulates the rotor speed and torque. This control is conducted in the synchronously rotating (dq) reference frame which was derived in

chapter 2. Furthermore, the machine control is actualized in the grid voltage orientation. That is, the grid voltage vector is aligned with the q-axis whereas in the stator orientation, the stator flux is aligned with the d-axis. In grid voltage orientation, a PLL is required for synchronization of the parameters. The two orientations have been discussed in **Chapter 2**, sub sections **2.6.2** and **2.6.3**.

Below is a schematic of the rotor side converter control that was developed using vector control in grid voltage orientation.

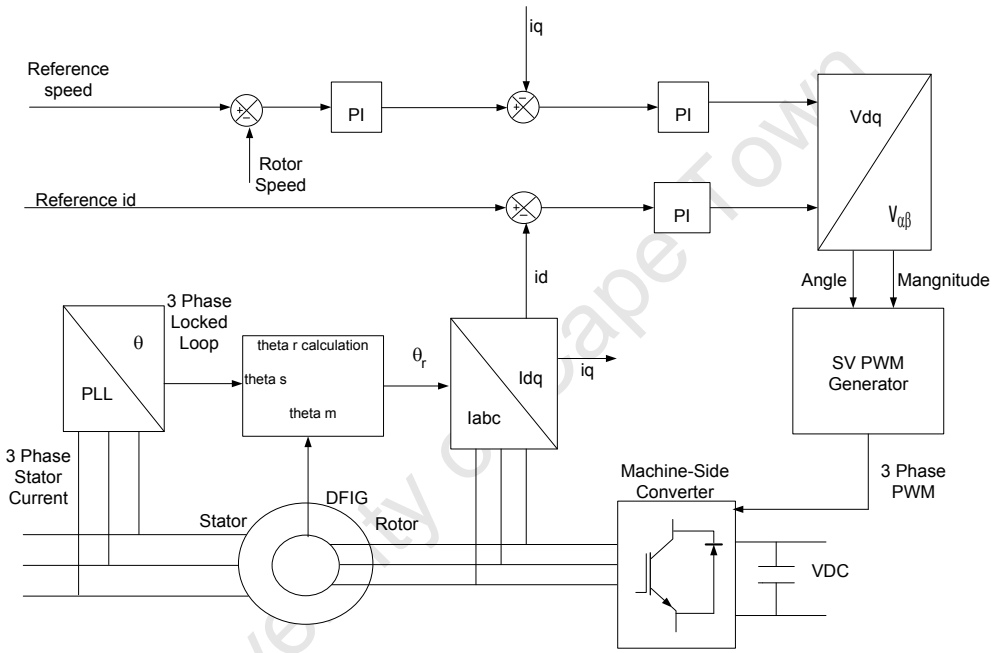

Figure3.5: Schematic of rotor – side converter control implemented in Matlab Simulink

3.6. Hardware set-up

This section gives a detailed description of the experimental set-up and some of the components in the set-up.

The overall system consists of a Wound Rotor Induction Machine (WRIM) connected as a doubly fed induction generator, a DC machine and drive, back to back converter and complementing components, two dSpace kits and two Personal Computers (PCs). The schematic of the experimental setup showing how all these components are inter-

connected, is shown in Figure 3.6 below. The main hardware components will be discussed in this section.

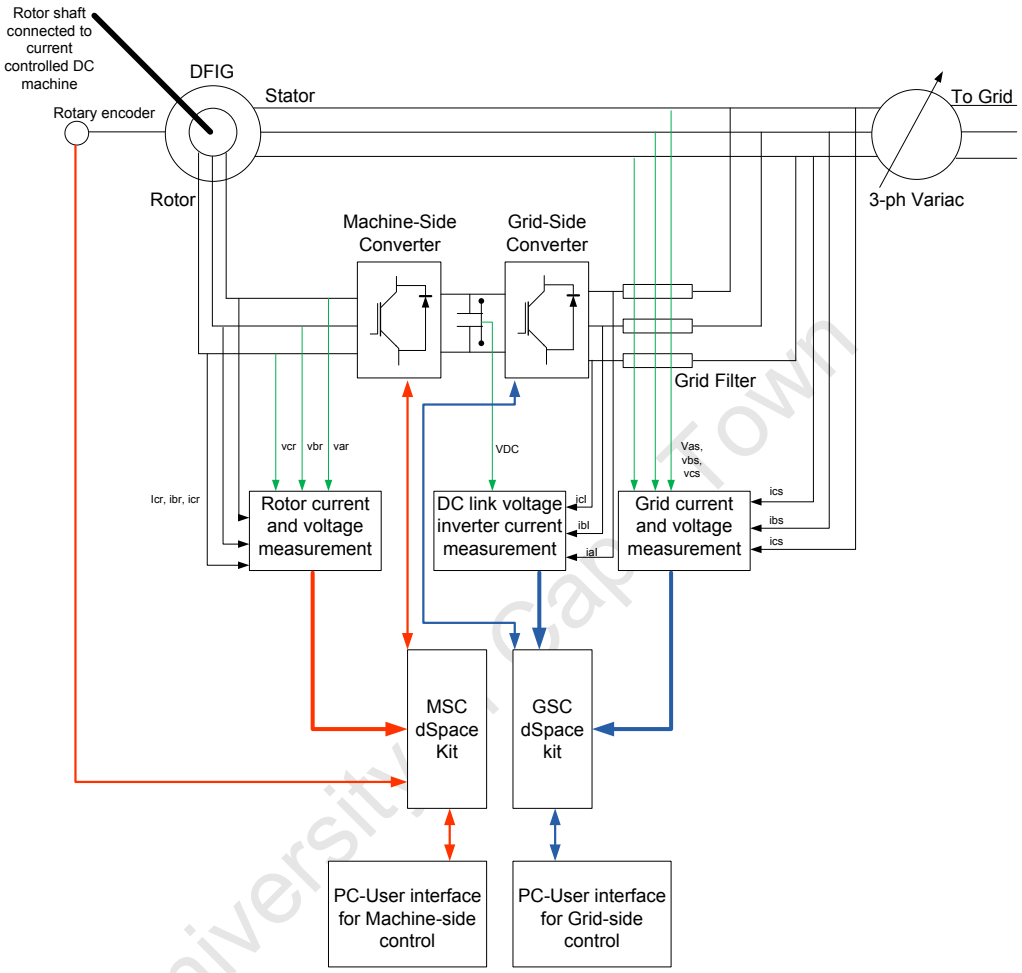

Figure 3.6: Schematic of experimental set-up of doubly fed induction generator connected to the grid

3.6.1. Three - Phase wound rotor induction machine (WRIM)

The machine used in this project is a 3-phase, 2.2 kW, 380 V, 50 Hz, 4-pole wound rotor induction machine. It has a rated speed of 1500 rpm (157 rads/s) and the actual machine used is shown in Figure 3.7 below.

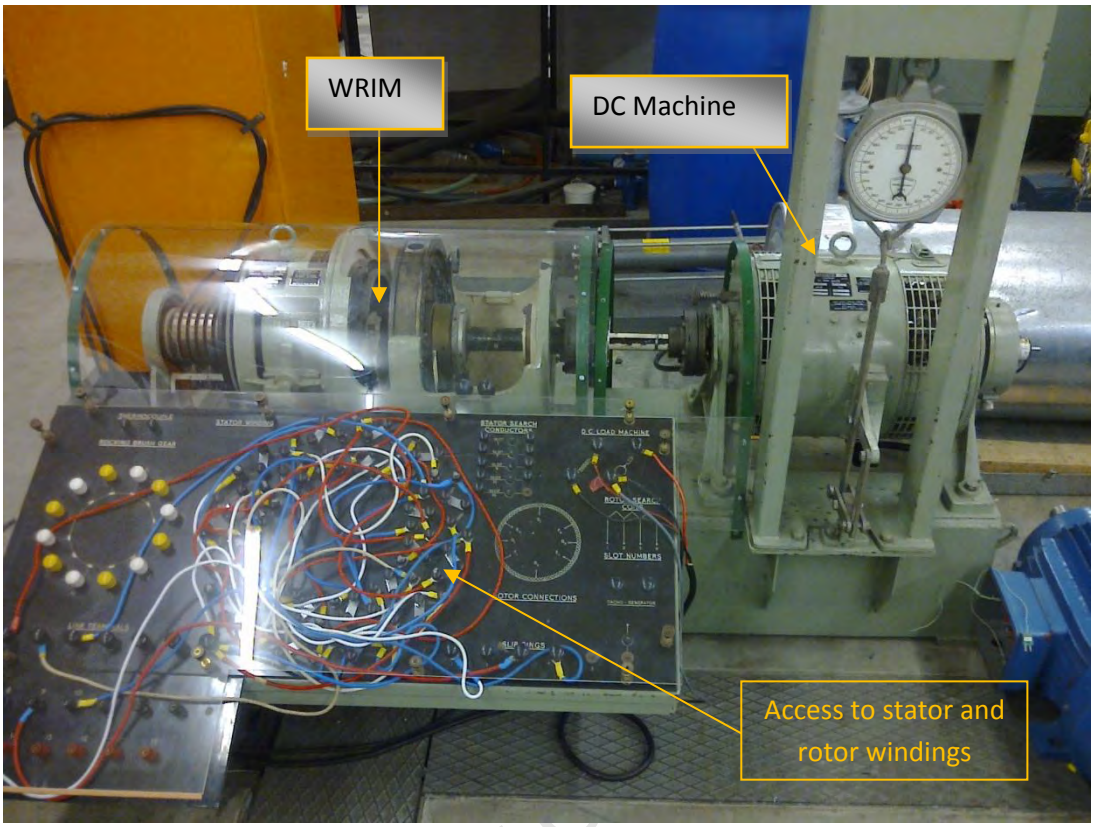

Figure 3.7: Wound rotor induction machine and DC machine

The 'No load' and 'Blocked rotor' tests are performed in order to obtain the equivalent circuit parameters of the WRIM. The IEEE recommended steady state per-phase equivalent circuit for the induction machine is shown in Figure 3.8 below.

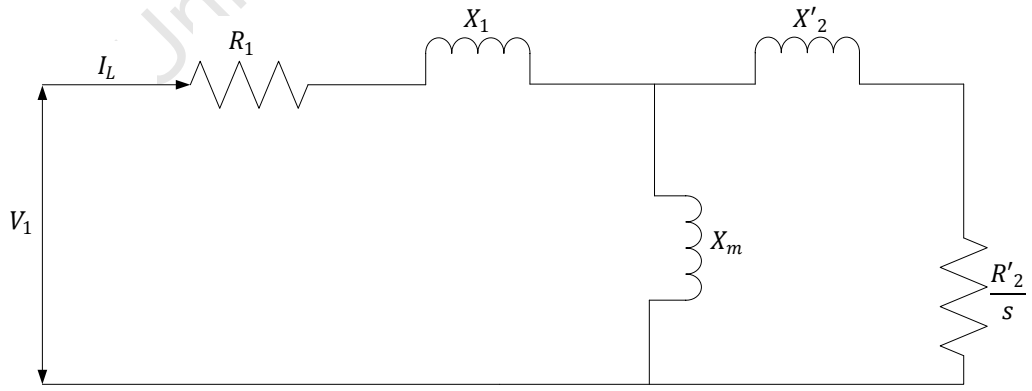

Figure 3.8: IEEE recommended steady-state per-phase equivalent circuit of an Induction machine

The parameters for the above circuits are as follows;

V_1 – Line to neutral voltage

I_L – Line current

R_1 – Stator resistance

X_1 – Leakage reactance

X_m – Mutual flux linkage common to both the stator and rotor

R'_2 – Rotor leakage reactance transferred to the stator

A. No load test

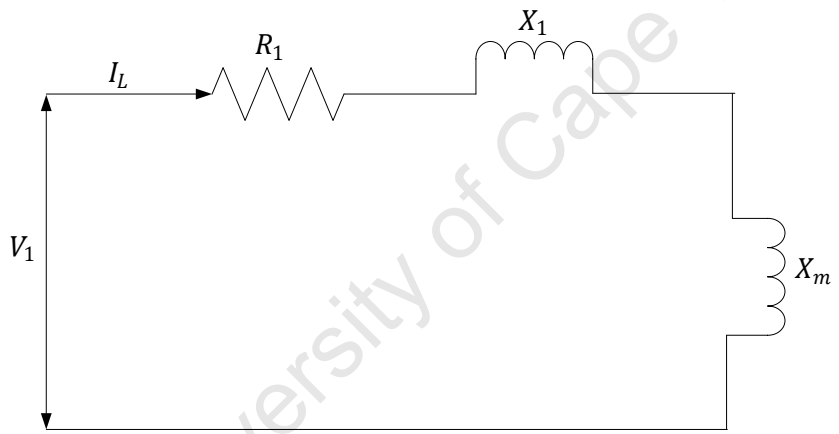

Figure 3.9: IEEE recommended steady state per-phase equivalent circuits for No load test

In this test the rotor is not coupled with any load and rated voltage at the rated frequency is applied to the stator windings. The rotor windings are shorted circuited. Below are the measured and calculated parameters;

Measured:

$V_{LL} = 414\,V$, $I_L = 2.5\,A$, $P_{TOT} = 197\,W$, $R_1 = 1\,\Omega$

Where V_{LL} is the line to line voltage, P_{TOT} is the total power.

Calculated parameters;

Line to neutral voltage $V_1 = \frac{V_{LL}}{\sqrt{3}} = \frac{414}{\sqrt{3}} = 239\ V$

Per – phase power $P_{PH} = \frac{P_{TOT}}{3} = \frac{197}{3} = 65.7\ W$

Per – phase apparent power $S_{PH} = \frac{V_{LL}I_L}{\sqrt{3}} = \frac{414\ x\ 2.5}{\sqrt{3}} = 597\ W$

Per – phase reactive power $Q_{PH} = \sqrt{S_{PH}^2 - P_{PH}^2} = 594\ var$

Per - phase rotational power loss $P_{\frac{rot}{PH}} = P_{PH} - I_L^2 R_1 = 59\ W$

No load impendence $Z_{NL} = \frac{V_1}{I_L} = 95.6\ \Omega$

No load resistance $R_{NL} = \frac{P_{PH}}{I_L^2} = 10.5\ \Omega$

B. Blocked Rotor test

In this test the rotor shaft is locked such that it is unable to rotate. Rated current is applied at the stator terminals and the following are the measured and calculated parameters.

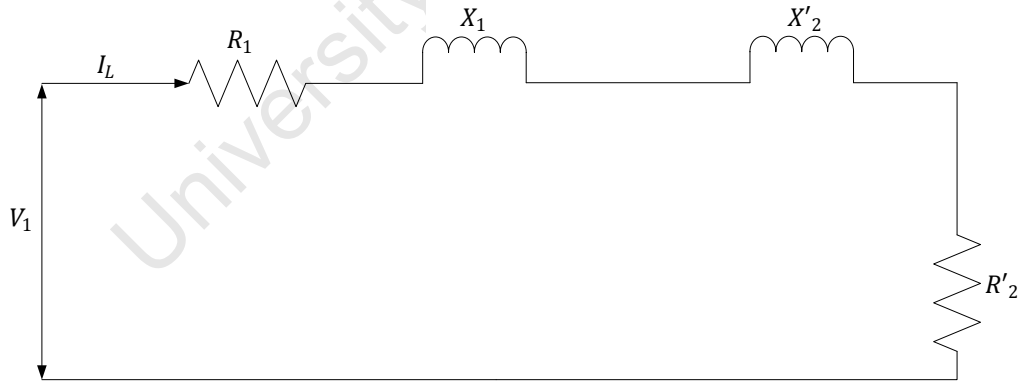

Figure 3.10: IEEE recommended steady state per-phase equivalent circuits for Blocked rotor test

Measured:

$V_{LL} = 85\ V$, $I_L = 4.6\ A$, $P_{TOT} = 301\ W$, $R_1 = 1\ \Omega$

Calculated parameters;

Line to neutral voltage $V_1 = \frac{V_{LL}}{\sqrt{3}} = \frac{85}{\sqrt{3}} = 49\ V$

Per – phase power $P_{PH} = \frac{P_{TOT}}{3} = \frac{301}{3} = 100\ W$

Per – phase apparent power $S_{PH} = \frac{V_{LL}I_L}{\sqrt{3}} = \frac{85\ x\ 4.6}{\sqrt{3}} = 225.7\ W$

Per – phase reactive power $Q_{PH} = \sqrt{S_{PH}^2 - P_{PH}^2} = 202\ var$

Blocked rotor Resistance $R_{BL} = \frac{P_{PH}}{I_L^2} = 4.7\ \Omega$

$R = R_{BL} - R_1 = 3.7\ \Omega$

Blocked rotor impendence $Z_{NL} = \frac{V_1}{I_L} = 10.7\ \Omega$

Blocked Rotor reactance $X_{BL} = \sqrt{Z_{BL}^2 - R_{BL}^2} = 9.6\ \Omega$

$X_1'\ and\ X_2'$ $X_1' + X_2' = X_{BL}\ \Omega$

$X_1 = X_2' = 4.8\ \Omega$

Magnetizing reactance $X_m = X_{NL} - X_1 = 90.2\ \Omega$

Rotor resistance $R_2' = [\frac{X_2' + X_m}{X_m}]^2 = 1.11\ \Omega$

With these values, the complete equivalent circuit of the induction machine with parameters is shown in Figure 3.11 below.

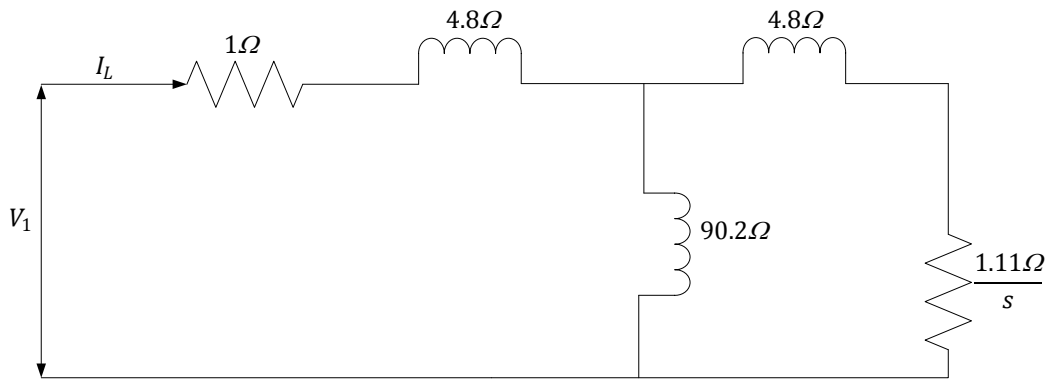

Figure 3.11: IEEE recommended steady-state per-phase equivalent circuit for induction machine with circuit parameters.

3.6.2. DC Machine and Drive

A 3 kW DC machine is used to emulate the turbine blades by exerting a torque on the shaft of the rotor of the DFIG. This is achieved in current control mode of the DC Machine. The drive used is a two quadrant drive.

3.6.3. Rotary Encoder

An incremental encoder is used to measure the rotor position and speed. A rotary encoder is a photo sensing device that is used to convert a mechanical changing amount into an electrical signal/pulse [29]. The encoder used in this project is an LS Mecapion S40 model. It has a resolution of $3000\ \frac{P}{R}$ and a maximum speed of 7000 rpm. Detailed specifications of the encoder can be found in the appended data sheet in Appendix C.

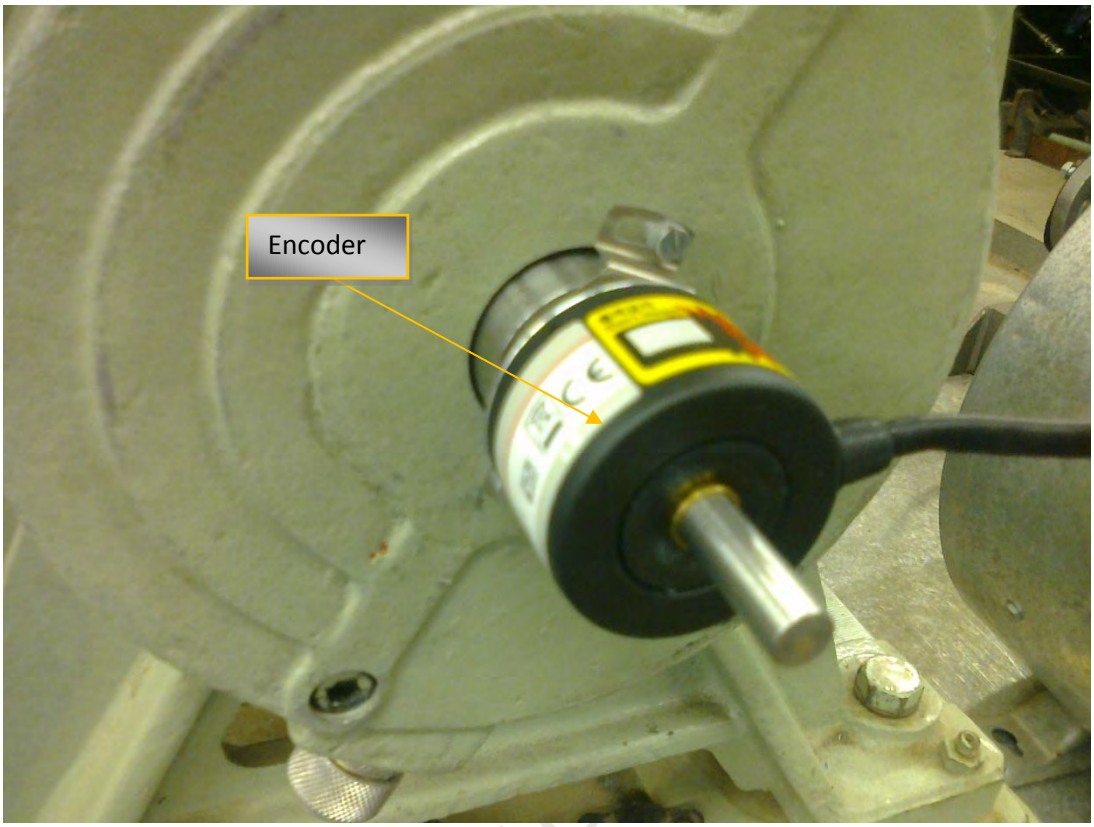

Figure 3.12: Incremental type rotary encoder

3.6.4. Converters

The back to back full-bridge converter is connected to the rotor windings of the DFIG. One converter is on the rotor-side and forms part of the machine – side control and the other converter is connected to the supply side and forms part of the grid – side control. The two converters are electrically separated by a capacitor bank which forms the DC link.

Each converter consists of 3 IGBTs (each half bridge has two switches) and 3 drivers to output signals to the switches according the control generated PWM waves.

3.6.5. Insulated Gate Bipolar Transistors (IGBTs)

Insulated Gate Bipolar Transistors (IGBTs) are semiconductor devices used for switching according to the PWM signals generated by the control. These signals are

received by the drivers from the dSpace kits. Details of these are explained in subsequent sections.

IGBTs have the advantage of being able to switch at very high speeds and this reduces the cost of other components connected to them such as transformers, inductors and capacitors. They can also handle much larger collector currents when compared to other semiconductor devices. This means they are able to have higher power ratings [30]. The rating of the IGBTs used for this project is 50 A.

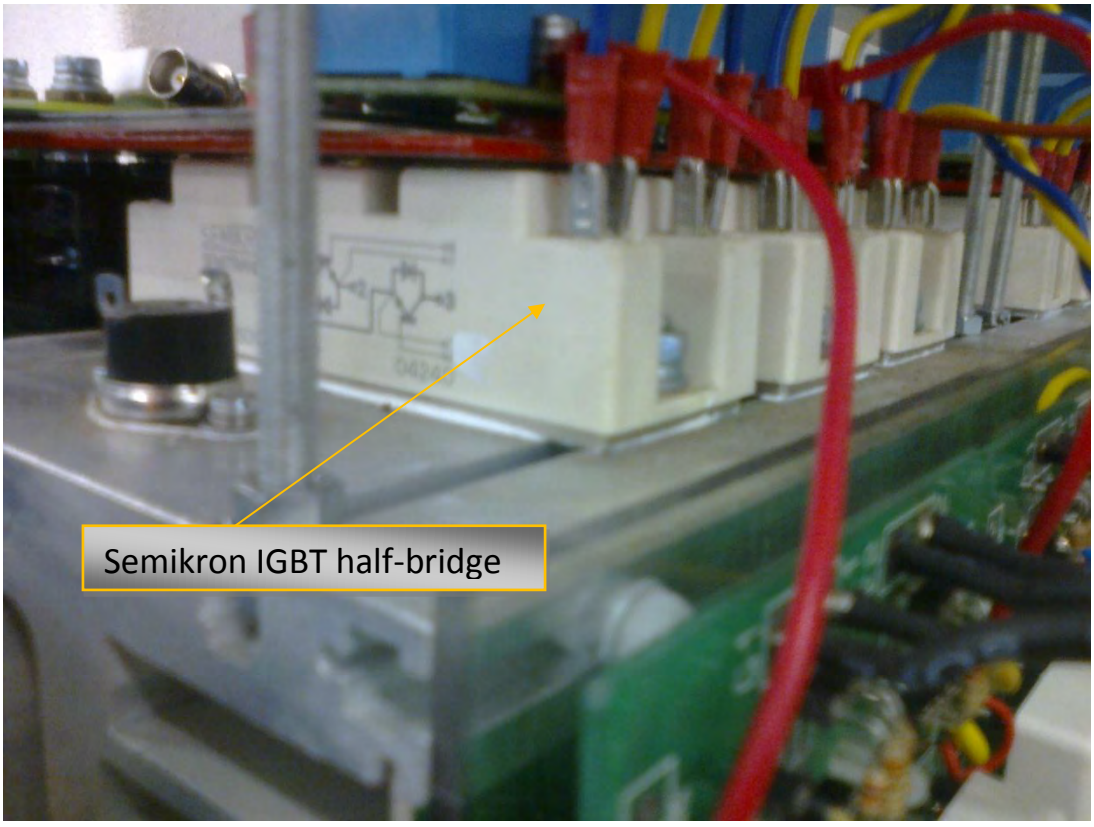

Figure 3.13: Semikron IGBT half-bridge mounted on heat sink of back to back converter

3.6.6. Drivers

The back-to-back converter has 6 drivers each driving the switches of a leg (two switches) as shown in Figure 3.14. When one switch on a leg is on, then the other switch on the same leg will be off. Two switches on the same leg are never on at the same time in order to prevent a short circuit across the DC Link. The driver modules

therefore insert a built-in dead-time between turn-off and turn-on of corresponding switches of the same leg to same leg of the converter.

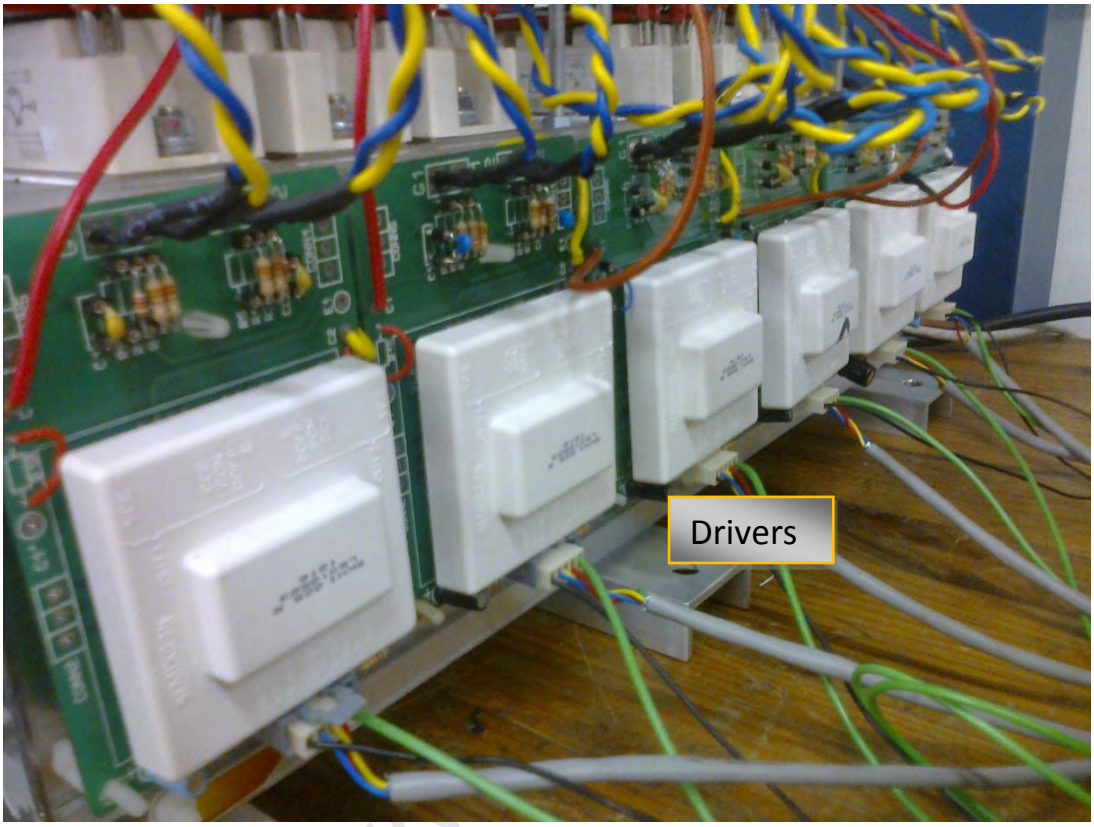

Figure 3.14: Drivers mounted on heat sink of the back to back converter and connected to Semikron half-bridge IGBTs

3.6.7. Voltage and Current measurements

The voltage and current signals from the experimental system have to be constantly measured and fed into the control via ADCs on the dSpace kits, where they are compared with the reference signals, in order to generate the appropriate control action.

Voltage and current measurements in this project are done by using the LV 25-P and LA 25-NP for voltage and current measurements respectively. The data sheets of the voltage and current transducers can be found in Appendix D. The diagrams below show how the LEM voltage and current modules are connected.

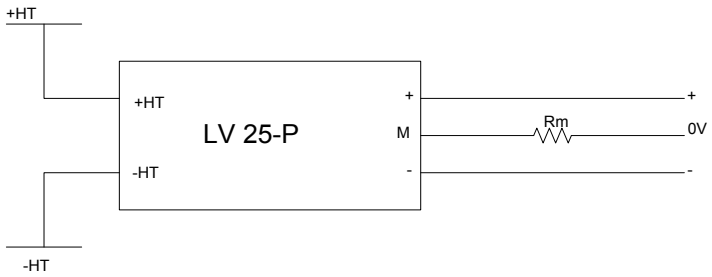

Figure 3.15: Voltage LEM module

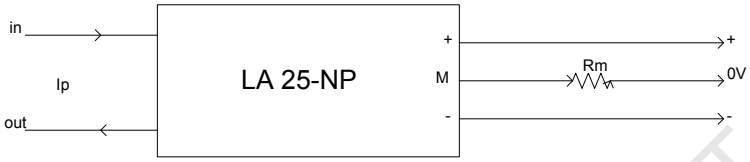

Figure 3.16: Current LEM module

Advantages of the LV 25-P and LA 25-NP according to their data sheets in APPENDIX D, are that they have precise accuracy and linearity, a low temperature drift and optimized response time. They also have a wide frequency bandwidth and no insertion losses. The LV 25_NP and LA 25-NP have a high immunity to external interference and have capacity for current overload.

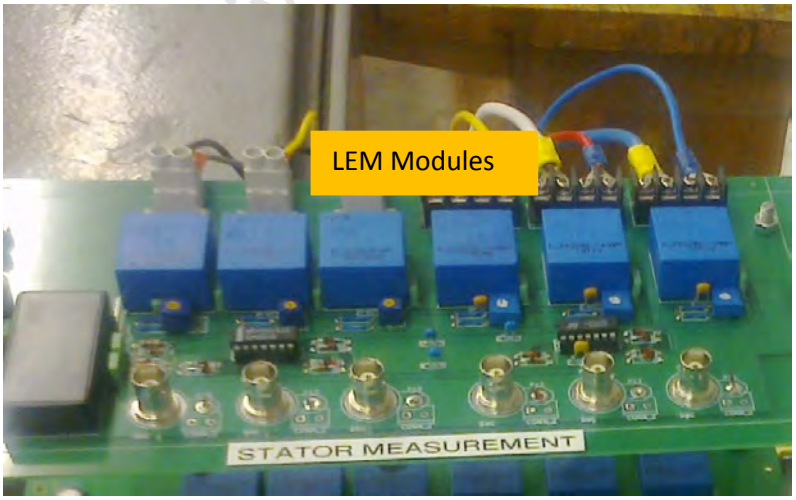

Figure 3.17: Voltage and Current LEM modules

Figure 3.17 above shows the LEM modules connected on a circuit board. They have to be supplied by an external voltage of $\pm 15\ V$.

A. Selection of external devices to be connected to the LV 25-P

Voltage transducer LV 25-P is used to measure the DC Link voltage and the stator voltages. On the primary side, the LV 25-P has a current rating I_p that has to be kept within $\pm 14\ mA\ or\ \pm 10\ mA$ which is $\pm I_{pmax}$. For the purposes of this system, $\pm I_{pmax}$ is chosen to be $\pm 14\ mA$.

The equation below is used to calculate the resistance R_p that is chosen to maintain the primary current within this range.

$$R_p \geq \frac{V_1}{I_{pmax}}$$

On the secondary side, the secondary current that is in the secondary coil is scaled by (2500:1000) of the primary current.

$$I_m = I_p\ x\ 2.5$$

But the readings obtained from the LV 25-P are voltage measurements, I_m has to be converted to voltage V_m which is then measured on the secondary side as;

$$V_m = I_m\ x\ R_m$$

R_m is in the range 100 Ω - 190 Ω, therefore, a 200 Ω potentiometer is chosen.

DC Link Voltage Measurement

The maximum DC Link voltage is chosen to be 600 V. From equation, R_p is calculated to be 42.857 kΩ, in order to maintain I_p as 6 mA, R_p is chosen to be 100 kΩ. I_m is then calculated to be 15 mA and R_m is chosen to be 150 Ω and $V_{m\ max}$ is set to 2.25 V.

Stator and Rotor Voltage Measurement

Other voltage signals to be measured are the V_{LL}, line to line voltages of the stator and rotor. Using the same procedure as was used for DC Link voltage. V_{LL} for the stator is 380V and for rotor is about 100V. A 20 % error region is allowed to avoid the saturation of the transducers. Hence the stator and rotor line to line voltages become 456 V and 120 V respectively. The same device parameters used for the DC Link Voltage are chosen for the Stator LV 25-P external devices.

B. Selection of external devices to be connected to the LA 25-NP

In the LA 25-NP, the secondary current I_m flowing through Rm is scaled down from the primary current I_p by K. K is the scaling factor and it is chosen to be 0.002. The relationship between I_m and I_p is as shown by the equation below;

$$I_m = I_p \, x \, K$$

R_m is found by the following equation;

$$R_m = \frac{V_m}{I_m}$$

R_m is chosen so that the output voltage stays within the input range of the ADC which is $\pm 10\ V$. The same external values are selected for the stator and rotor LEM module settings.

$$I_{rated\ (rms)} \sqrt{2}\ x\ 4.73 = 6.69\ A$$

$$I_m = 6.69x\ 0.002 = 13.38\ mA$$

R_m is found to be 500 Ω and Vm is calculated as 6.69 V. This value is within the $\pm 10\ V$ that is the input range of the ADC on the dSpace kit.

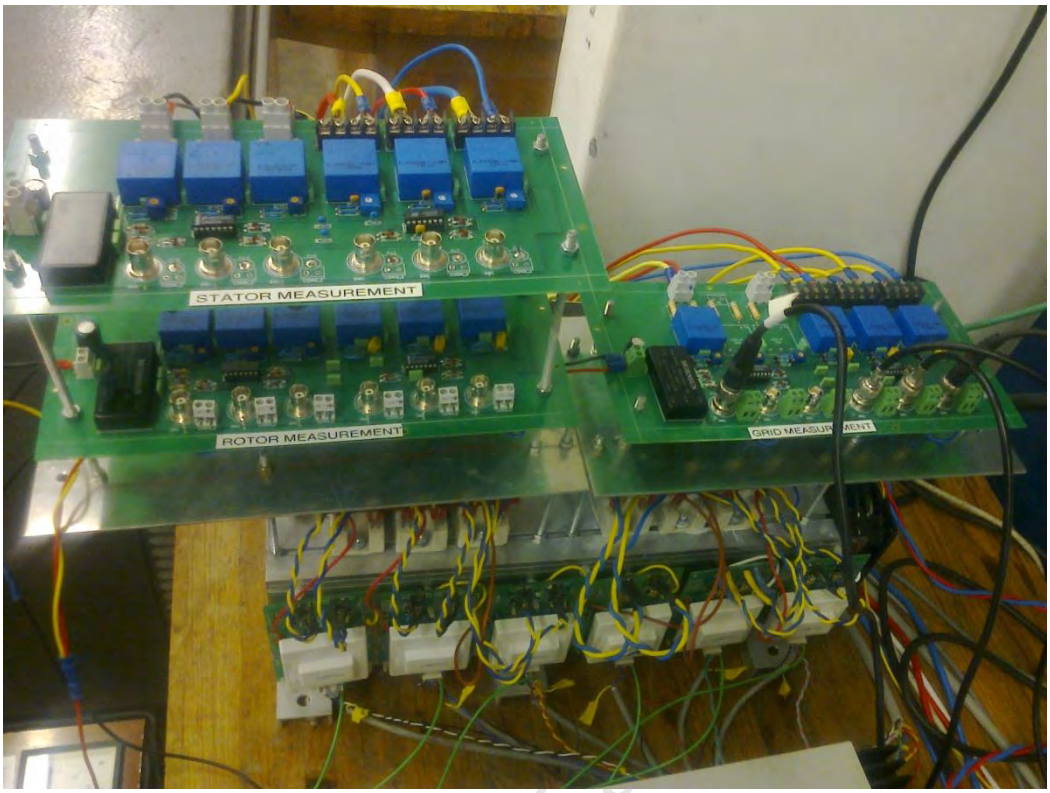

Figure 3.18: Stator, rotor and grid measurement boards using LEM modules

3.6.8. System protection

Any system requires electrical protection so as to avoid hazardous working conditions and to prevent damage of the equipment. Figure 3.19 below shows some of the protection components used to protect the experimental set-up. The machine components shown below are the fuses, contactors, the isolator and three phase circuit breaker. The signals going through the system are monitored by the relays. The relays energize the contactors when these signals go over the specified thresholds; which in turn break the circuit, thereby isolating the system being protected from over currents.

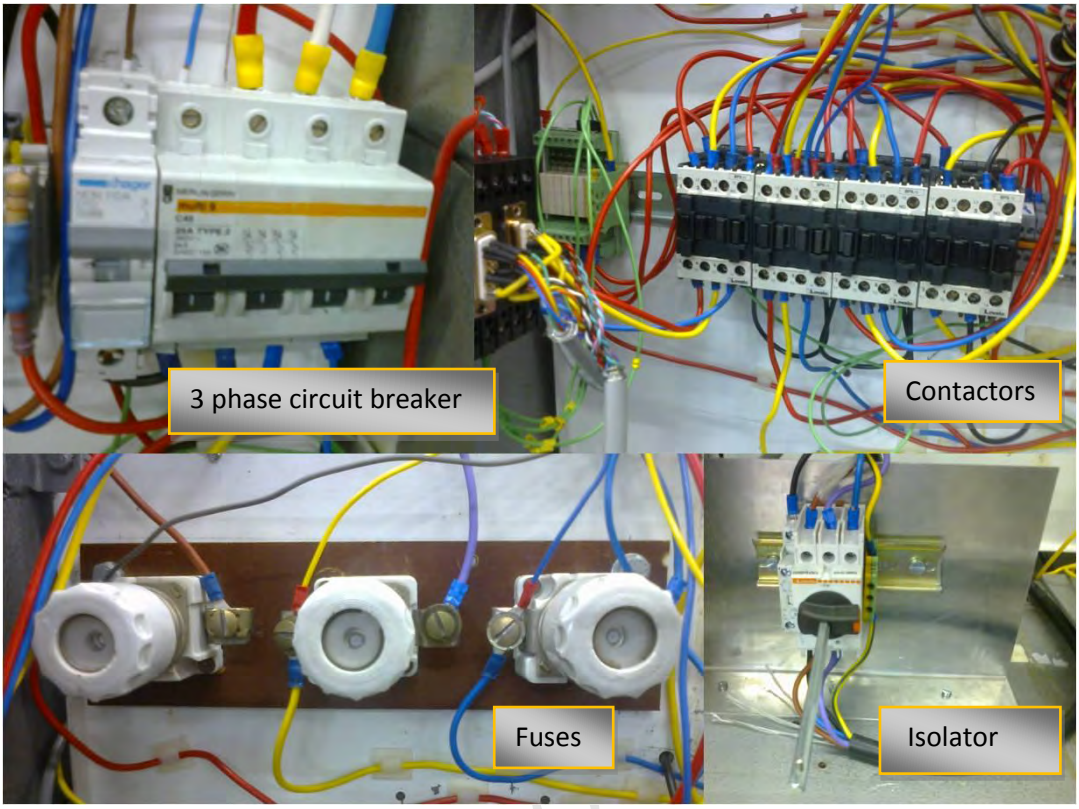

Figure 3.19: System protection showing a circuit breaker, contactors, fuses and an isolator

3.6.9. LCL Filter

The LCL filter is shown in Figure 3.20 below. It comprises two three phase inductors on E core and capacitors. The inductors were specially made to be varied from 1 mH to 3 mH for the inverter side inductor and 2 mH to 6mH for the grid side inductor. The inductors are made to withstand a current capacity of 15 amps.

3.6.10. dSpace Kits

The controller kits in the hardware implementation of this project were ACK Kits1104's from dSpace. Figure 3.21 below shows the dSpace 1104 kits that were used as the interface between the hardware and software of the system. dSpace is able to build models directly from Simulink into Control Desk which is the experimental control

environment. This greatly reduces development time and serves as a great advantage of dSpace.

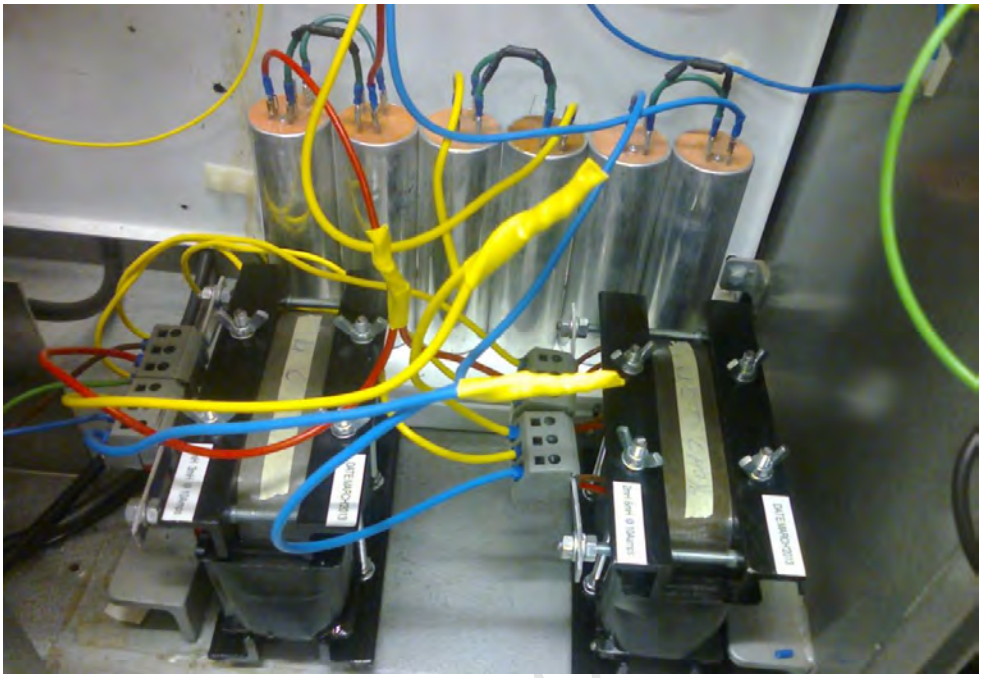

Figure 3.20: LCL Filter

Figure 3.21: dSpace 1104 Kits

3.6.11. Whole Experimental Set –up

The figure below shows a photo taken of the complete experimental set-up and how the different components, that have just been discussed in the preceding sections, are connected. The numbers indicate the different components of the set-up and have been named in the list given below Figure 3.22.

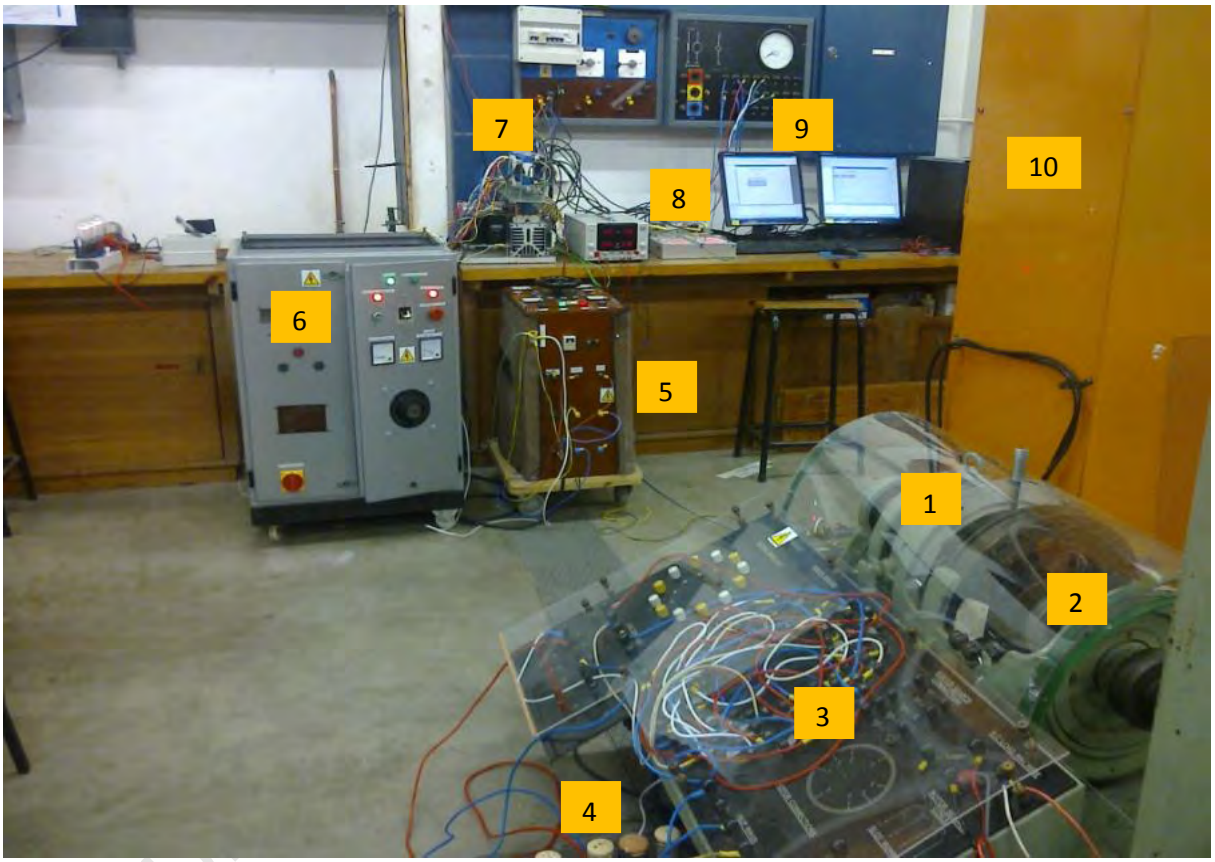

Figure 3.22: Experimental Setup

Components

1. Wound Rotor Induction Machine
2. DC Machine
3. Access to Stator and Rotor windings
4. Current limiting Resistors
5. Three phase variac
6. Panel containing protection components

7. Back to Back Convertor and LEM boards
8. dSpace Kits
9. Desktop PCs
10. DC Machine Drive

4. IMPLEMENTATION IN MATLAB/SIMULINK AND SIMULATION RESULTS OBTAINED

4.1. Introduction

In this chapter the simulation results are discussed. Results were obtained from tests on the machine-side converter and grid-side converter and then from simulating the overall system with both converters connected to the Doubly Fed Induction Generator (DFIG).

All simulations were performed in MATLAB/Simulink and the parameters used for the DFIG are actual parameter values that were obtained from the 'No Load' and 'Locked Rotor' tests on the actual machine. These values are therefore relevant to the experimental set-up as well. For the simulation configuration, a Fixed Step solver was selected with a step size of 0.000237 s. This was used for the experimental implementation as well. The switching frequency was set to 6 kHz in both the simulation and experimental implementations.

The machine-side converter results are presented first, then the grid-side converter results are discussed, and finally simulation results from the overall system are discussed. This is done for balanced and unbalanced grid conditions.

4.2. Simulation of the Machine–Side Converter

The system was simulated when operating at a sub-synchronous speed of 115 rad/sec (1099.5 rpm, 26.7% below synchronous speed). It is then simulated at the synchronous speed of 157 rad/sec (1500 rpm) and finally at a super-synchronous speed of 200 rad/sec (1905 rpm, 27% above the synchronous speed). During the simulation of the systems in the three modes,

4.2.1. Sub-synchronous speed

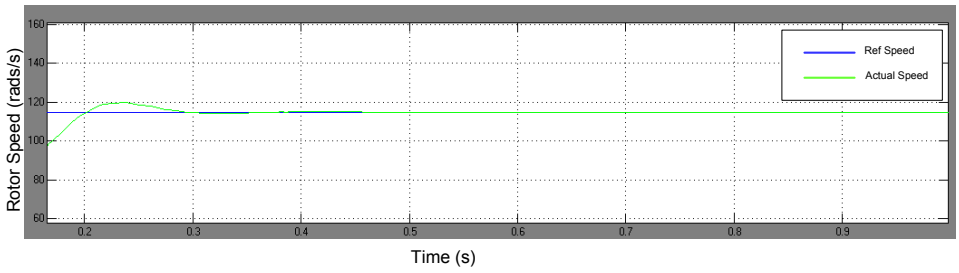

Figure 4.1: Simulated Rotor Speed during Sub-Synchronous speed for machine-side converter

A reference speed of 115 rads/s was fed into the speed control loop and Figure 4.1 above shows that the rotor speed settled and was maintained at the specified speed. Hence this demonstrates the ability of the speed control of the machine to follow the reference signal.

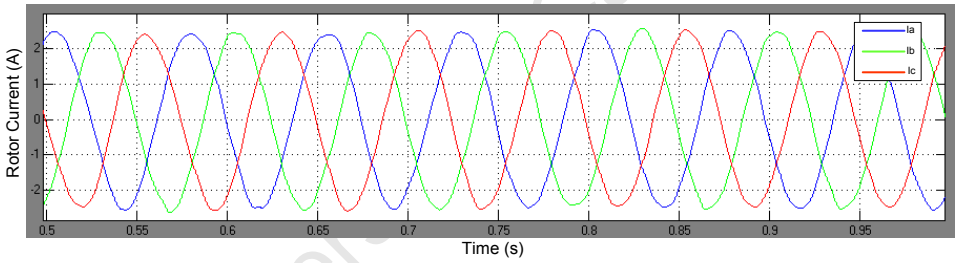

Figure 4.2: Simulated rotor three phase currents during sub-synchronous speed for machine-side converter

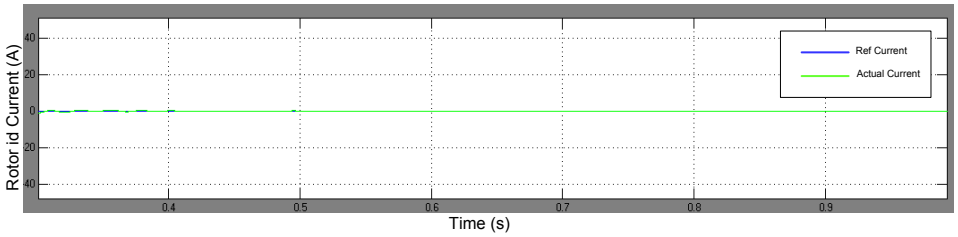

Figure 4.3: Simulated rotor i_d current during sub-synchronous speed for machine-side converter

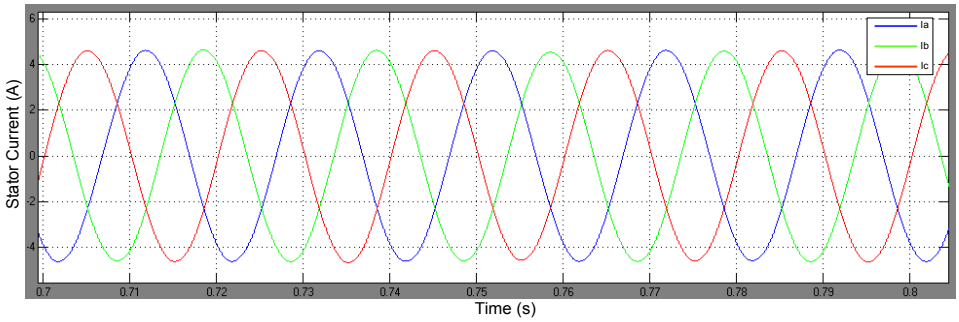

Figure 4.4: Simulated stator three phase currents during sub-synchronous speed for machine-side converter

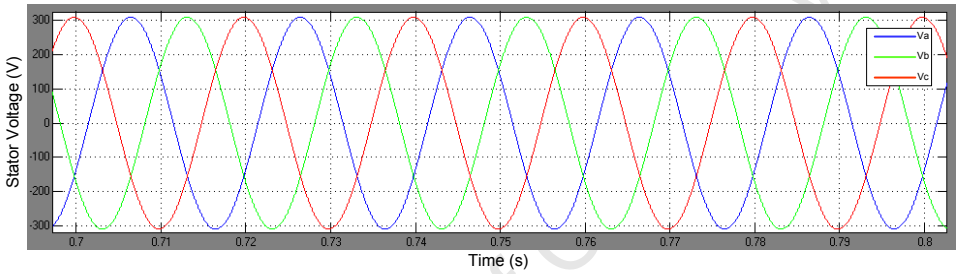

Figure 4.5: Simulated stator three phase voltages during sub-synchronous speed for machine-side converter

Figures 4.2 to 4.5 above are the rotor three phase currents and d component of the current, stator currents and stator voltages respectively. As can be seen from the graphs, the rotor current values are a fraction of the stator current values. It is this inherent characteristic that makes it possible to have a lower rating converter connected to the rotor windings.

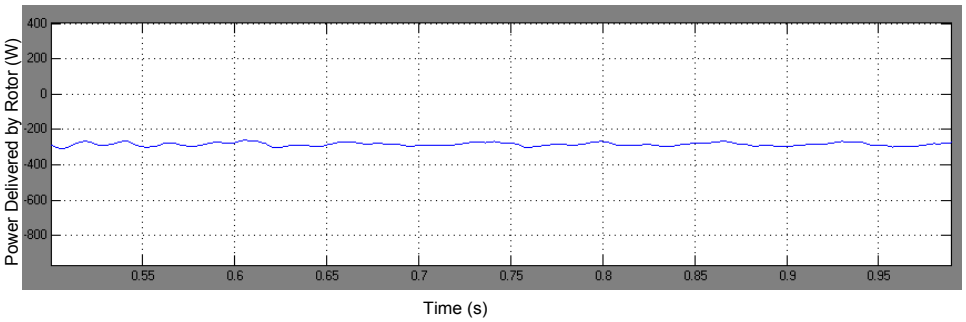

Figure 4.6: Simulated power delivered by the rotor during sub-synchronous speed for machine-side converter

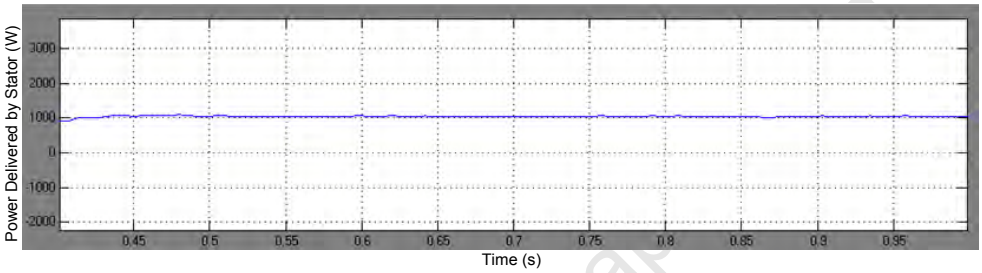

Figure 4.7: Simulated power delivered by the stator during sub-synchronous speed for machine-side converter

The power delivered by the rotor and stator is shown in Figure 4.6 and 4.7 respectively. Equations 4.1 and 4.2 were used to calculate the power on the rotor and stator and the values obtained were compared to the results obtained in the simulations.

$$Stator\ Power\ P_s = Torque\ x\ Speed \qquad 4.1$$

$$Rotor\ Power\ P_r = P_s\ x\ slip \qquad 4.2$$

Using the above equations and the torque value used for the MATLAB/Simulink simulation, which is 7 Nm, the stator power is calculated as follows;

$$Stator\ Power\ P_s = Torque\ x\ Speed = 7\ Nm\ x\ 157\ rads/s = 1099\ W$$

$$Rotor\ Power\ P_r = P_s\ x\ slip = -0.267\ x\ 1099\ W = -293\ W$$

Since the stator variables are rotating at synchronous speed, 157 rads/s is used to calculate the stator power. The results obtained were tabulated as shown below in Table 4.1.

Table 4.1: Calculated and simulated stator and rotor power and the losses

Power Delivered by	Calculated Power (W)	Simulated Power (W)	Power Loss (W)
Stator	1099	1000	99
Rotor	-293	-300	7

4.2.2. Synchronous speed

In this section all results were obtained with the speed maintained at 157 rads/s. Figure 4.8 below illustrates the ability of the system to perform speed control.

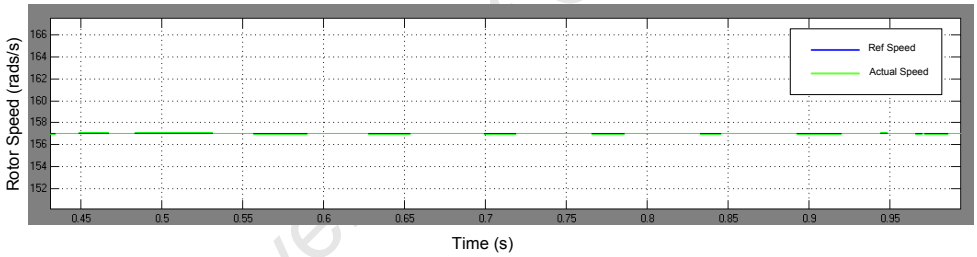

Figure 4.8: Simulated rotor speed during synchronous speed for machine-side converter

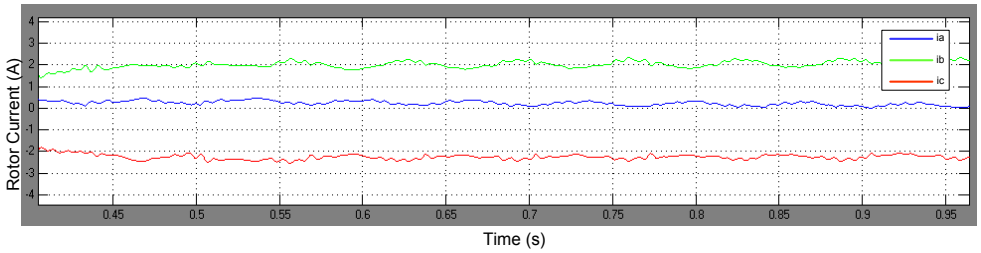

Figure 4.9: Simulated rotor three phase currents during synchronous speed for machine-side converter

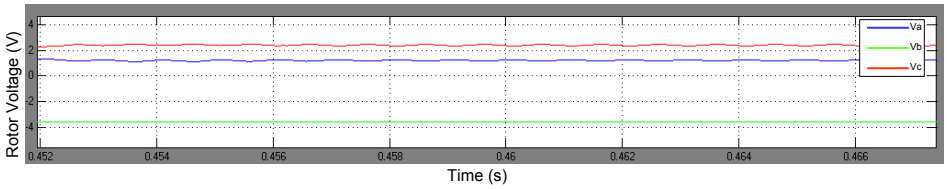

Figure 4.10: Simulated Rotor three phase voltages during synchronous speed for machine side converter

The rotor voltage and current are DC signals because the system was modelled and controlled in the synchronous reference frame and the system is currently operating at synchronous speed; that is, there a no slip hence no slip frequency. This lines up with the theory and fundamentals in Chapter 2.

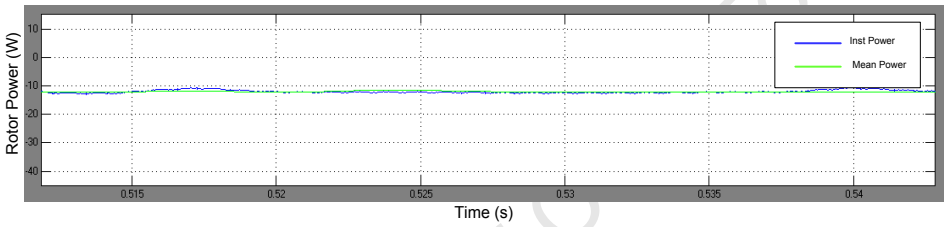

Figure 4.11: Simulated power delivered by the rotor during synchronous speed for machine-side converter

At synchronous speed the power being delivered by the rotor should be zero. Figure 4.11 shows a power of 13 W which is due to losses in the converter as it is not possible to have zero power loss.

4.2.3. Super-synchronous speed

Figure 4.12 below shows the rotor speed being set to 200 rads/s (1905 rpm). Both the reference speed and actual speed are shown. This super-synchronous speed is maintained by the control and the three phase stator voltages and currents, the rotor current, the power delivered by the stator and the rotor power are measured, recorded and shown in Figures 4.13 to 4.17.

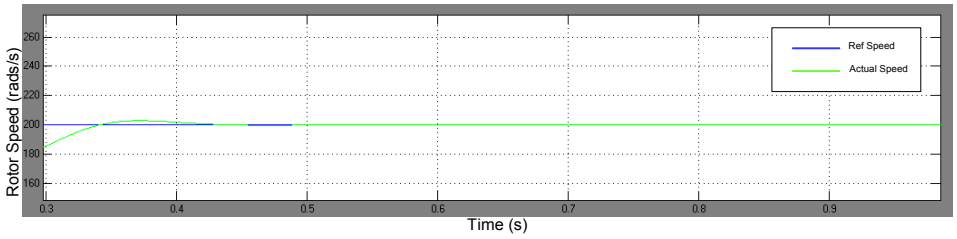

Figure 4.12: Simulated rotor speed during super-synchronous speed for machine side converter

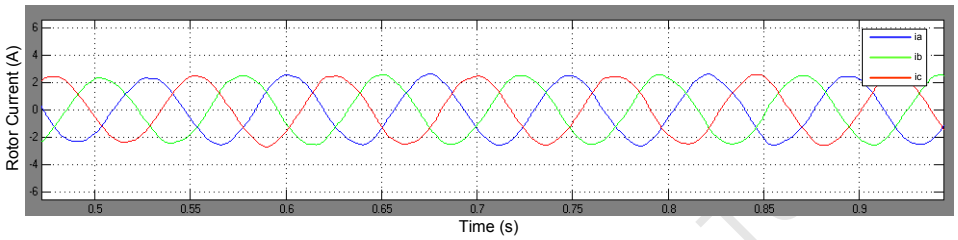

Figure 4.13: Simulated rotor three phase currents during super-synchronous speed for machine-side converter

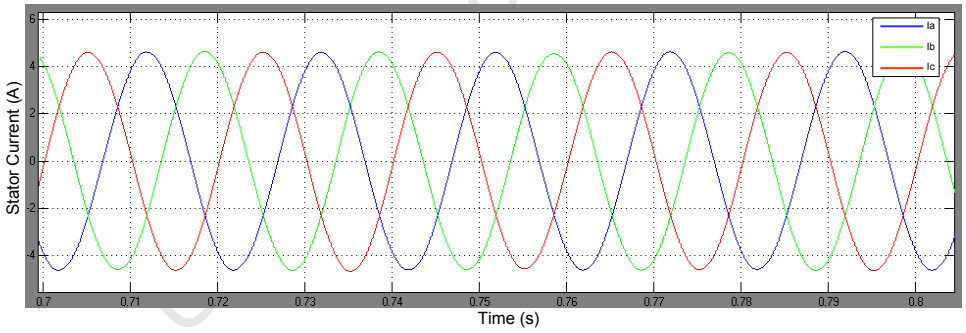

Figure 4.14: Simulated stator three phase currents during super-synchronous speed for machine-side converter

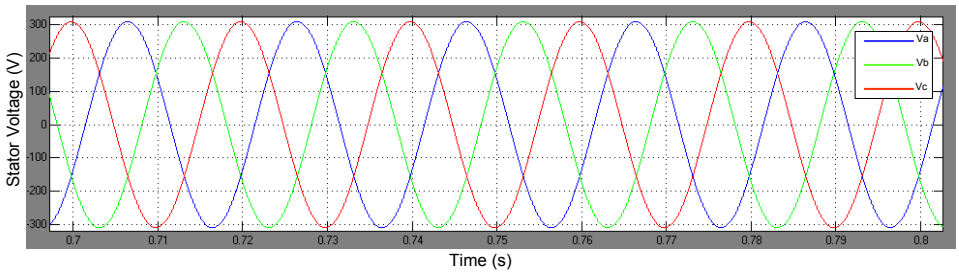

Figure 4.15: Simulated stator three phase voltages during super-synchronous speed for machine-side converter

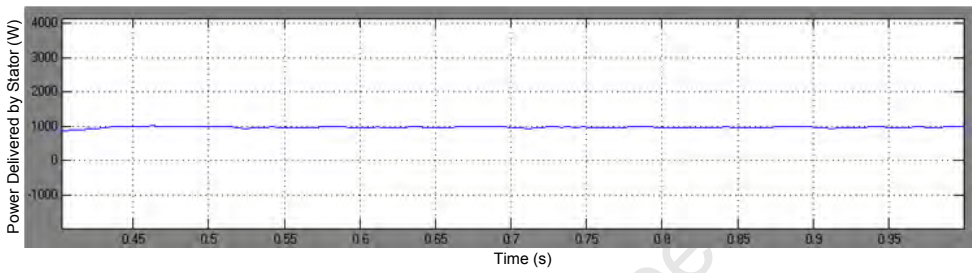

Figure 4.16: Simulated power delivered by the stator during super-synchronous speed for machine-side converter

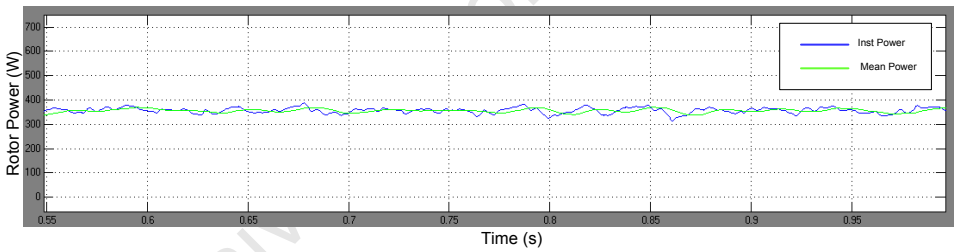

Figure 4.17: Simulated power delivered by the rotor during super-synchronous speed for machine-side converter

The power delivered by the rotor is shown in Figure 4.17. The power delivered by the stator is the same as that from Figure 4.7. Equations (4.1) and (4.2) were again used to calculate the power on the rotor and stator and the values obtained were compared to the results obtained in the simulations.

$$Stator\ Power\ P_s = Torque\ x\ Speed$$

$$Rotor\ Power\ P_r = P_s\ x\ slip$$

Similar to the calculations in section 4.2.1, the above equations are used to calculate the stator and rotor power as follows;

$$Stator\ Power\ P_s = Torque\ x\ Speed = \ 7\ Nm\ x\ 157\ rads/s = 1099\ W$$

$$Rotor\ Power\ P_r = \ P_s\ x\ slip = \ 0.27\ x\ 1099\ W = \ 340.2\ W$$

The results obtained were tabulated as shown below in Table 4.2;

Table 4.2: Calculated and simulated stator and rotor power and the losses

Power Delivered by	Calculated Power (W)	Simulated Power (W)	Power Loss (W)
Stator	1099	1000	99
Rotor	340.2	340	0.2

4.3. Grid – Side Converter

The grid-side converter is now looked at in this section. The main purpose of the grid-side converter control is to maintain the DC Link voltage at a value set by the reference signal as well as to transfer power to and from the grid.

On the grid-side converter as on the machine-side converter, there is independent control of the direct and quadrature axis current components. On the machine-side converter, the direct current component is maintained at 0 A in balanced grid conditions. While on the grid-side converter, it is the quadrature axis current component that is kept at 0 A during balanced grid conditions. The quadrature axis current component is responsible for reactive power.

The control comprises of an outer voltage control loop which maintains the DC Link voltage, and two inner current control loops which control the direct and quadrature axis current components.

4.3.2. DC Link Voltage control

Figures 4.18 and 4.19 below demonstrate the converters ability for voltage control.

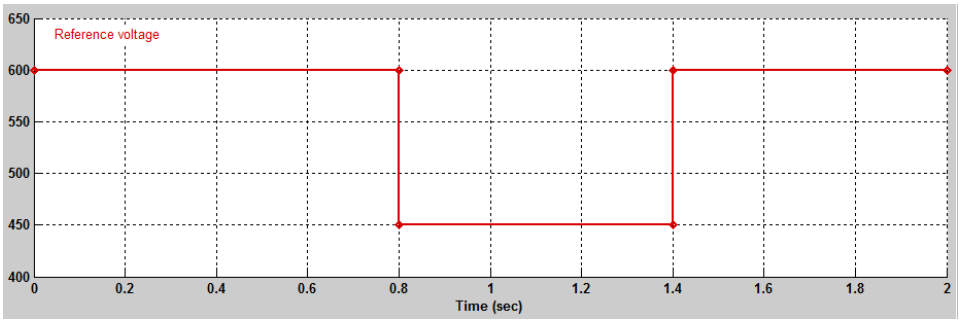

Figure 4.18: Simulated signal builder used to step DC Link voltage from 600V to 450V to 600V for grid-side converter

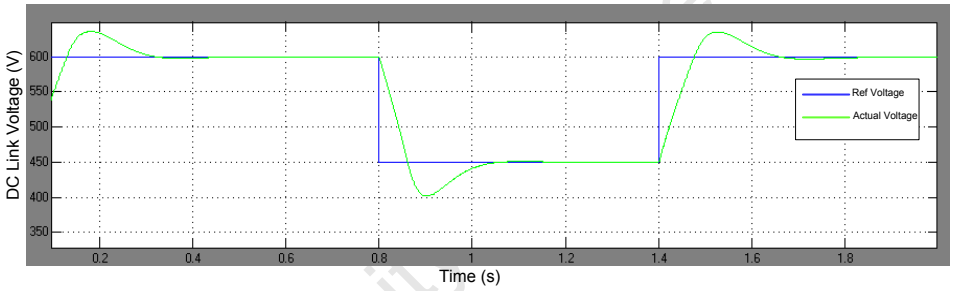

Figure 4.19: Simulated DC Link voltage for a step in Voltage from 600 V to 450 V to 600 V for grid-side converter

Reactive power capability

This section shows the reactive power capability of the converter by showing the leading and lagging power factor. The leading and lagging of the power factor is evident in the way the supply phase currents lead and lag the phase voltages when the quadrature axis current was maintained at 3 A and -3 A. The DC Link voltage was maintained at 600V for all the cases in this section.

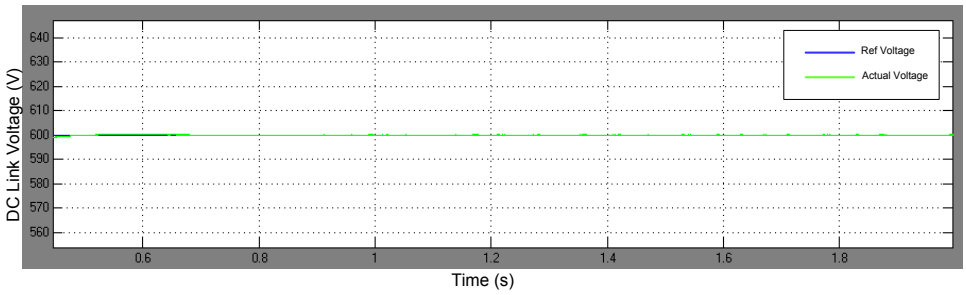

Figure 4.20: Simulated DC Link voltage maintained at 600 V for grid-side converter

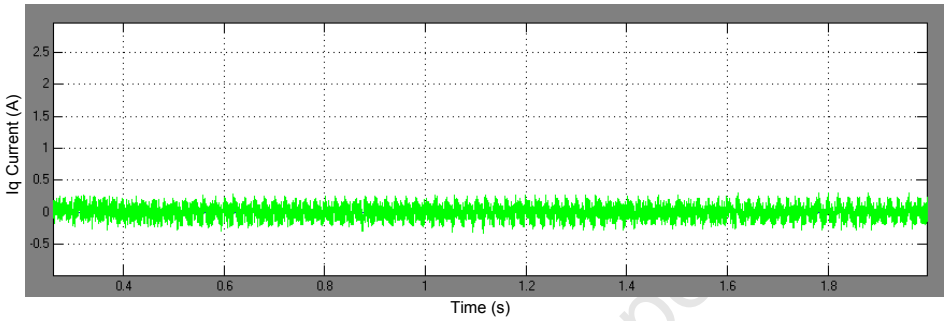

Figure 4.21: Simulated quadrature axis current component iq maintained at 0 A for grid-side converter

Here, i_q was maintained at 0Amps as shown in Figure 4.21. Figures 4.22 and 4.23 below demonstrate the operation of the converter in inverting mode which corresponds to super synchronous operation, that is, current flowing into the grid. From the figures it can be seen that the phase currents and voltages are 180° out of phase which validates that the operation is in inverting mode. Since iq was maintained at 0A, there was no reactive power through the converter.

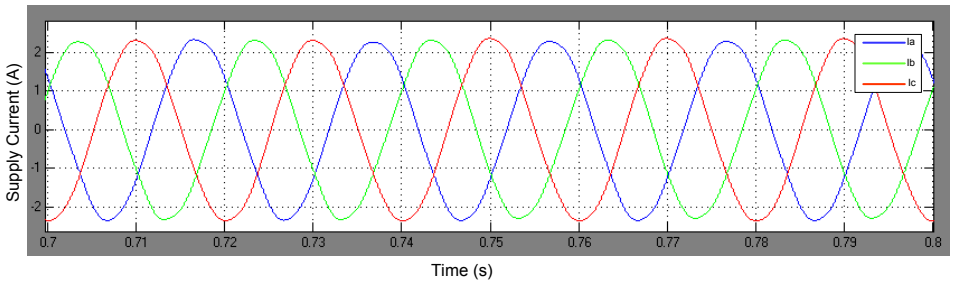

Figure 4.22: Simulated supply currents when i_q = 0 A during inverting mode for grid-side converter

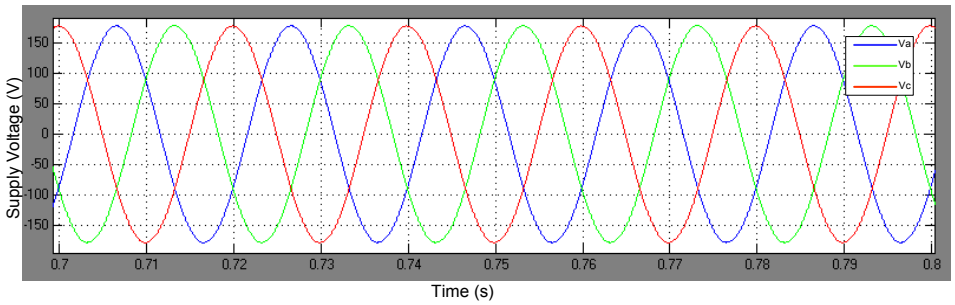

Figure 4.23: Simulated supply voltages when i_q = 0 A during inverting mode for grid-side converter

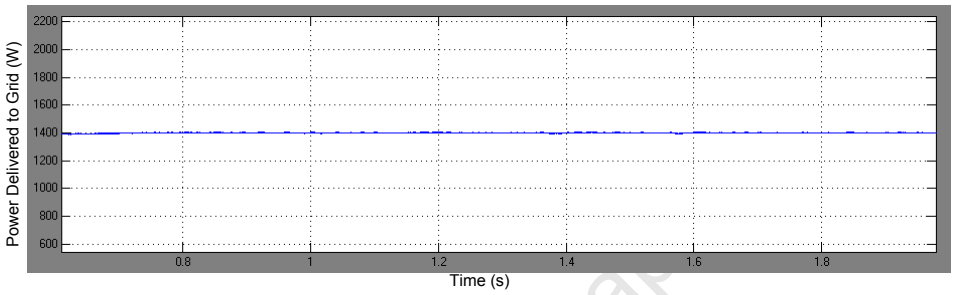

Figure 4.24: Simulated total power transferred to the grid

The quadrature axis current was now regulated at -3 A as is shown in Figure 4.25 below. Figure 4.26 and 4.27 show the supply phase currents and voltages. The current is leading the voltage.

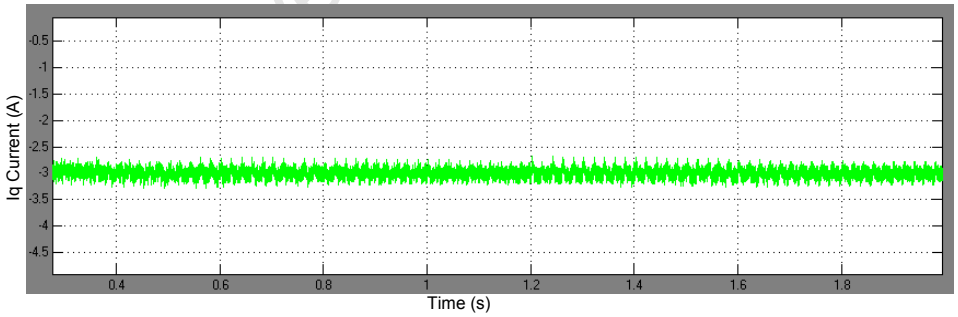

Figure 4.25: Simulated quadrature axis current i_q maintained at -3 A for grid-side converter in inverting mode

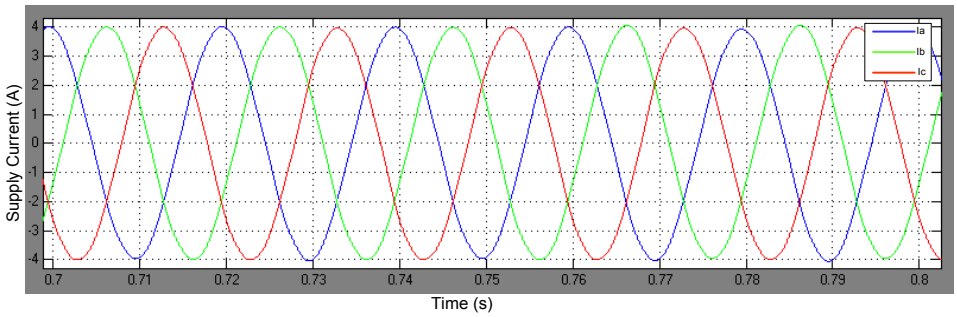

Figure 4.26: Simulated supply currents when i_q = -3 A for grid-side converter in inverting mode

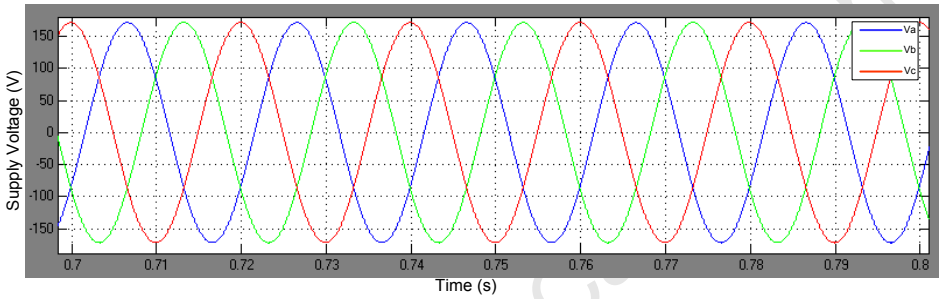

Figure 4.27: Simulated supply voltages when i_q = -3 A for grid-side converter in inverting mode

Figure 4.28 below shows that the quadrature axis current component being maintained at 3 A. Figures 4.29 and 4.30 show the supply phase currents and voltages. The current is lagging the voltage.

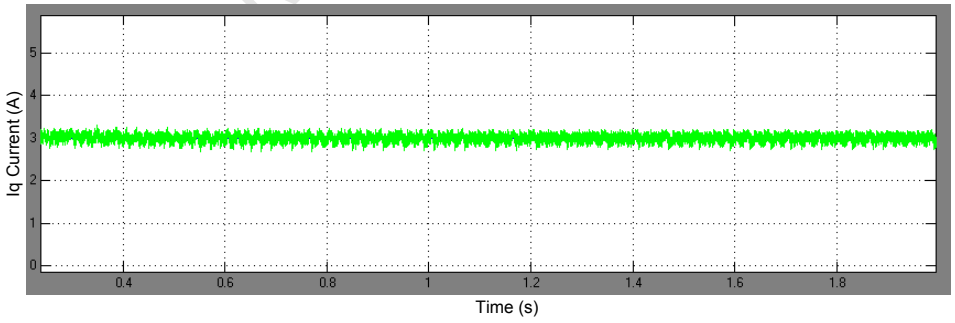

Figure 4.28: Simulated quadrature axis current i_q maintained at 3 A for grid-side converter in inverting mode

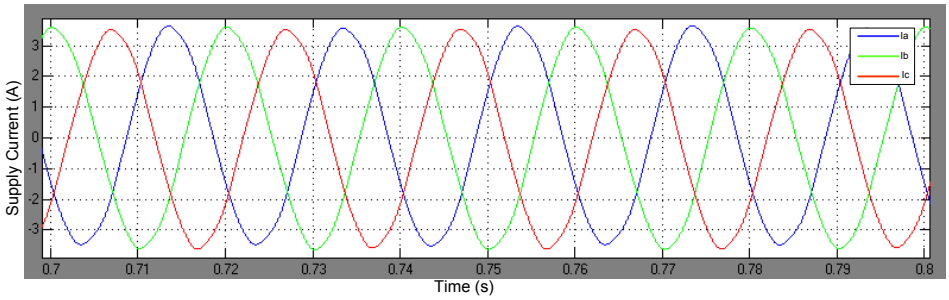

Figure 4.29: Simulated supply currents when iq = 3 for grid-side converter in inverting mode

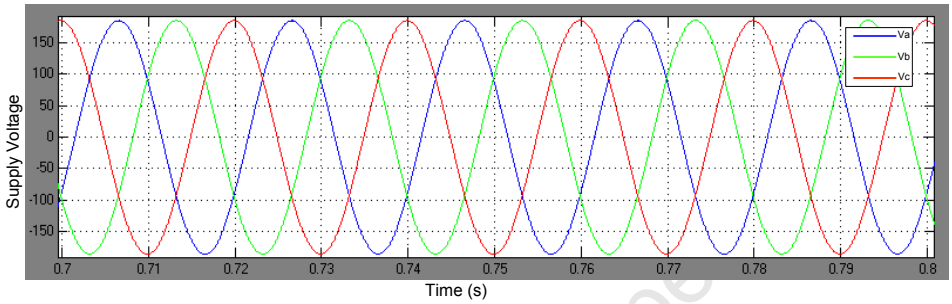

Figure 4.30: Simulated supply voltages when i_q = 3 for grid-side converter in inverting mode

Independent control of direct and quadrature axis current components

This section demonstrates how the quadrature axis current control is independent of the direct current control. In Figures 4.32 the quadrature axis current component is stepped up to 1 A using the signal builder in Figure 4.31. It is clear from Figure 4.32 that the direct axis component is not affect by the step in the quadrature axis current component.

The same can be seen in Figure 4.34 when the quadrature axis current component is stepped down to -1 A using the signal builder in Figure 4.33. Again the direct axis component is not affected by this change in the quadrature axis current component.

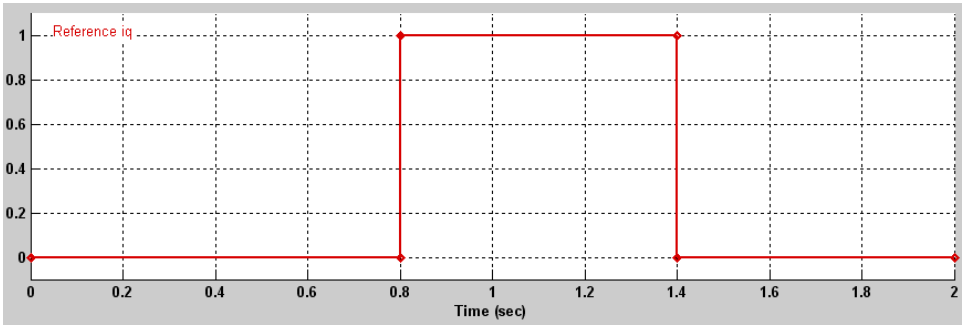

Figure 4.31: Simulated signal builder used to step the quadrature axis current component from 0 A to 1 A to 0 A for grid-side converter

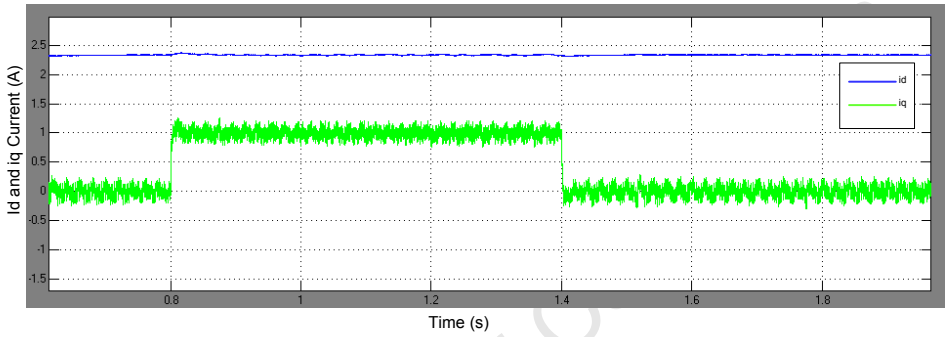

Figure 4.32: Simulated quadrature axis current i_q response to step for grid-side converter

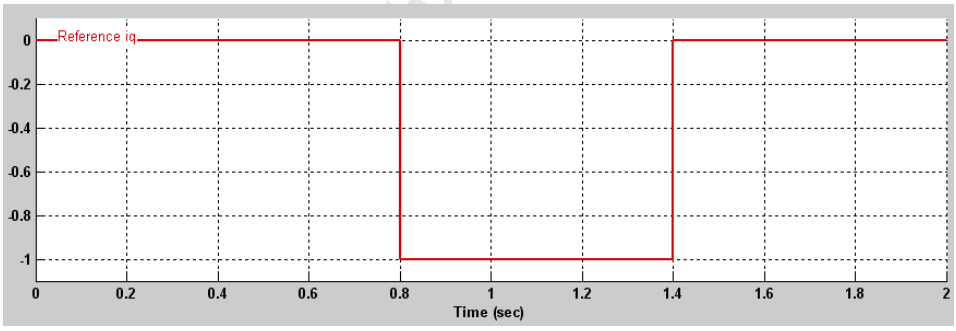

Figure 4.33: Simulated signal builder used to step the quadrature axis current component from 0A to -1 A to 0 A for grid-side converter

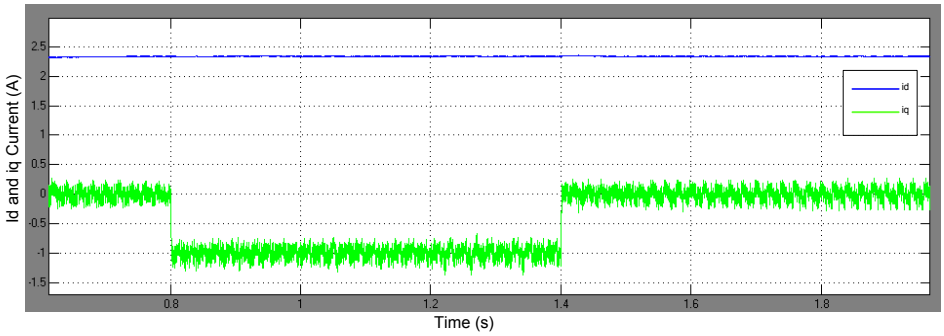

Figure 4.34: Simulated quadrature axis current i_q response to step for grid-side converter

4.4. Control of Overall System

The results obtained from the simulation of the overall system are shown here. This is first done with balanced grid, and then with unbalanced grid. The set of results shown for the balanced grid below not only verifies that the whole system is operational when connected together, but it also demonstrates the transient response of the system and the ability of the control to remain stable in this state.

4.4.1. With Balanced Grid

In order to verify the ability of the system control to operate as expected when the overall system is connected and tested in its entirety, the speed is stepped up from 115 rads/d (sub-synchronous speed) to 180 rads/s (super-synchronous speed) and the results obtained are laid out below.

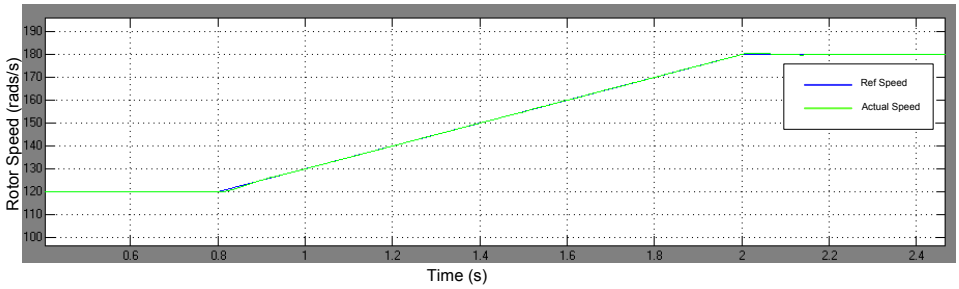

Figure 4.35: Simulated rotor speed from sub-synchronous to super-synchronous speed on overall system

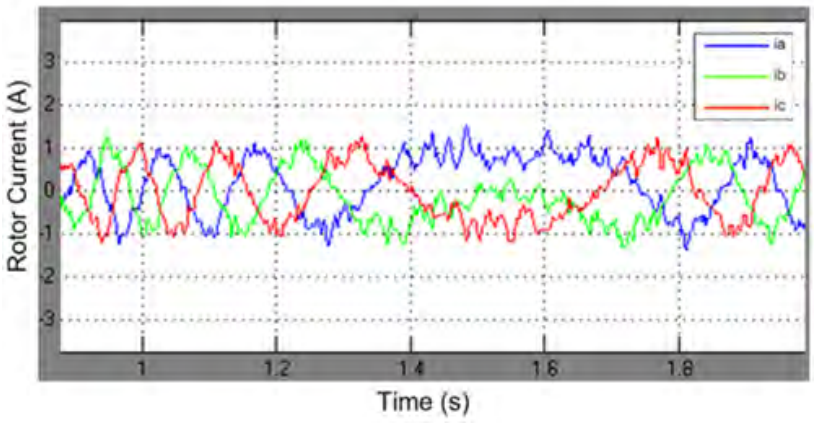

Figure 4.36: Simulated rotor current during sub-synchronous to super-synchronous speed on overall system

It is interesting to note above in Figures 4.38 and 4.39 that the frequency of the rotor reduces to zero at synchronous speed, as is verified by the signal being momentarily DC, and the rotor frequency begins to increase again as is seen by the sinusoidal currents. This is because as the speed varies from sub-synchronous speed to super-synchronous speed, the slip also varies from positive to negative. The point at with the slip crosses the zero point as the point at which the frequency of the rotor equals zero since $f_r = sf_s$. Where f_s is the stator frequency, s it the slip and f_r is the rotor frequency.

The power delivered by the rotor is also determined by the slip. Hence, as can be seen in Figure 4.37 below, as the slip varies the power also varies and it is zero when the slip crosses the zero point.

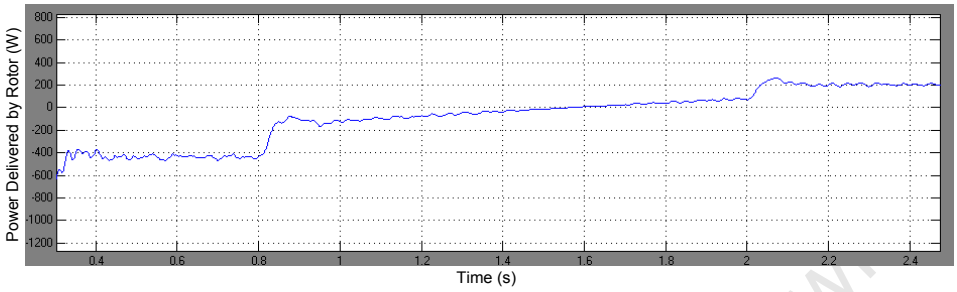

Figure 4.37: Simulated power delivered by the rotor during sub-synchronous to super-synchronous speed on overall system

4.4.2. With 50% 3-phase Voltage-dip

The results obtained in this section are the system's response to a 50% 3-phase voltage dip introduced at 0.4s. It can be seen in Figure 4.38 below, that the stator three phase voltage drops to half its original value.

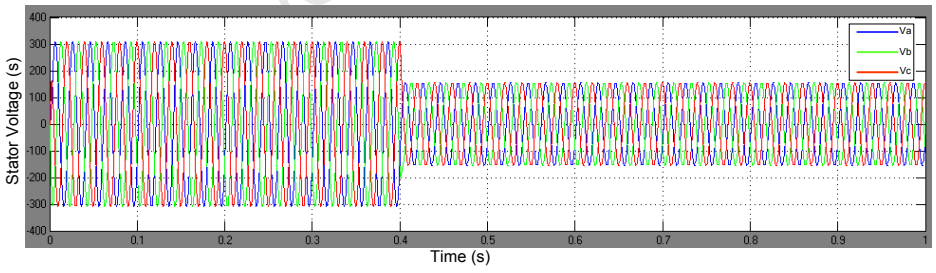

Figure 4.38: Simulated stator phase voltages with a 50% 3-phase voltage-dip introduced at 0.4s

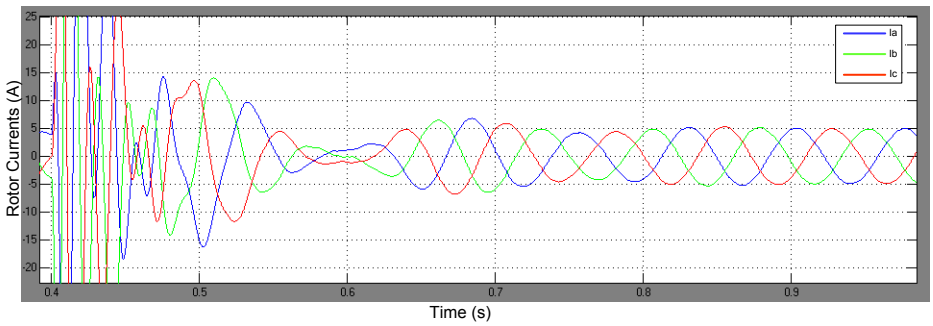

Figure 4.39: Simulated rotor phase currents with a 50 % 3-phase voltage-dip introduced at 0.4s

Figure4.39 above demonstrates the Fault Ride Through (FRT) capability of the Doubly Fed Induction Generator. This can be seen by the three phase currents stabilising with the voltage dip still present in the system. Further, there is an increase in the current being fed to the grid, due to reactive current compensation, as would be expected. The increase in current during the voltage dip can be also be confirm by the work done in [23].

The DC Link voltage in Figure 4.40 below continues to be regulated despite the 3-phase dip. Again this is a verification of the FRT capability of the system.

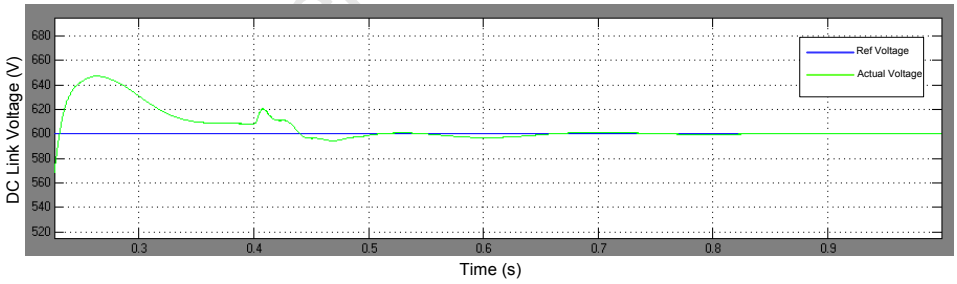

Figure 4.40: Simulated DC Link voltage with a 50 % 3-phase voltage-dip introduced into the system

4.4.3. With 30 % 3-phase over-voltage

A 3-phase over-voltage is now introduced into the system as can be seen by the increase in the stator three phase voltage in Figure 4.41 below.

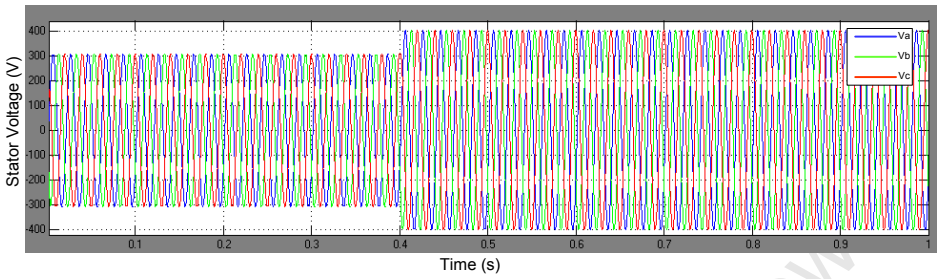

Figure 4.41: Simulated stator phase voltages with a 30 % 3-phase over-voltage introduced into the system

Figures 4.42 – 4.43 below show the system response the over-voltage. Again the FRT capability is evident by the stable rotor three phase currents and the DC Link voltage which is maintained at 600 V. Further there is a decrease in the current which also agrees with the work done in [23].

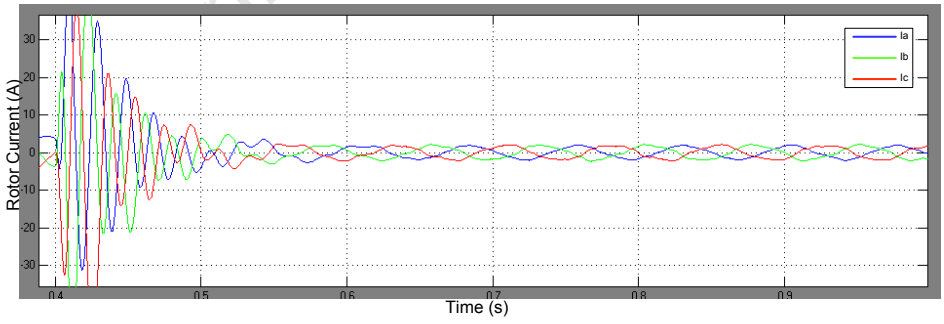

Figure 4.42: Simulated rotor phase currents with a 30 % 3-phase over-voltage introduced into the system

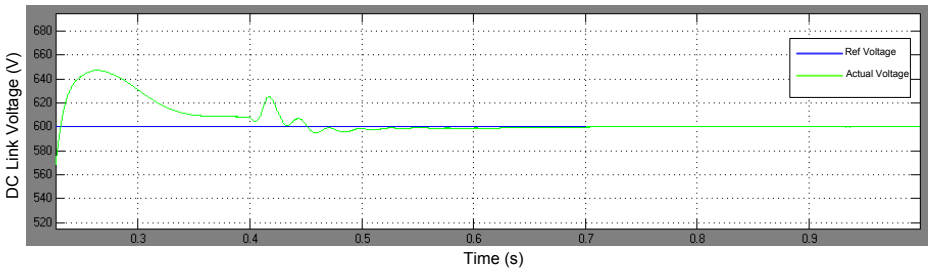

Figure 4.43: Simulated DC Link voltage with a 30 % 3-phase over-voltage introduced into the system.

4.5. Conclusion

The above results demonstrate that the model simulated in Matlab Simulink operated as expected and was able to provide ancillary services such as reactive power capability and fault ride through. This fulfils the requirements of the new grid codes that ask that wind energy systems should be able to actively participate and contribute to supporting the network [16 31].

Though the dips and over voltages used for the simulation may have been quite exaggerated, the simulated model has shown that it is able to perform Fault ride through which is another requirement according to the rising grid codes that the wind turbines stay connected to the grid for steady state voltage unbalances of up to 2 % [32].

5. EXPERIMENTAL IMPLEMENTATION AND VALIDATION

5.1. Introduction

The experimental model is validated in this chapter. The layout of the results will be similar to that of the simulation results in Chapter 4. This is done for ease of comparison and discussion. As was mentioned in Chapter 4, for the experimental implementation a Fixed Step solver is selected, also with a step size of 0.000237 s and a switching frequency of 6 kHz. The MATLAB/Simulink models are converted into the real time simulation control desk. This is the real time interface package and converts the Simulink models into the equivalent C-code. Hence the DFIG model that was used in MATLAB/Simulink is now replaced by actual voltages and currents measured from the machine and read in through the ADC's on the dSpace Kit via the LEM modules. All other calculations and transformations remain the same as in the purely simulated environment.

The machine–side converter control is discussed together with its operating results. The grid–side converter control and operating results are discussed afterward. These two sub-systems are tested independently as in Chapter 4. After it has been shown that the sub-systems are operational, the overall system is then tested in order to verify its operation.

The machine–side converter control is validated by performing a series of tests to verify speed control, operation in rectifying and inverting mode. Furthermore, details of the slip angle calculation are shown. Correct angle calculation is vital for correct operation and stability of control in inverting and rectifying mode, as well as the changeover between the two modes of operation.

5.2. Machine – Side Converter Control

The machine-side converter is discussed in this section. The start-up, rotor angle calculation procedures and speed control are first discussed. Operation of the DFIG is then evaluated in the following modes; sub-synchronous, synchronous, super-synchronous. In all these modes, a stable DC link voltage of 300 V is maintained by grid-side converter. The machine-side and grid-side converters' operation are electrically separated by the DC link and are independent of one another. Therefore, the operation of the one has no effect on the results of the other.

5.2.1. Start-up, rotor angle calculation procedures and speed control

A soft start is needed in order to avoid high inrush currents in the rotor windings. There are two common methods of starting up. Method (1) involves connecting resistors to the rotor windings at start up, and Method (2) involves synchronisation of the stator to the grid in the following steps [33] and [34];

- DC Bus is Charged up
- DC bus voltage is used to accelerate the rotor windings
- Machine-Side converter control is initialised
- DC bus voltage value is regulated at set point
- Rotor shaft speed is maintained at synchronous speed
- Stator is synchronized by switching it to the grid

In order for Method 2 to be implemented, the grid voltage value and the voltage value at the capacitors of the filter need to have the same amplitude, frequency and phase angle, with very little deviation in these named parameters [33].

The method used in this project is method 1, connecting resistors to the rotor to limit current at start-up. A schematic of the setup for operation in this sub-system is shown in Figure 5.1 and a photo of the setup is shown in Figure 5.2 below.

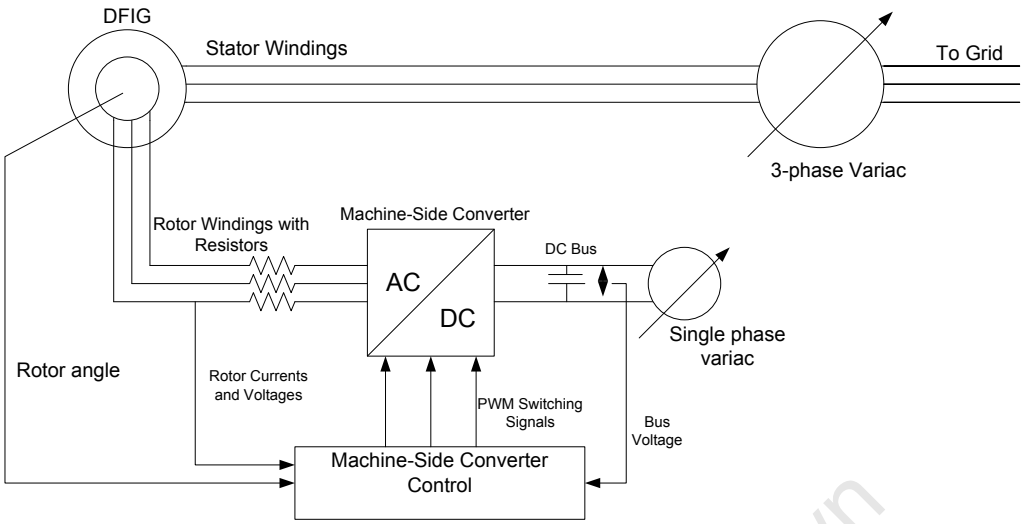

Figure 5.1: DFIG with resistors connected to the rotor windings to limit current

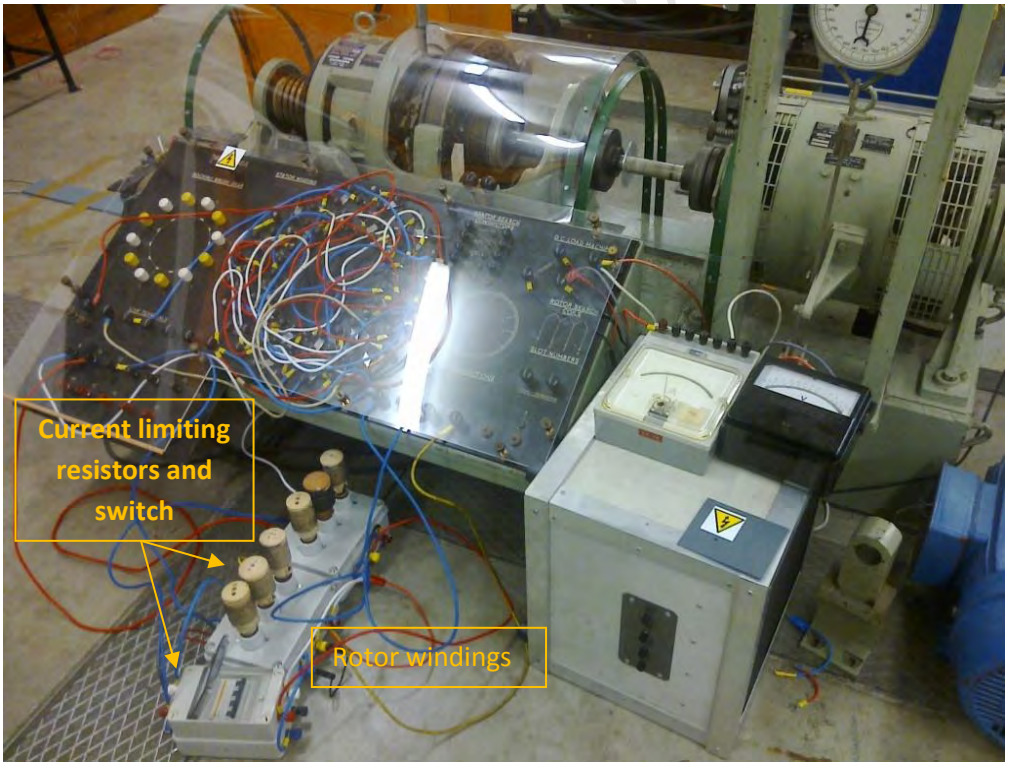

Figure 5.2: DFIG with resistors connected to the rotor windings to limit current

Rotor Slip angle calculation

In order to get the fundamental angle that is used in transformations for the calculation of PWM generation signals, the rotor angle, theta m, is obtained from the encoder and stator angle, theta s, is obtained by using a PLL. The difference of the two signals produces the fundamental angle.

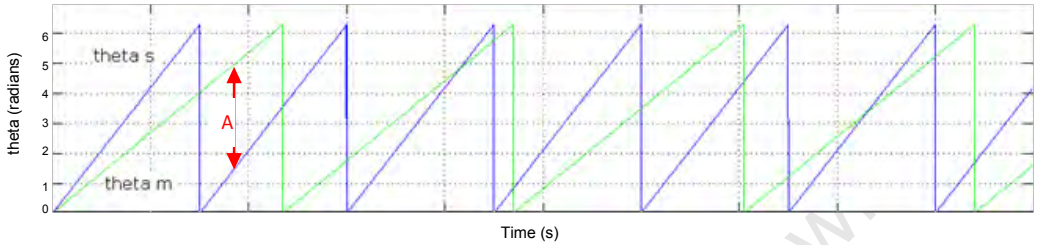

Figure 5.3: Stator angle theta s and rotor angle theta m

A problem could arise in obtaining the difference of the two angles when theta s is less than theta m as shown by section A in Figure 5.3 above. In section A above, the numeric value obtain by subtracting theta m from theta s is negative, leading to the incorrect theta r waveform and which could destabilise the control.

Hence a mathematical equation was formulated and modelled in Matlab Simulink as shown below;

If theta s > theta m, theta r = theta s – theta m

*Else theta r = (theta s + 2*π) – theta m.*

By adding 2*π to theta s before subtracting theta m from it, we ensure that we get a positive value. The 2*π effectively shifts the theta s waveform above the theta m waveform by the same value it was below the theta m waveform.

The above principle was then formulated in MATLAB/Simulink and the model obtained is shown in Figure 5.4 below.

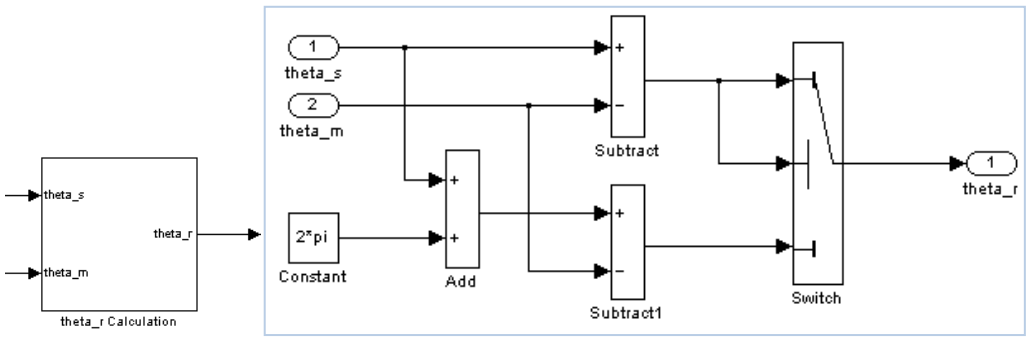

(a) (b)

Figure 5.4: theta r calculation (a) theta r calculation subsystem, (b) theta r calculation details

This is to ensure that a correct and positive value for theta r is obtained. The model was implemented experimentally in control desk and the results are shown in Figure 5.5. It was also verified in Figure 5.6 that the angle is calculated correctly in both sub-synchronous and super-synchronous operation of the rotor.

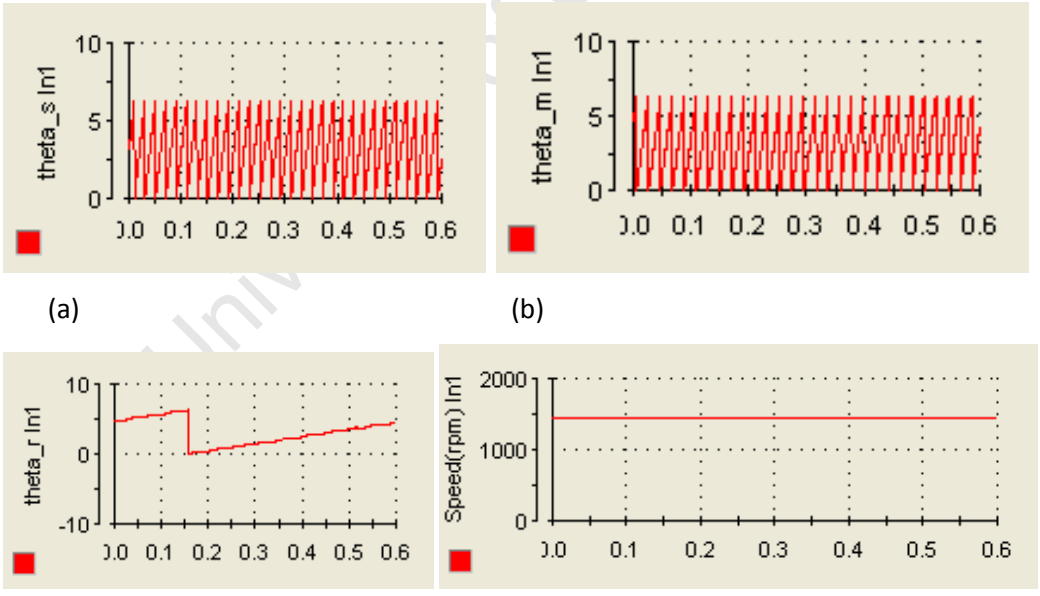

(a) (b)

(c) (d)

Figure 5.5 (a) Stator angle theta s, (b) rotor angle theta m, (c) slip angle theta m, (d) Rotor speed

The theta s waveform is shown in Figure 5.5 (a) above and the theta m waveform is shown in Figure 5.5 (b), both are in rads/s. The two waveforms are captured with the rotor speed just below synchronous speed as shown in Figure 5.5 (d). Theta r, which is the difference between the theta s and theta m is shown in Figure 5.5 (c). It is evident that this waveform is at a much lower frequency and this is because as the rotor speed approaches synchronous speed, the slip frequency tends to zero and at synchronous speed the theta r waveform is a dc value equal to 2*π.

Figure 5.6 (a) and (b) below show the rotor speed and rotor slip angle (theta r) respectively as the rotor speed is stepped slightly from super-synchronous speed to synchronous speed.

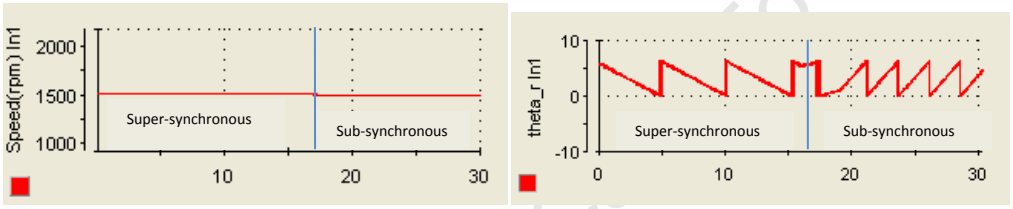

(a) (b)

Figure 5.6: Rotor angle calculation in super and sub-synchronous speeds. (a) Rotor speed, (b) Rotor slip angle

Speed control

The response of the doubly fed induction generator to a step change in speed was evaluated. The speed of the rotor was stepped up from 1400rpm to 1440rpm and the response is shown in Figure 5.7 below. The performance of the machine–side converter control was also evaluated for a step reduction in speed of the rotor from 1000 rpm to 950 rpm. The results are shown in Figure 5.8 below. In both tests the control is stable as demonstrated by the speed settling at the reference speed value. Furthermore, this verifies the machine–side converter's speed control ability within a fixed speed range determined by the slip, usually +/- 20 – 30 % [35] +/- 30 % is an optimal range to take advantage of lower cost of converter as higher ratings will mean higher cost of the converter [35]. The back to back convertor used in this project had a higher power rating since it was readily available; hence, as shown in Figure 5.7 the

speed control ability was at a high slip of 36.7 %. In general however, converter ratings used in DFIGs are limited to about 38 % of the stator power, which therefore limits the operating slip range to the afore-mentioned range [37].

In the following sections, operation in sub-synchronous and super-synchronous speed were operated within the +/- 30 % slip range.

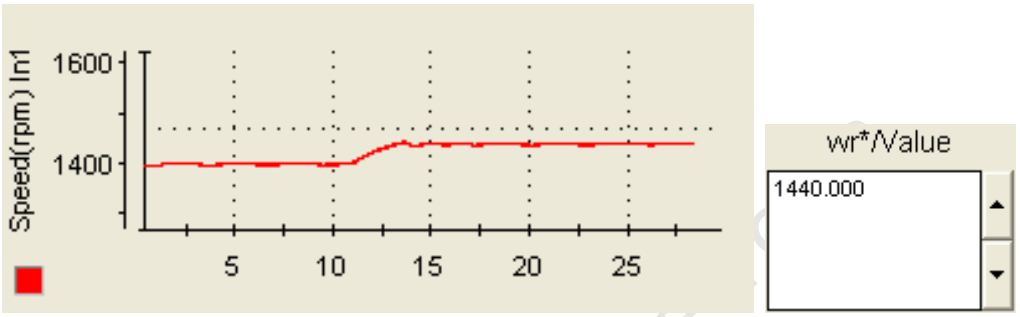

Figure 5.7: Speed response to step change in speed from 1400rpm to 1440rpm

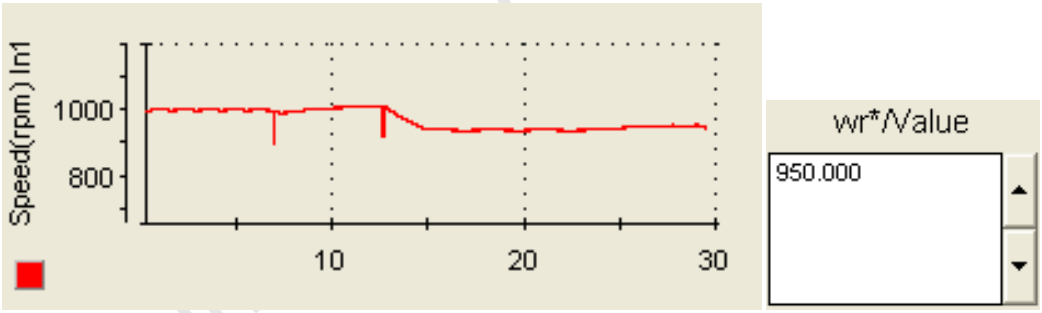

Figure 5.8: Speed response to step change in speed from 1000rpm to 950rpm

5.2.2. Sub-synchronous speed operation

The operation of the machine–side converter in sub-system mode will now be evaluated in sub-synchronous, synchronous and super–synchronous speeds. The results recorded are the DC link voltage, rotor speed, rotor and stator three phase currents and voltages as well as the stator d and q voltage components. The DC link

voltage was maintained at the 300V due to physical constraint of the Variac used. This is shown in Figure 5.9 below.

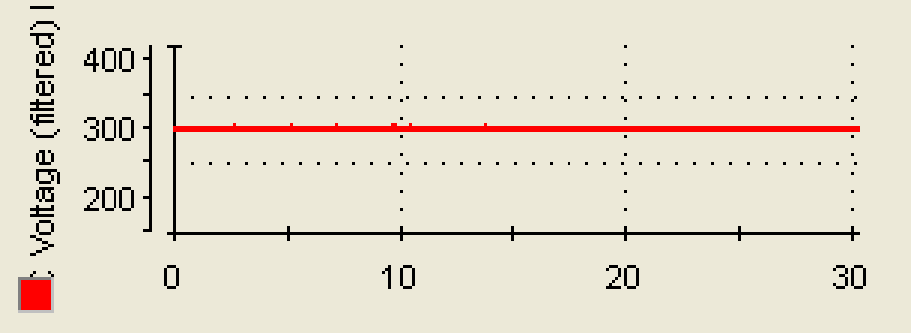

Figure 5.9: DC Link Voltage maintained at 300V

In Figure 5.10 below, the rotor speed was maintained at 1110 rpm which represents a slip of 26 %. This was done to match the speed in the Simulink implementation which was maintained at a slip of 26.7 % in sub-synchronous operation.

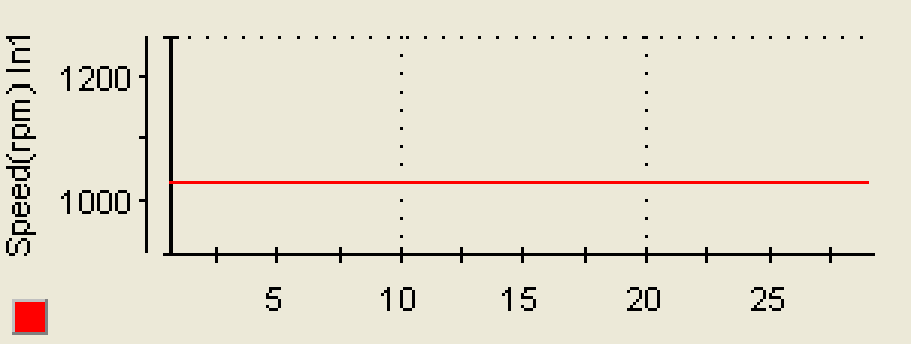

Figure 5.10: Rotor speed in sub-synchronous operation maintained at 1110rpm (26% slip)

The rotor three phase currents and the stator three phase voltages are in phase during sub-synchronous speed. This verifies that both are being supplied externally and not supplying power to the grid [20]. The stator windings are supplied by the grid while the rotor windings are supplied by the DC Bus through the DC-

AC inverter. The frequency of the stator voltages are at the supply frequency of 50 Hz, whilst the rotor currents are at a frequency of s.f = 50 Hz x 0.26 = 13 Hz.

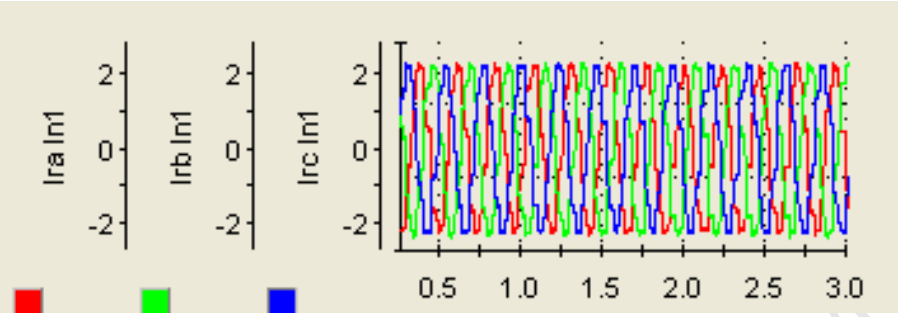

Figure 5.11: Rotor phase currents during inverting mode at 1110rpm (26% slip)

For ease of control, the above phase currents are transformed into the direct and quadrature axis components using the equations below;

$$i_\alpha = \frac{2}{3}\left(i_a - \frac{i_b}{2} - \frac{i_c}{2}\right) = \frac{2}{3}i_a - \frac{i_b}{3} - \frac{i_c}{3} \quad (5.1)$$

$$i_\beta = \frac{2}{3}\left(\frac{i_b\sqrt{3}}{2} - \frac{i_c\sqrt{3}}{2}\right) = \frac{i_b}{\sqrt{3}} - \frac{i_c}{\sqrt{3}} \quad (5.2)$$

$$i_d = i_\alpha cos\theta_r + i_\beta sin\theta_r \quad (5.3)$$

$$i_q = -i_\alpha sin\theta_r + i_\beta cos\theta_r \quad (5.4)$$

The fundamental angle (θ_r) used in these transformations is theta r obtained by the calculation shown in Figure 5.4.

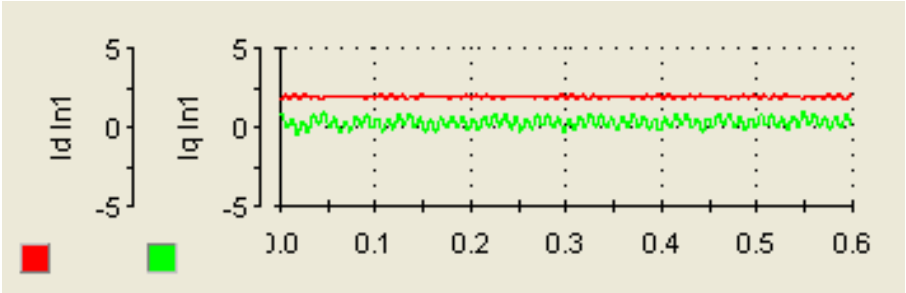

Figure 5.12: Rotor d and q current components during inverting mode at 1110rpm (26 % slip)

Figure 5.13 below shows the stator phase voltages and Figure 5.14 shows the d and q components of the stator phase voltages. As was the case for the currents, d and q voltages used in the control to calculate the PWM switching signals.

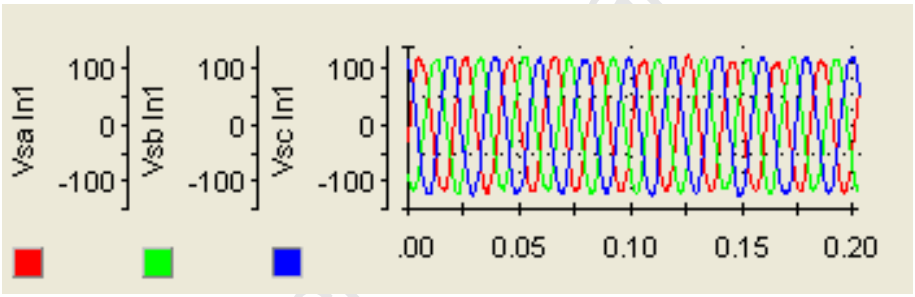

Figure 5.13: Stator Phase Voltages

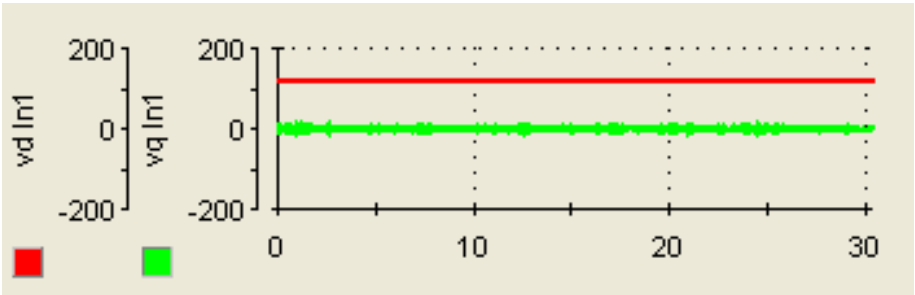

Figure 5.14: Stator d and q Voltage components

5.2.3. Synchronous speed operation

The following results illustrate the operation of the doubly fed induction generation at synchronous speed. The speed is maintained at 1500 rpm. The rotor current signals are dc signals as was observed in simulation. This is expected because at 0 % slip the rotor frequency is sf_s which is zero.

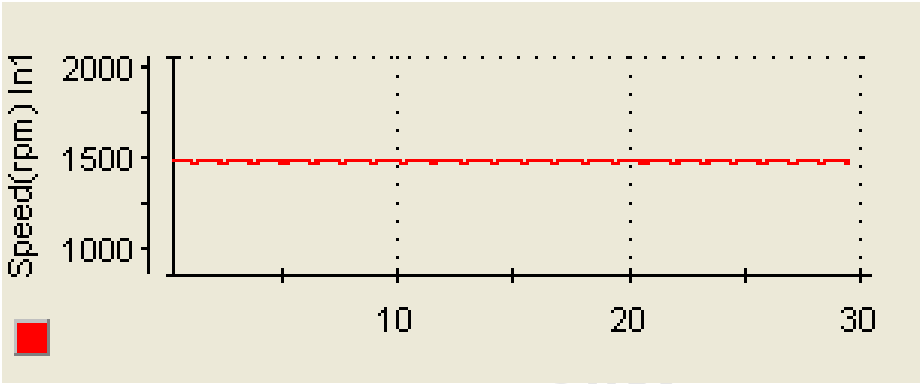

Figure 5.15: Synchronous speed operation, rotor speed maintained at 1500rpm

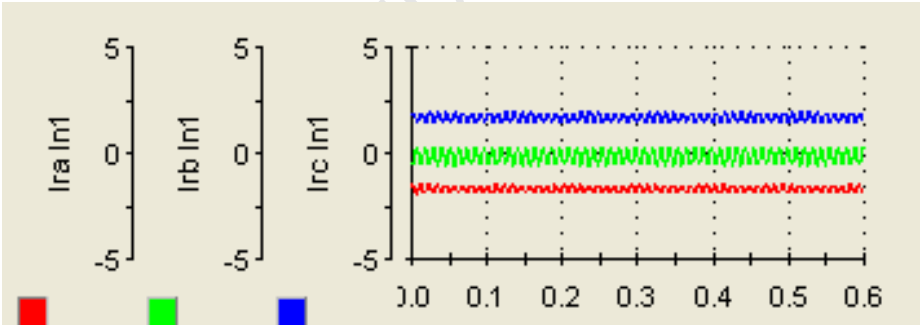

Figure 5.16: Rotor phase currents during synchronous speed operation (1500rpm)

5.2.4. Super-synchronous speed operation

The next set of results show the operation of the sub-system in super synchronous mode. The rotor is maintained at a super-synchronous speed of 1620 rpm as shown in Figure 5.17 below.

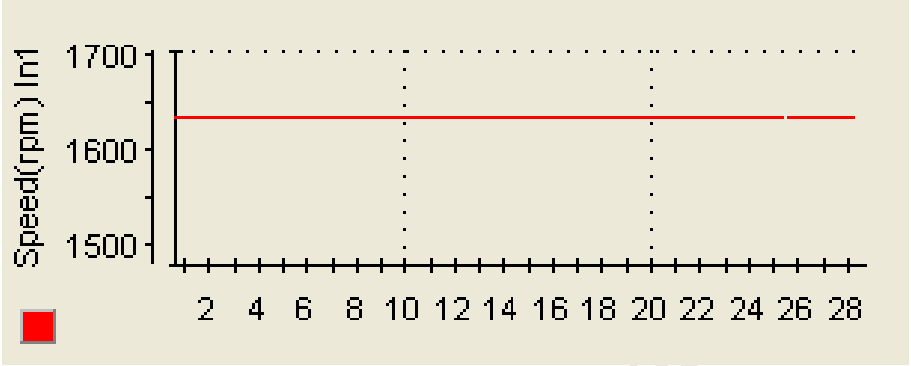

Figure 5.17: Rotor speed in super-synchronous operation maintained at 1620rpm

Figure 5.18 shows the rotor currents in super-synchronous operating mode. The currents recorded are in rectifying mode through the machine-side converter and being supplied to the grid through the grid-side inverter.

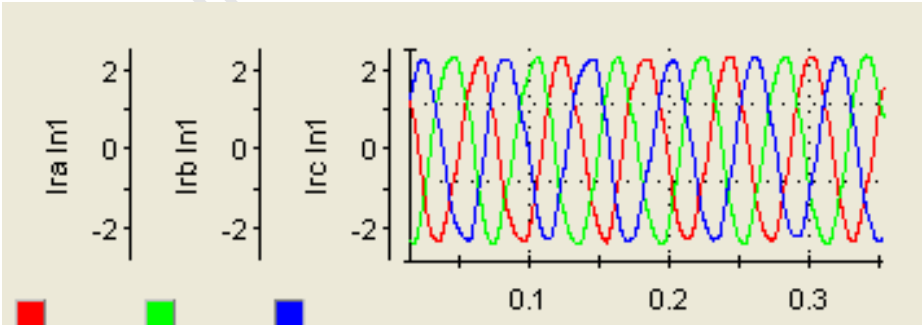

Figure 5.18: Rotor phase currents during rectifying mode at 1620rpm

The stator phase voltages are shown in Figure 5.19. As can be seen from the two the two graphs in Figure 5.18 and Figure 5.19, there is a 180° phase shift between the currents and voltages illustrates the ability of the rotor to provide bidirectional power flow [20].

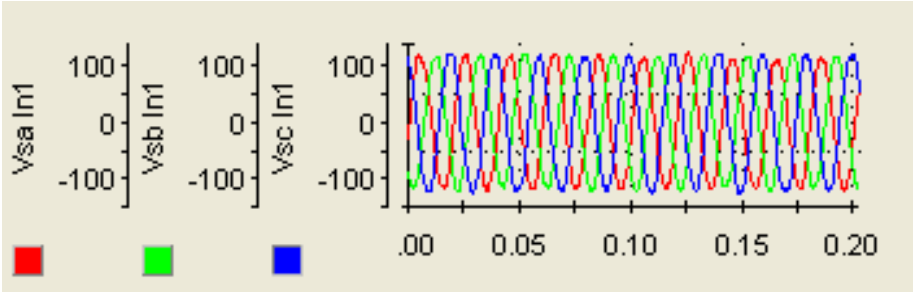

Figure 5.19: Stator Phase Voltages

5.2.5. Transient operation

The transient operation of the doubly fed induction generator machine–side converter control is investigated below. First the speed is stepped from super synchronous to sub synchronous as recorded in Figure 5.20. The behaviour of the rotor currents is shown in Figure 5.21. The rotor speed is then stepped up from sub-synchronous speed to super-synchronous speed as shown in Figure 5.22 and the behaviour of the rotor three phase currents can be seen in Figure 5.23.

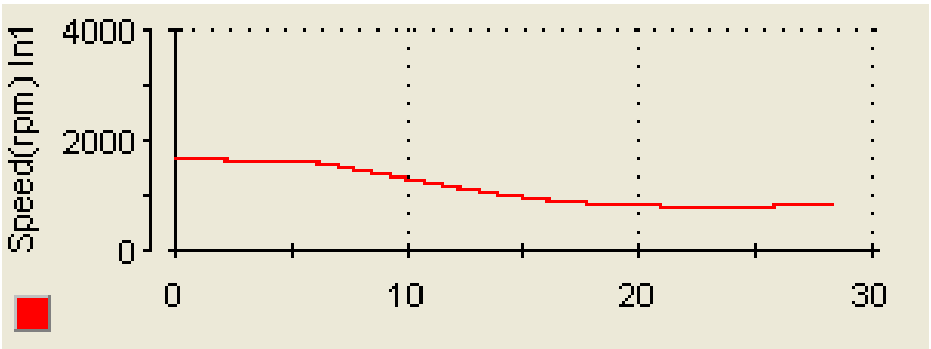

Figure 5.20: Rotor speed change from super-synchronous to sub-synchronous.

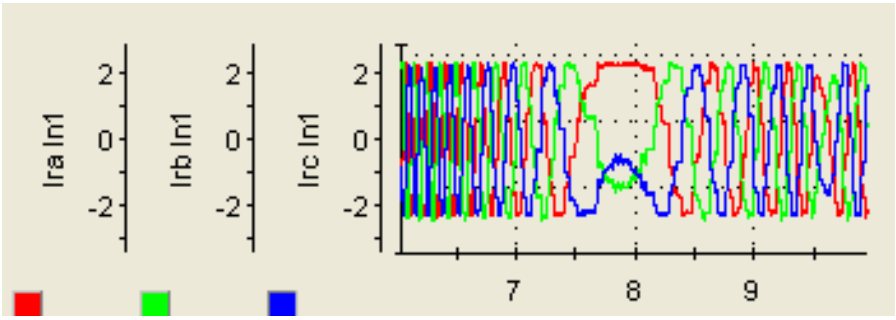

Figure 5.21: Rotor currents with speed change from sub-synchronous to super-synchronous

It can be seen clearly in the behaviour of the rotor three phase currents as they the rotor speed crosses the synchronous speed, the currents go from being ac signals to being dc signals. This is expected and has been verified through equations in Chapter 2 and in Chapter 5.2.3.

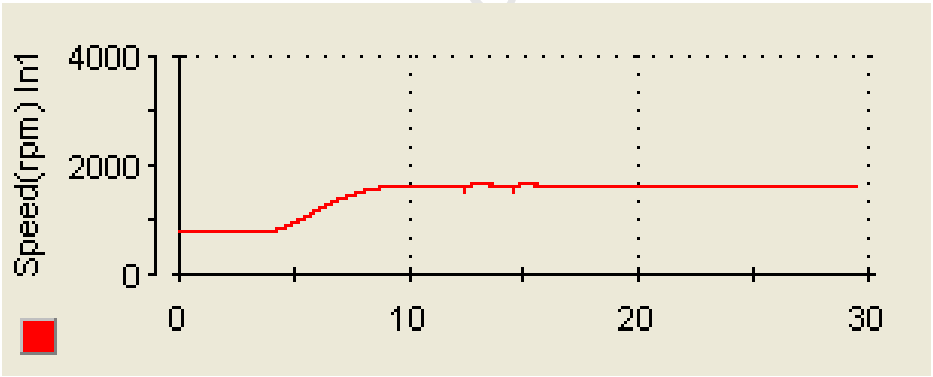

Figure 5.22: Rotor speed change from sub-synchronous to super-synchronous.

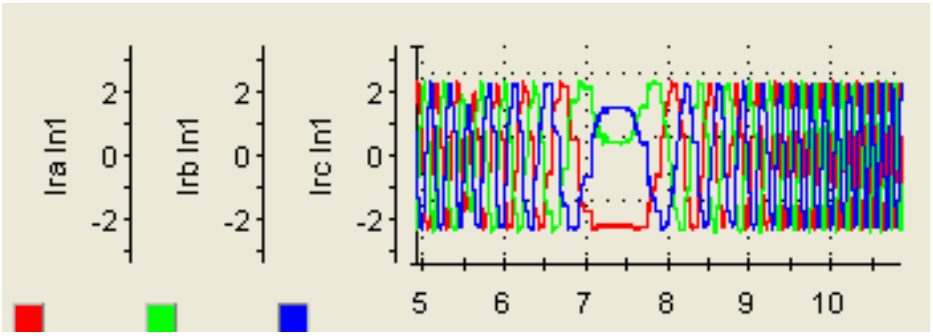

Figure 5.23: Rotor currents with speed change from sub-synchronous to super-synchronous

5.3. Grid – Side Converter Control

In order to test the operation of the grid – side converter control, it is connected as shown in Figure 5.17. It is test in inverting mode of operation as this modes test the correct operation of the PWM switching. A resistive load is connected to each phase and the DC link voltage was maintained at 300 V.

Figure 5.24: Experimental setup showing 50ohm load connected to each phase.

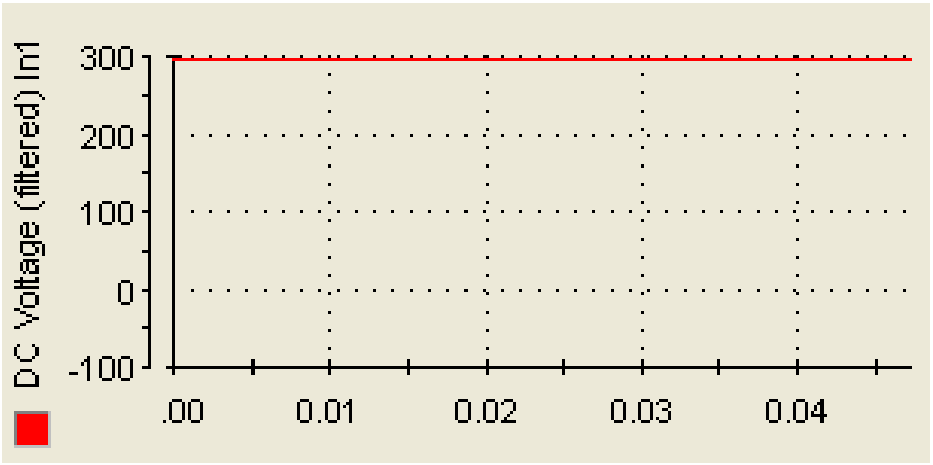

Figure 5.25: DC Link Voltage

The Bus is maintained at 300 V as shown in Figure 5.18 above. The grid – side inverter three phase currents and q and d current components are recorded below in Figures 5.19 and 5.20 respectively.

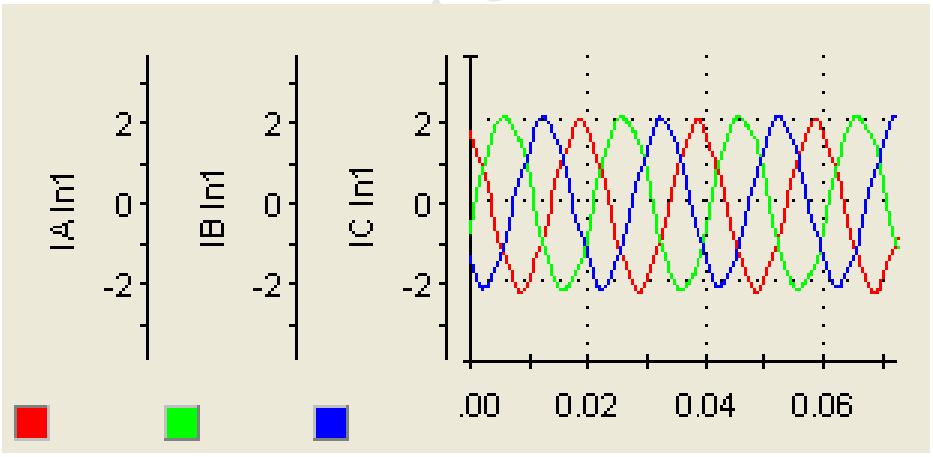

Figure 5.26: Grid – Side inverter three phase currents in inverting mode

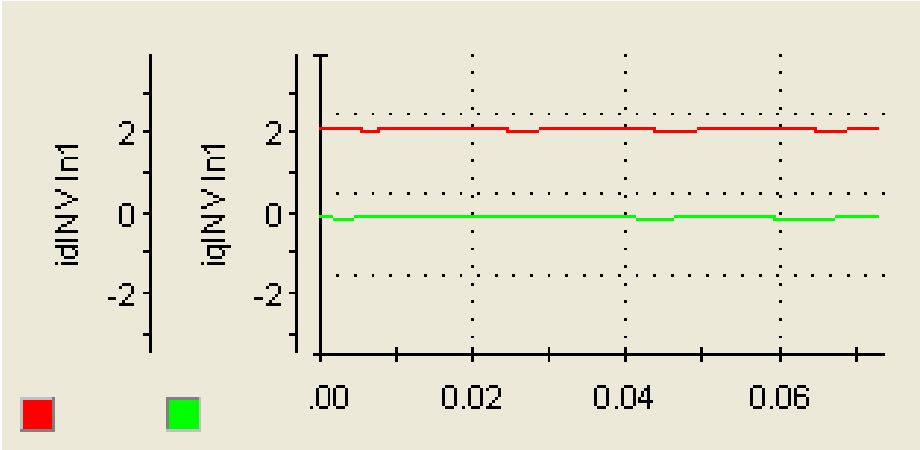

Figure 5.27: Grid – side converter direct and quadrature axis current components

The three phase voltages produced by the grid – side inverter as well as the calculated d and q voltage components are shown below in Figures 5.21 and 5.22 respectively. The produced voltages and currents are in phase as both signals are produced by inverting the voltage via the DC Link from dc to ac.

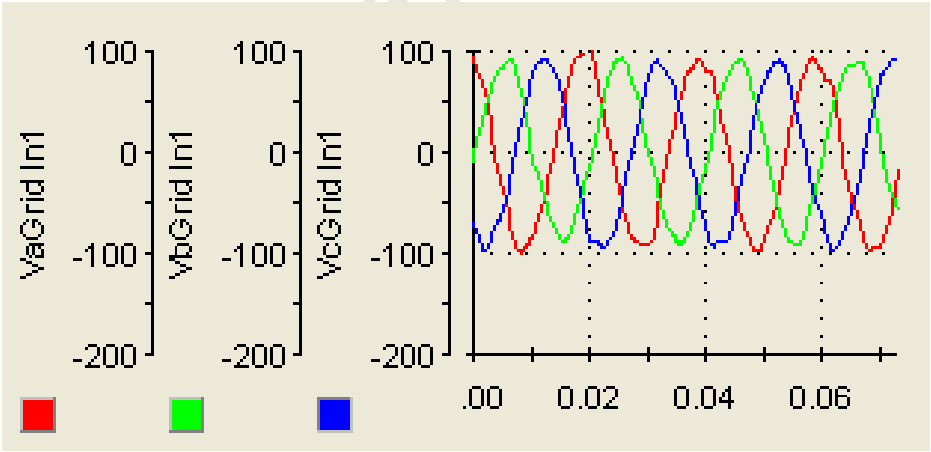

Figure 5.28: Grid three phase voltages

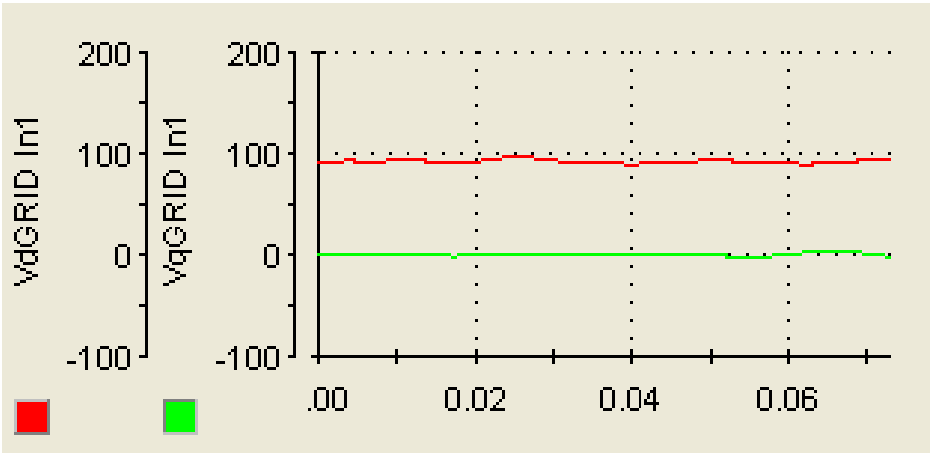

Figure 5.29: Grid direct and quadrature axis voltage components

The real and reactive power are calculated from the currents and voltages recorded, and are displayed in Figure 5.23 below.

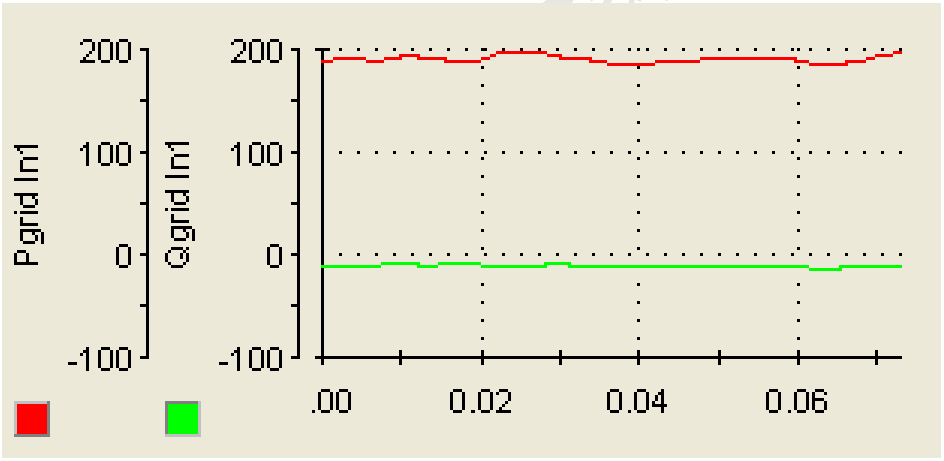

Figure 5.30: Real and reactive power

5.4. Overall System Control

The system is now tested with both machine–side converter and grid–side converter on and both connected in the topology shown in the Figure 5.31 below

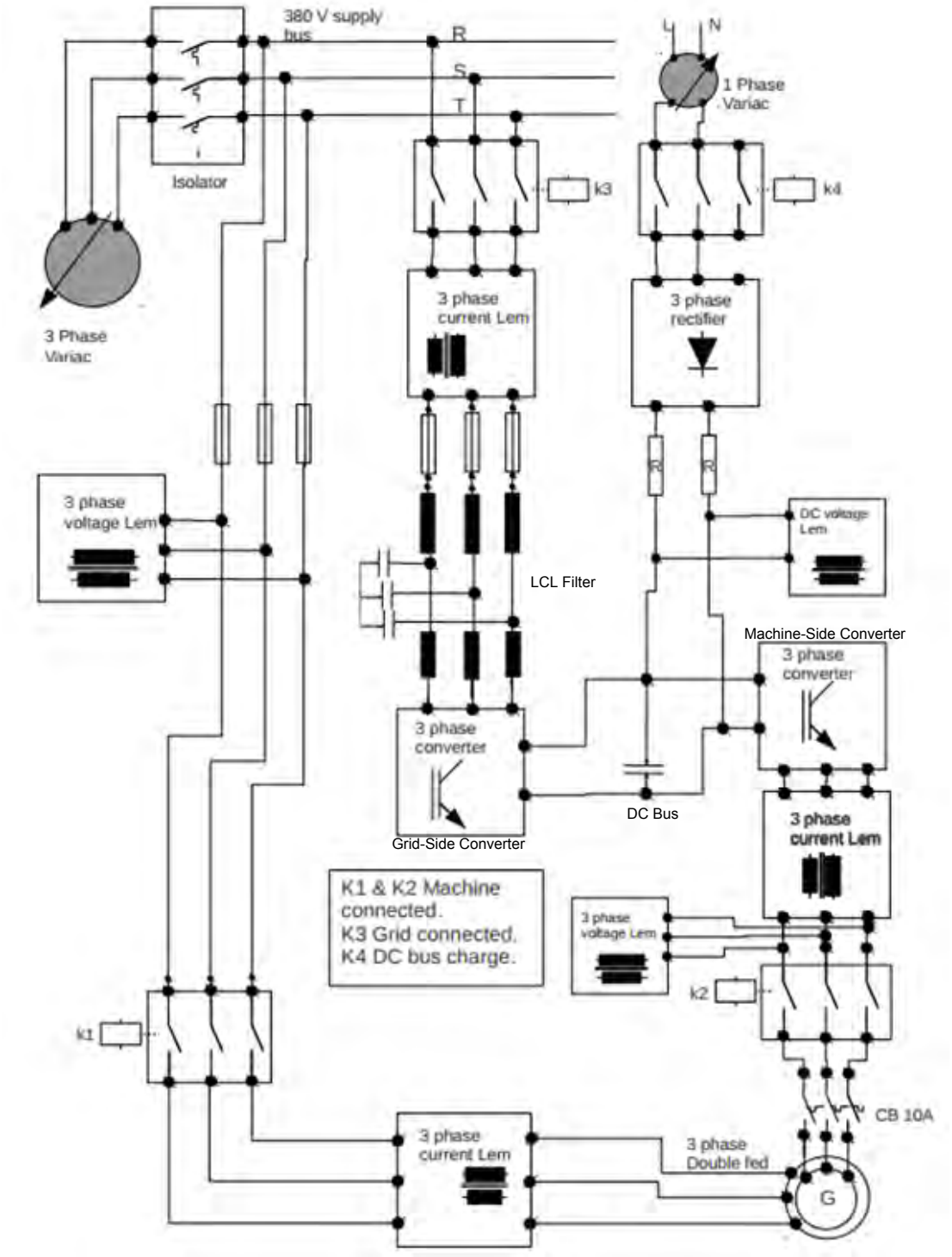

Figure 5.31: Whole system topology for experimental setup

5.4.1. Balance

The DC link voltage is maintained at 300 V as in the sub-system modes of operation. The rotor speed in super-synchronous and the DFIG is supplying power to the grid. This is a balanced condition because there is no variation in the amplitude, frequency and phase angles of either the voltages or the currents. Below are the operating results obtained including the calculated d and q components of the voltages and currents, and the calculated power being supplied to the grid. Under these balanced conditions, the reactive current and power are shown to be zero.

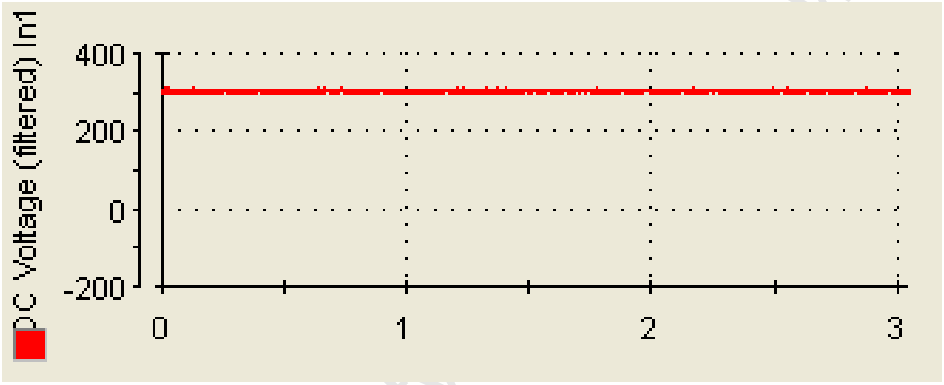

Figure 5.32: DC Link Voltage

Figure 5.33 below shows the grid-side converter three phase currents and Figure 5.34 shows the d and q quadrature axis currents obtained by transformations coded in the control.

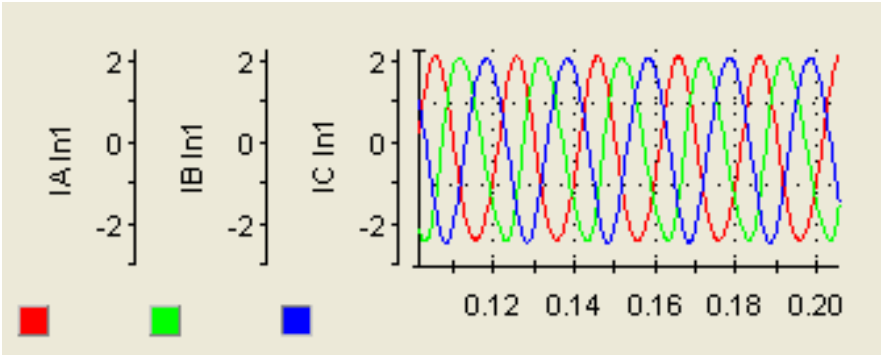

Figure 5.33: Grid – Side converter three phase currents

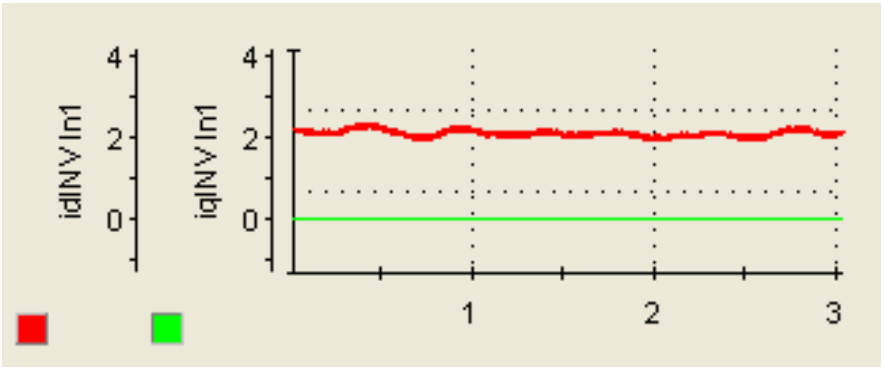

Figure 5.34: Grid – side converter direct and quadrature axis current components

The three phase voltages from the grid are also measured and shown below in Figure 5.35. The transformation to d and q axis is computed in the control and the resulting d and q axis voltages are shown in Figure 5.36.

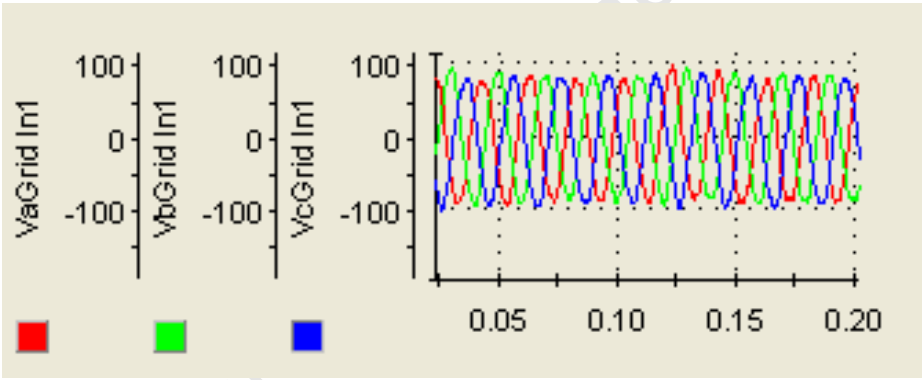

Figure 5.35: Grid three phase voltages

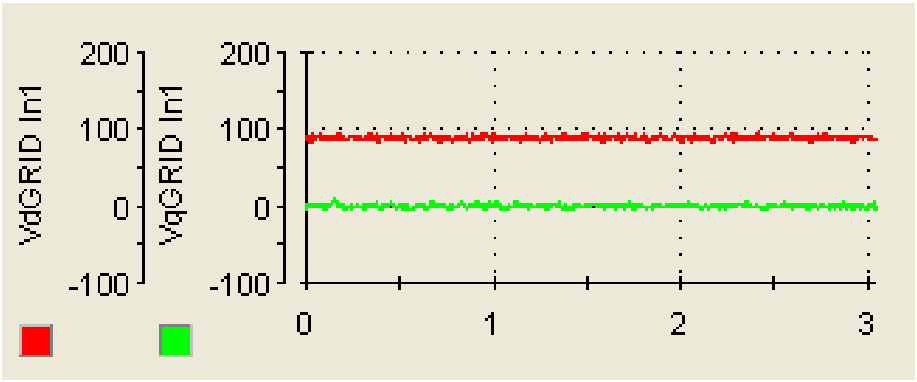

Figure 5.36: Grid direct and quadrature axis voltage components

From the d and q axis components of the grid voltage and current, the real and reactive power is calculated and the resulting powers are shown in Figure 5.37 below.

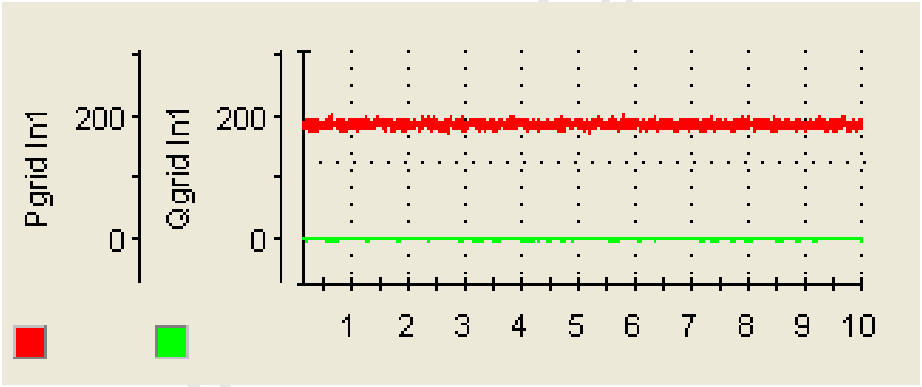

Figure 5.37: Real and reactive power

5.4.2. Reactive power Capability

The results below show the reactive power capability of the DFIG. Partially Increasing the rating of the machine – side converter has the effect of increasing the reactive power capability of the DFIG. Other factors that have been identified to affect the amount of reactive power that can be produced by the DFIG include the rotor current, stator current and rotor voltage limits [37].

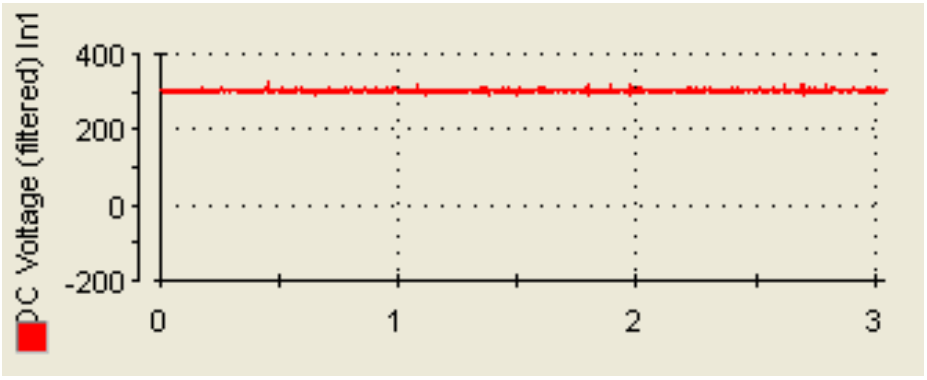

Figure 5.38: DC Link Voltage

The reactive q current component is controlled at -3 A as was done in MATLAB/Simulink Figure 4.25. There is no change in the d component of the current and this demonstrates the independent control of the d and q current components as was verified in MATLAB/Simulink operation in Chapter 4.

The change in the q component of the current can also be seen in the increase of the amplitude of the inverter three phase currents in Figure 5.39.

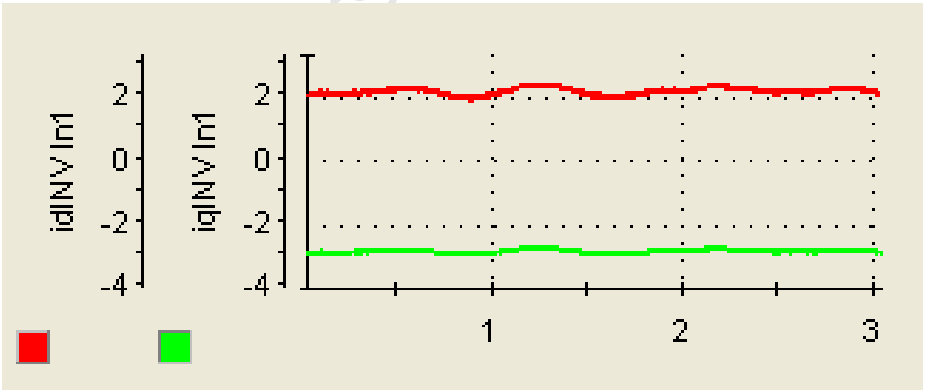

Figure 5.39: Grid side converter direct and quadrature axis current components

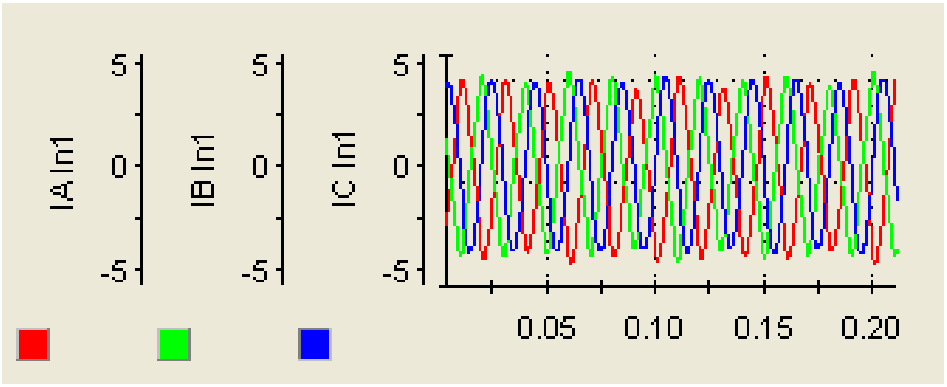

Figure 5.40: Grid – Side inverter three phase currents

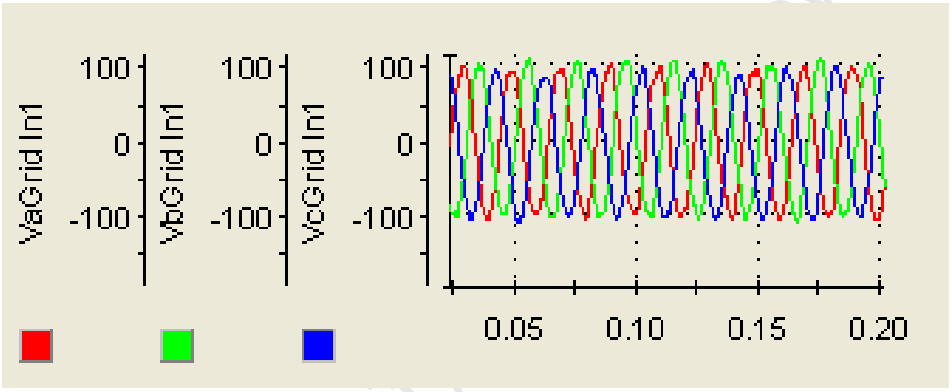

Figure 5.41: Three phase grid voltages

Figure 5.34 below shows the calculated reactive power. The reactive power is no longer zero but is proportional to the increase in the reactive q component of the current; this illustrates the DFIG ability to provide reactive power. Work on the limits of the reactive power that can be provided by the capacity of DFIG. Further work on the regulations on the active and reactive power has been conducted in [38] and [39].

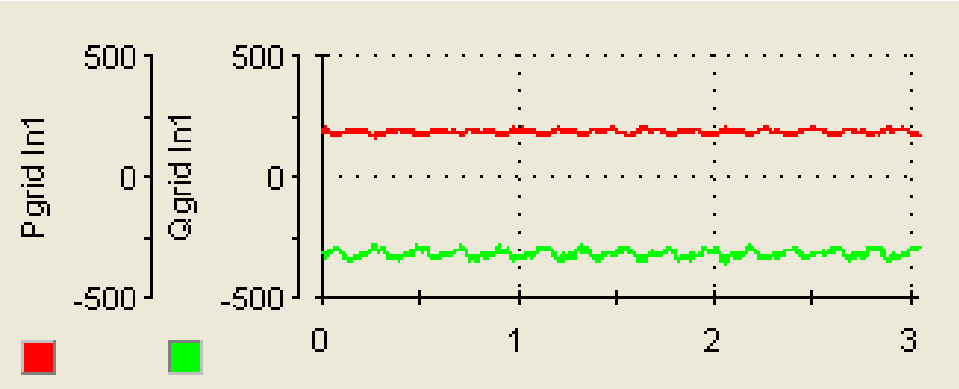

Figure 5.42: Real and reactive power with i_q = -3 A

5.4.3. Unbalance with Standard Vector Control

A three phase voltage dip at 50 % and an over voltage at 30 % were implemented in MATLAB/Simulink to demonstrate the stability of the control of the overall system as well as possibility of the DFIG to produce ancillary services.

In the physical experimental system however, a single phase voltage dip, also known as a Type B dip, was implemented. To implement the Type B dip, resistance of one phase is increased; this leads to current increase in a single phase due to reduced impendence. Figure 5.43 shows the current and voltage space vectors during this kind of dip. The three phase variac shown in Figure 5.46 was used to implement the unbalance.

As it can be seen in Figure 5.43 obtained from the work done in [40], one of the phases has a lower amplitude, This is an example of a Type B dip. This will now be implemented experimentally and the operating results will be discussed in the section.

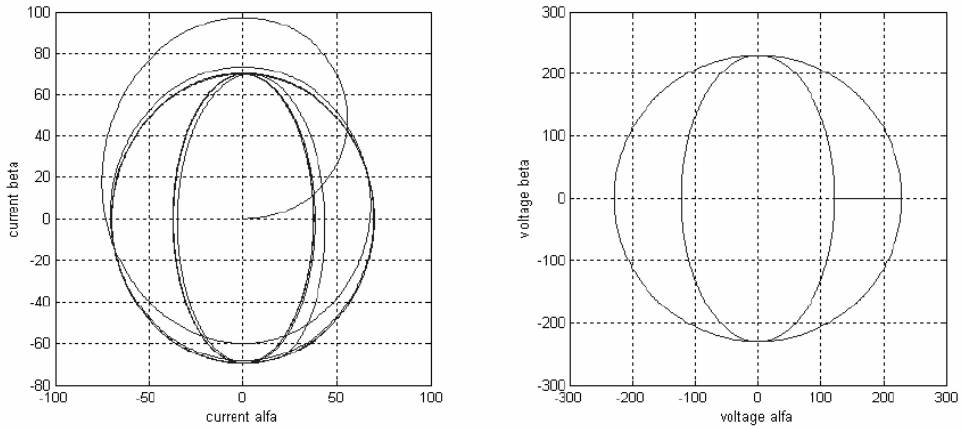

Figure 5.43: Current and Voltage space vectors during a type B voltage dip [40]

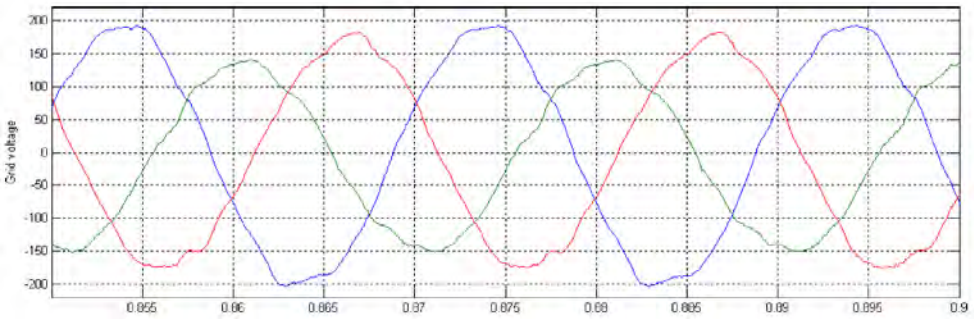

Figure 5.44: Shape of the Grid Voltages during a type B voltage dip [40]

Figure 5.45: Three phase variac used to implement voltage unbalance

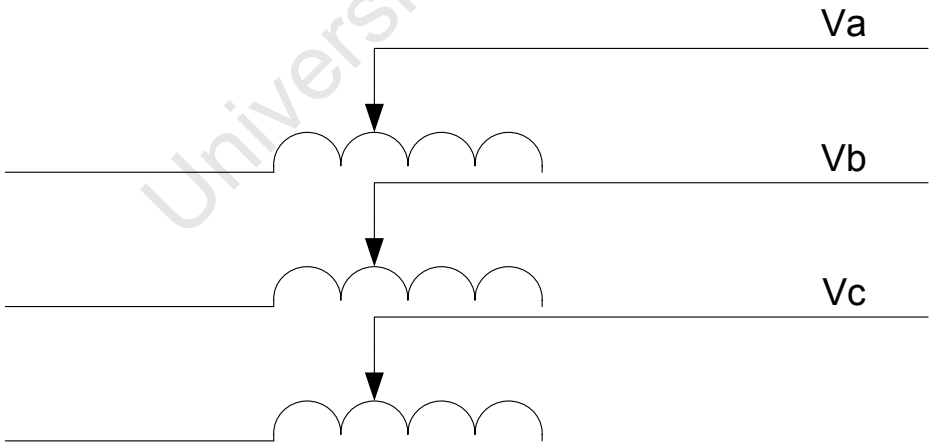

Figure 5.46: Block diagram of three-phase variac used to implement voltage unbalance

The results below show the voltage and currents taken during balanced grid conditions with standard vector control being implemented. I_q is zero and this is necessary to ensure operation at unity power factor.

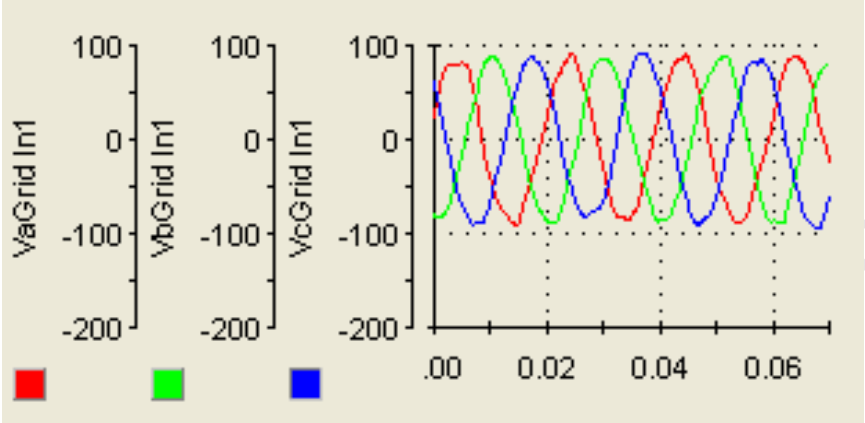

Figure 5.47: Balanced three phase grid voltages

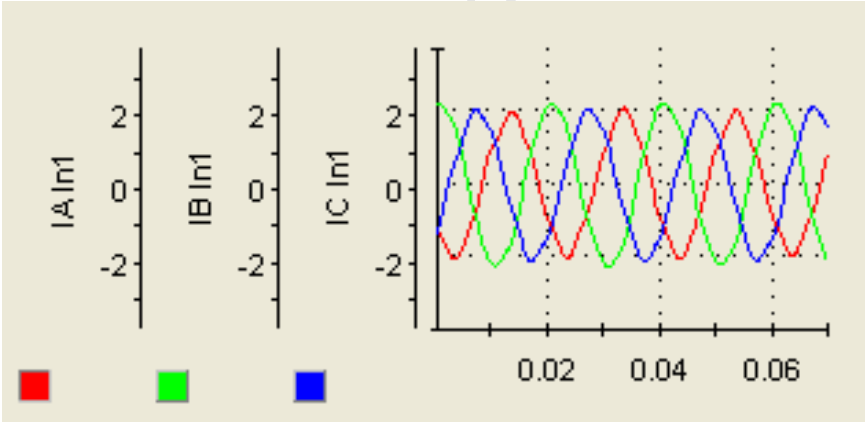

Figure 5.48: Grid –side inverter three phase currents for balanced grid voltage

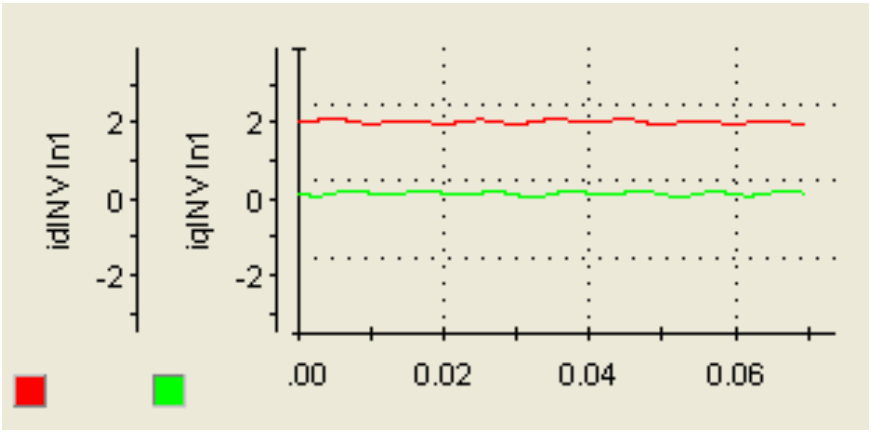

Figure 5.49: Grid – side inverter direct and quadrature axis current components for balanced grid voltage

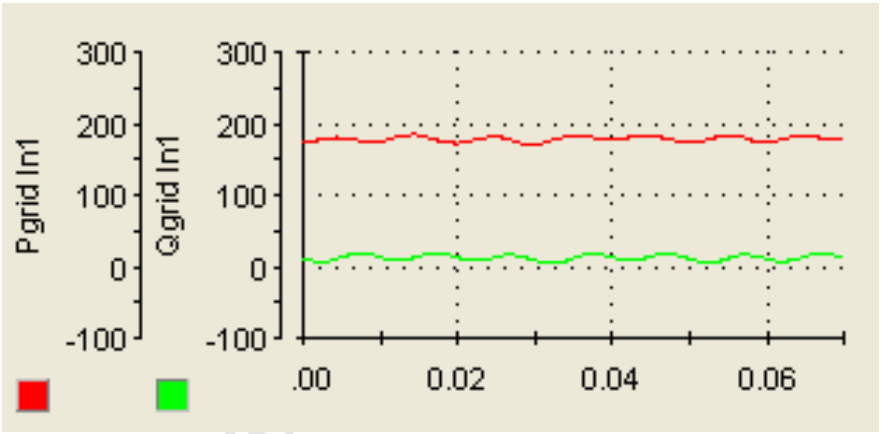

Figure 5.50: Real and reactive power measured after grid – side inverter

A type B dip is now introduced into the system on the red phase as shown in Figure 5.51 below. Phase A voltage is reduced by 10 % and the effects of this dip on the current is shown in Figure 5.52. As was mentioned a type B dip occurs when the resistance in lower in one phase hence the current is expected to increase along the phase with the fault as has been demonstrated by the increase in one phase of the current signals.

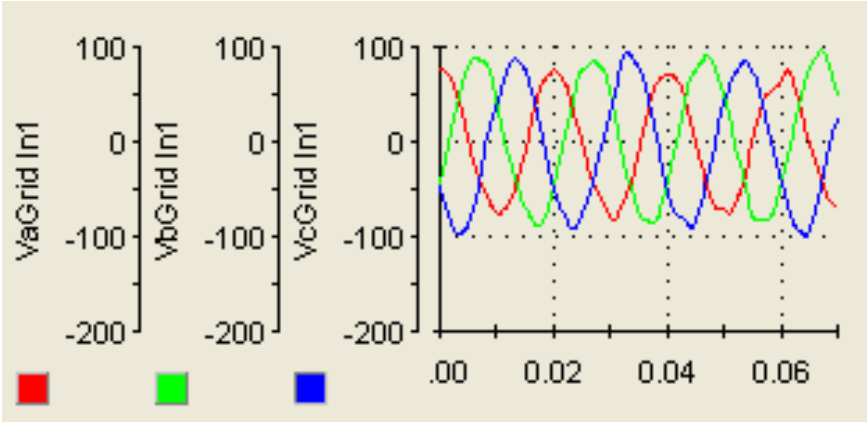

Figure 5.51: Grid Voltages during a type B voltage dip

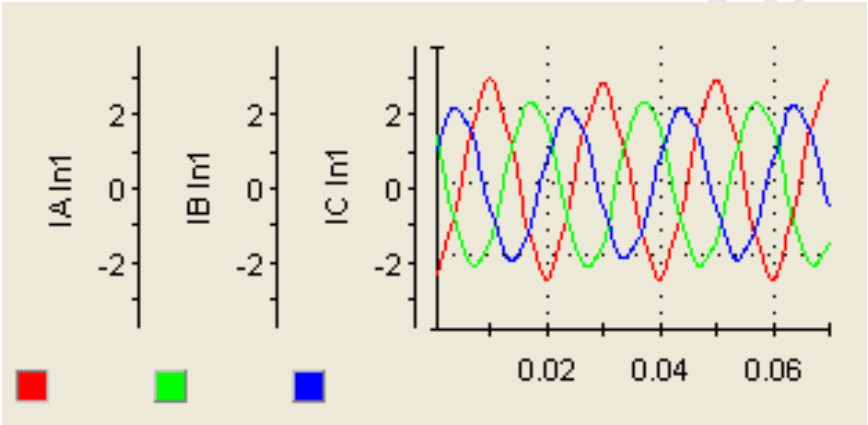

Figure 5.52: Grid –side inverter three phase currents with a Type B dip on grid voltage

5.4.4. Unbalance with Dual Vector Current Control

The same unbalance is introduced into the system with dual vector current control being implemented. As can be seen in Figure 5.54, the three phase currents are more stable and this is due to the fact the in dual vector current control the quadrature axis current component and the negative current sequence components are maintained at zero [41].

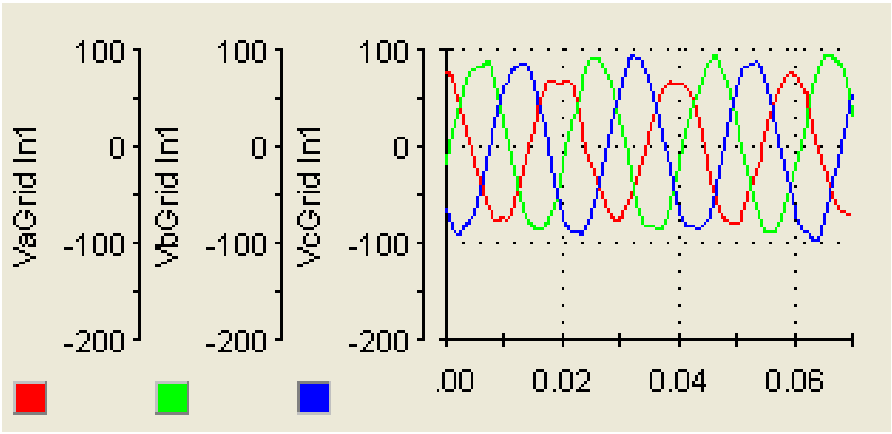

Figure 5.53: Grid Voltages with a type B voltage dip

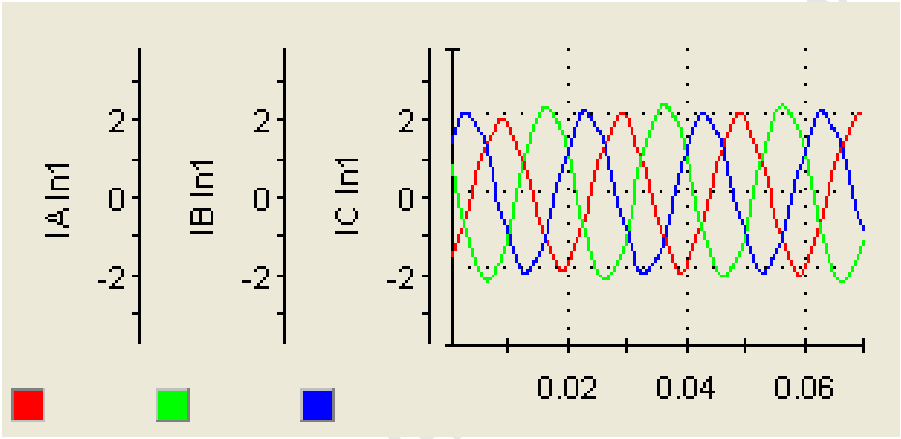

Figure 5.54: Grid – side inverter three phase currents with type B voltage dip and dual vector current control implemented

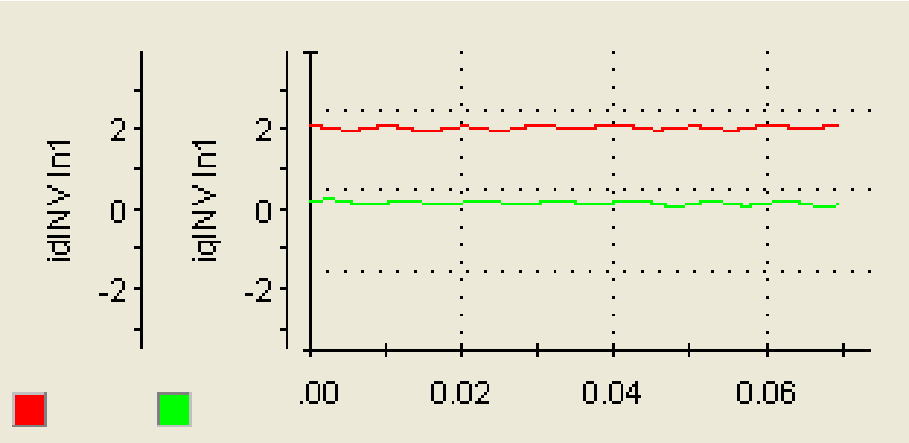

Figure 5.55: Grid – side inverter direct and quadrature axis current components with type B voltage dip and dual vector current control implemented

The operating results of the current components with dual vector current control implemented are shown in Figure 5.56 and Figure 5.57. The current is separated into its negative and positive d components and into its negative and positive q components. These components are then controlled independently by the implementation of dual vector current control (DVCC). In order to maintain stability under grid unbalances, the negative sequence components are set to zero. The positive q current component is also maintained at zero to ensure unity power factor.

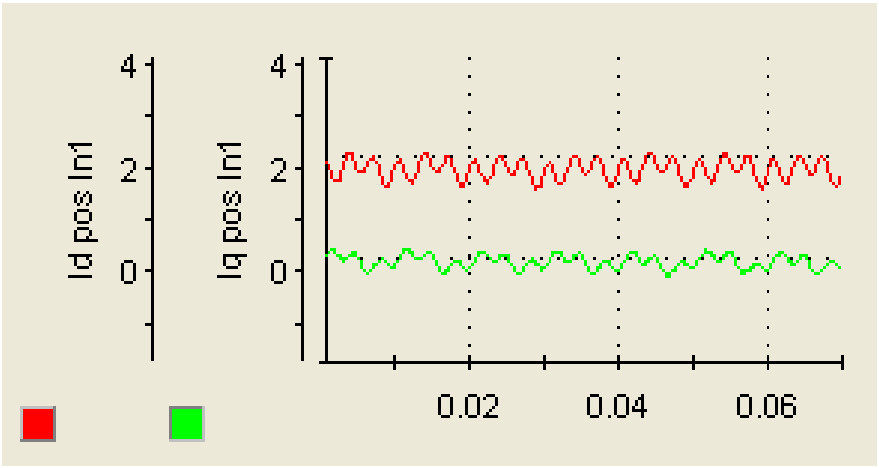

Figure 5.56: Grid – side inverter direct and quadrature axis positive sequence current components with type B voltage dip and dual vector current control implemented

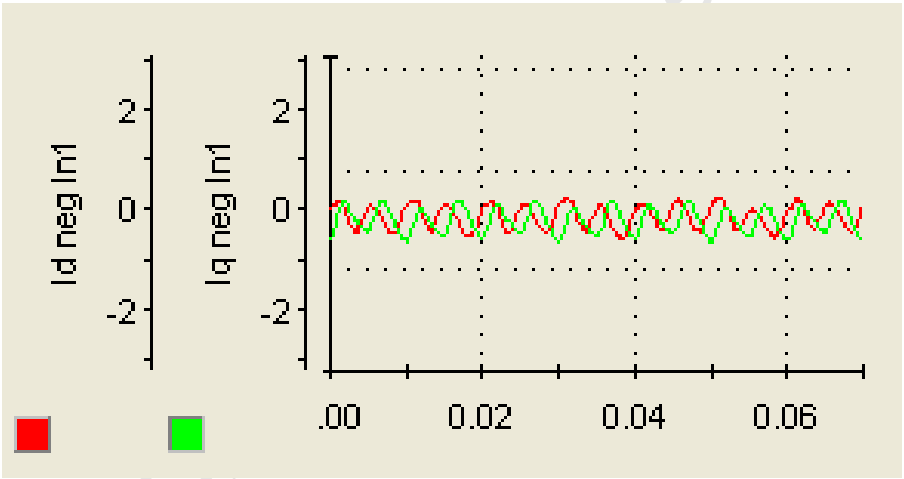

Figure 5.57: Grid – side inverter direct and quadrature axis negative sequence current components with type B voltage dip and dual vector current control implemented

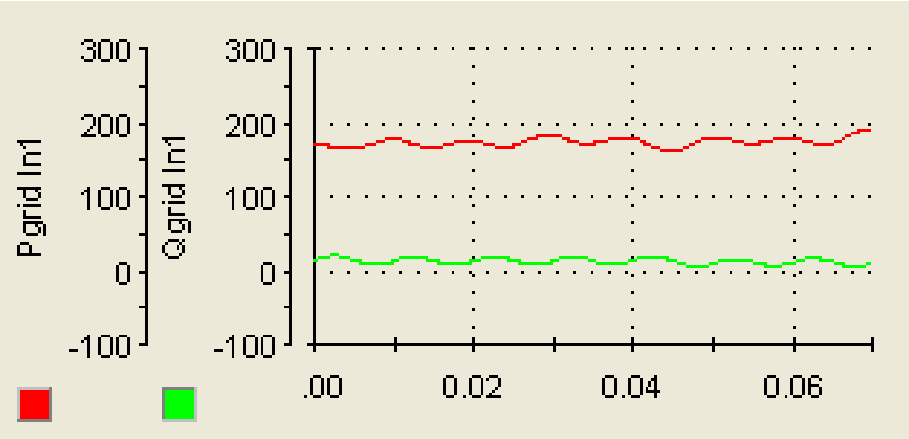

Figure 5.58: Real and Reactive power during a type B voltage dip with DVCC implemented

5.5. Conclusion

The operation of the whole system has been verified. First the correct operation of each sub-system was verified and the operating results were recorded and discussed. The machine-side sub-system control was shown to be stable in transient operation. The operating results of the grid-side sub-system were also recorded and discussed. The independent control of the d and q current components was demonstrated, as well as the reactive power capability and the use of dual vector current control to ensure stability of the system during unbalanced grid voltage conditions.

6. COMPARISON AND DISCUSSION OF RESULTS

Machine – Side Converter

- Sub–synchronous operation; the simulated model and experimental model both operated as expected.
- Synchronous speed operation; during this mode of operation it was validated both in simulation and experimental that the rotor currents and voltages obtained are dc signals. This is due to 0 slip of the rotor speed in relation to synchronous speed and hence slip frequency, f_s, is also 0. The rotor currents and voltages therefore do not change with time but are constant.
- Super – synchronous speed operation; the machine operated as expected.

Operation in the above three modes confirmed the ability of the doubly fed induction generator to operate in sub, synchronous and super synchronous modes of operation. Speed control through the machine–side converter was also demonstrated both in simulation and experimentally as well the ability of the machine side converter to operate in inverting and rectifying mode.

Grid – Side Converter

The Reactive power capability of the doubly – fed induction generator was verified both in simulation and experimentally.

In MATLAB/Simulink 50% voltage dip and 30% three phase over voltage where implemented, while a 10% type B dip was implemented experimentally. The use of control techniques, specifically dual vector current control in this case, to stabilise the system during the gird voltage unbalances was verified both in software and experimentally.

7. CONCLUSIONS

Based on the complete doubly-fed induction generator wind energy conversion system presented here, the following conclusions have been drawn:

1. **Complete Doubly – Fed Induction Generator system for integration studies**

   A complete DFIG system has been modelled mathematically, in MATLAB/Simulink as well as set-up of physical experimental system has been achieved. The operation of the experimental set-up has been verified by tests in transient operation and demonstration of reactive power capability. It has also been tested with balanced and unbalanced grid voltage and the control has been verified to be stable in both cases.

2. **Control of Doubly – Fed Induction Generator during transient operation**

   The operation of the rotor–side converter sub-system was verified by various tests including transient operation where the speed was swept from sub-synchronous to super-synchronous. The correct operation and stability of the control during this operation verified that the mathematical model equations and modelling of software were correct as well as the verification of correct operation of the experimental system as well.

3. **Testing of Machine-side and grid – side converters in inverting and rectifying modes.**

   The correct operation of the back to back converter and other components were test by running the machine-side and grid side converters in inverting and rectifying modes. The correct voltage and current measurements obtained further verified correct Space Vector PWM switching.

4. Grid – Side inverter LCL Filter design and implemented

An LCL filter was design analytically and then implemented in hardware. Its operation was verified by the smooth signal obtained after the grid – side inverter despite the high switching frequency employed by the switches.

5. Effect of Grid unbalance demonstrated and corrected with control systems

The effect of an unbalanced grid voltage on the doubly – fed induction generator system signals has been demonstrated by implementing a 10% voltage drop in one phase of the grid voltage, also known as a type B dip. It was shown that the currents are unstable. This successfully corrected by implementing dual vector current control as opposed to just standard vector control. The effects were shown by stable currents and control despised the unbalance being present in the system.

6. DFIG for grid integration studies

The tests carried out on the DFIG wind generator system including operation unbalanced grid voltage conditions shows that the system was successful for tests on grid integration.

8. RECOMMENDATIONS

From the results obtained, it has been validated that the system is fully functional. However, the following recommendations have been made as work that could be done to further improve the system.

- Employ method 2 in Chapter 5 as a start up procedure; using DC Bus voltage to run motor to synchronous speed and then switching in the stator at this point so as to connect and synchronize it to the grid. This would enhance the automation of the system and reduce the number components in the system.
- In order to increase the Fault Ride Through capabilities of the system, crowbar protection could be added to the system.

References

[1] http://www.ewea.org/wind-energy-basics/ Web accessed on 11 May, 2013.

[2] http://www.ewea.org/fileadmin/files/library/publications/statistics/Wind_in_power_annual_statistics_2012.pdf '*Wind in Power 2012 European Statistics*'. Web accessed on 16 March 2013.

[3] http://www.energy.gov.za/IRP/irp%20files/IRP2010_2030_Final_Report_20110325.pdf '*INTEGRATED RESOURCE PLAN FOR ELECTRICITY, 2010 -2030, Revision 2'*. Final Report, pg 9. 25 March 2011. Accessed in July 2013

[4] R. Swisher, C. De Azua and J. Clendenin, "*Strong Winds on the Horizon: Wind Power Comes of Age*" *Proceedings of IEEE, Vol. 89, No. 12, 2001.*

[5] T. Jin and Z. Tian, "*Uncertainty Analysis for Wind Energy Production with Dynamic Power Curves*" IEEE, PMAPS, 2010.

[6] J. Martinez, P. C. Kjaer and R. Teodorescu, "*DFIG Turbine Representation for Small Signal Voltage Control Studies*" *IEEE 12th Conference on Optimization of Electrical and Electronic Equipment, OPTIM,* 2010.

[7] S. Li, T.A. Haskew, K.A. Williams and R.P. Swatloski, "*Control of DFIG Wind Turbine with Direct-Current Vector Control Configuration*" *IEEE Transactions on Sustainable Energy, Vol. 3 No.1*, January 2012.

[8] A. Larsson; "*The Power Quality of Wind Turbines*" Thesis for Degree of Doctor of Philosophy, Chalmers University of Technology, 2000.

[9] T. Yeh and L. Wang*, "A Study on Generator Capacity for Wind Turbines under Various Tower Heights and Rated Wind Speeds Using Weibull Distribution"* IEEE Transanctions on Energy Conversion, Vol. 23, No. 2, June 2008.

[10] *wiki.windpower.org/index.php/Betz'_law, accessed 19-11-12*

[11] F. L. Luo, "Design *of Wind-Turbine Energy System*." IEEE IPEC, 2010.

[12] O. Soares, H. Goncalves, A. Martins and A. Carvalho, "*Nonlinear control of the doubly-fed induction generator in wind power systems*." 2010.

[13] G. Abad, J. Lopez, M.A. Rodriguez, L. Marroyo, G. Iwanski, "*Doubly Fed Induction Machine Modeling and Control for Wind Energy Generation*" IEEE Press, John Wiley & Sons, INC., Publication, 2011.

[14]L. Munteanu, A.L. Bratcu, N. Cutululis and E. Caenge. "*Optimal Control of Wind Energy Systems*" Advances in Industrial Control, 2008.

[15]A*.A.K. Gupta, B.H. Bhushan and C.P. Samuel, "Generator Topologies with Power Electronics Converters for a Wind Energy Conversion System: A Review". 2011.*

[16]M*. Molinas, B. Naess, W. Gullvik and T. Undeland; "Cage Induction Generators for Wind Turbines with Power Electronics Converters in the Light of the New Grid Codes." EPE 2005.*

[17]S.A. Shaheen, H.M. Hasanien and M.A. Badr, "Study on Doubly Fed Induction Generator Control." Proceedings, MEPCON, December.

[18]http://www.ewh.ieee.org/soc/es/Nov1997/09/INDEX.HTM Web accessed on 7 July, 2013

[19]Q*. Wang, L. Chang, 'PWM Control Strategies for Wind Turbine Inverters', IEEE pg 309 – 312. 1998.*

[20]P. Barendse, "*Design and Implementation of Variable Speed Wind Energy Induction Generator Systems for Fault Studies.*" In fulfilment of requirements for MSc Electrical Engineering, University of Cape Town, 2003.

[21] S*.K. Salman and B. Badrzadeh, "New Approach for modeling Doubly-Fed Induction Generator (DFIG) for grid-connection studies" Robert Gordon University*

[22] A. Petersson, L. Harnefors, and T. Thiringer, "*Comparison Between Stator-Flux and Grid-Flux-Orientation Rotor Current Control of Doubly-Fed Induction Generators*" in Proceedings 35th Power Electronics Specialist Conference, Vol. 1, Aachen, Germany, 20-25 June 2004, pp. 482-486.

[23] S. Choudhury, K.B. Mohanty and B.K. Debta, "*Investigation on Performance of the Doubly-Fed Induction Generator Driven by Wind turbine under Grid Voltage Fluctuation*". IEEE 2011.

[24] J.Hu, Y. He and L. Xu, "*Improved rotor current of wind turbine driven doubly-fed induction generators during network voltage unbalance*" Electric Power Systems Research 80, pgs 847-856. 2010.

[25] H.R. Karshenas and H. Saghafi*, "Basic Criteria in Designing LCL Filters for Grid Connected Converters" IEEE, ISIE, July 2006.*

[26]G.A. Raducu, "*Control of Grid Side Inverter in a B2B Configuration for WT Applications*". Master Thesis, Aalborg University, 2008.

[27] M. Liserre, F. Blaabjerg and S. Hansen, "*Design and Control of an LCL-Filter-Based Three-Phase Active Rectifier*". IEEE Transactions on Industry Applications, Vol. 41, No 5, pg 1281- 1291. September/October 2005.

[28] D. Mehrzad, J. Luque and M.C. Cuenca "*Vector Control of PMSG for grid-connected Wind Turbines Applications*", Master Thesis, Aalborg University, 2009.

[29] LS Mecapion Rotary Encoder (INCREMENTAL TYPE) S40 / S48 / S66 / H40 Series, Manual & Data sheet

[30] T. Wildi, "*Electric Machines, Drivers and Power Systems*", 4th Edition, Prentice-Hall, Inc., 2000.

[31] Y. Zhang, J. Jia and W. Li, "*Study on Converters for Doubly Fed Induction Generator Based Wind Power Generation System*". International Conference on Power System Technology, 2010.

[32] J. Hu and Y. He, "*Modelling and enhanced control of DFIG under unbalanced grid voltage conditions*". Electric Power Systems Research, 2008.

[33] J. L. Da Silva, R. G. De Oliveira, S. R. Silva, B. Rabelo and W. Hofman, "*A discussion about a Start-up Procedure of a Doubly-Fed Induction Generator System*". NORPIE 2008.

[34] X. Yuan, J. Chai and Y. Li "*A Doubly Fed Induction Machine Based Solution to Medium Frequency Power Supply*" IEEE 2009.

[35] E. Tremblay, A. Chandra, P.J. Lagace and R. Gagnon, "*Study of Grid-Side Converter Control for Grid-Connected DFIG Wind Turbines under Unbalanced Load Condition*". IEEE ISIE, July 2006.

[36] W. Sadara and B. Neammanee, "*Implementation of a Three Phase Grid Synchronisation for Doubly-fed Induction Generators in Wind Energy System*".

[37] S.N. Singh, J. Ostergaard and B. Singh, "*Reactive Power Capability of Unified DFIG for Wind Power Generation*". IEEE 2010.

[38] L. Sun, Z. Mi, Y. Yu, T. Wu and H. Tian, "*Active Power and Reactive Power Regulation Capacity Study of DFIG Wind Turbine*".

[39] D. Xu, R. Li, Y. Lui and Y. Lang, "*Reactive Power Analysis and Control of Doubly Fed Induction Generator Wind Farm*".

[40] M. Bobrowska-Rafal, K. Rafal, G. Abad and M. Jasinski, "*Control of PWM rectifier under grid voltage dips*" BULLETIN OF THE POLISH ACADEMY OF SCIENCES TECHNICAL SCIENCES Vol. 57, No. 4, 2009.

[41] J.G. de la Bat, *"Development of a System for Testing Grid-Connected Permanent Magnet Wind Generators"* Master Thesis, University of Cape Town 2011.

APPENDIX A: Contactor and Relay Connection

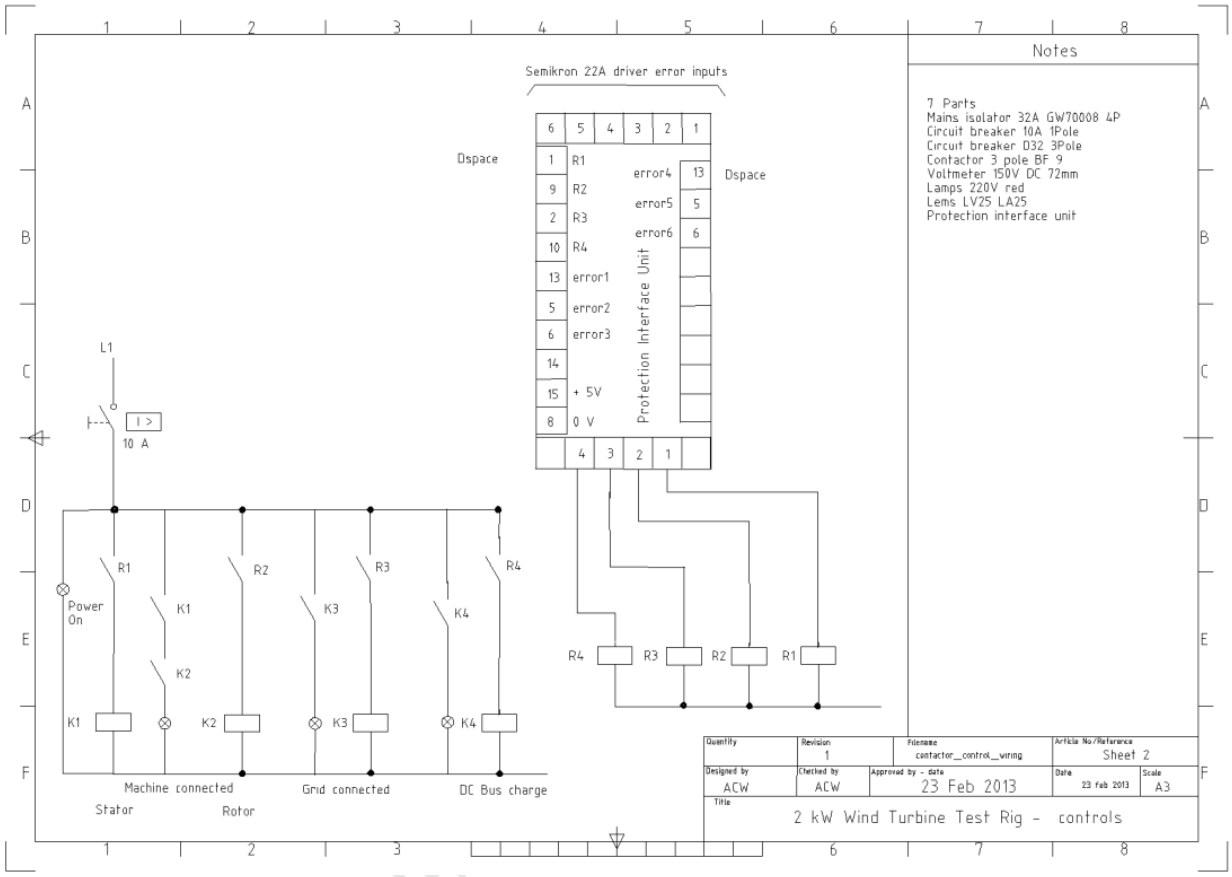

Figure A1: Contactor and Relay connection

APPENDIX B: LEM Board, Relay and Error Signal Board Circuit Design

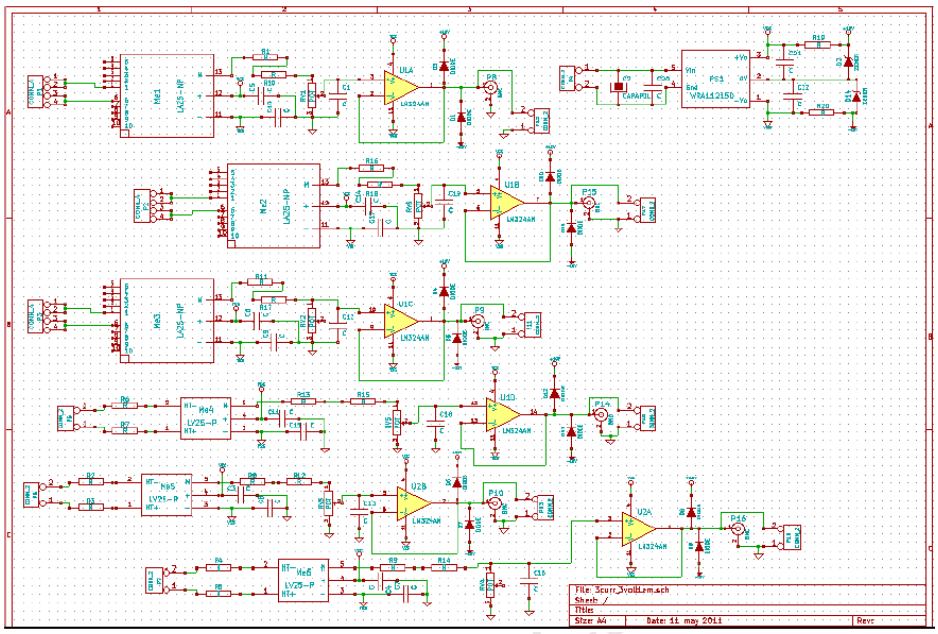

Figure B1: LEM Board Circuit Diagram (Standard for the AMES Research Group, University of Cape Town)

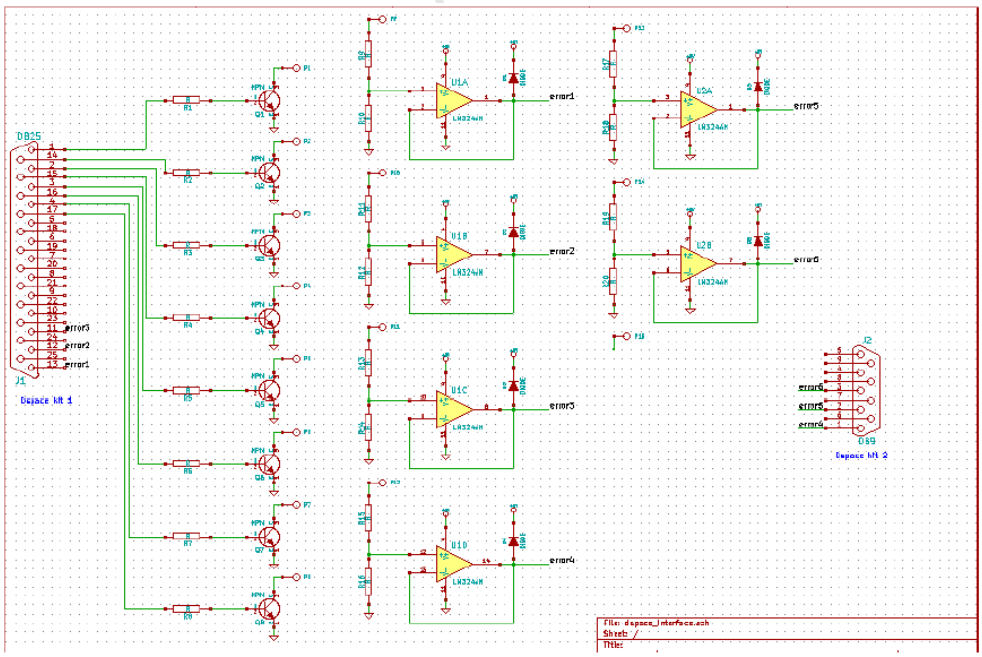

Figure B2: Relay and Error Signal Board Circuit Diagram (Standard for the AMES Research Group, University of Cape Town)

APPENDIX C: Data Sheet and Manual for LS Mecapion Rotary Encoder

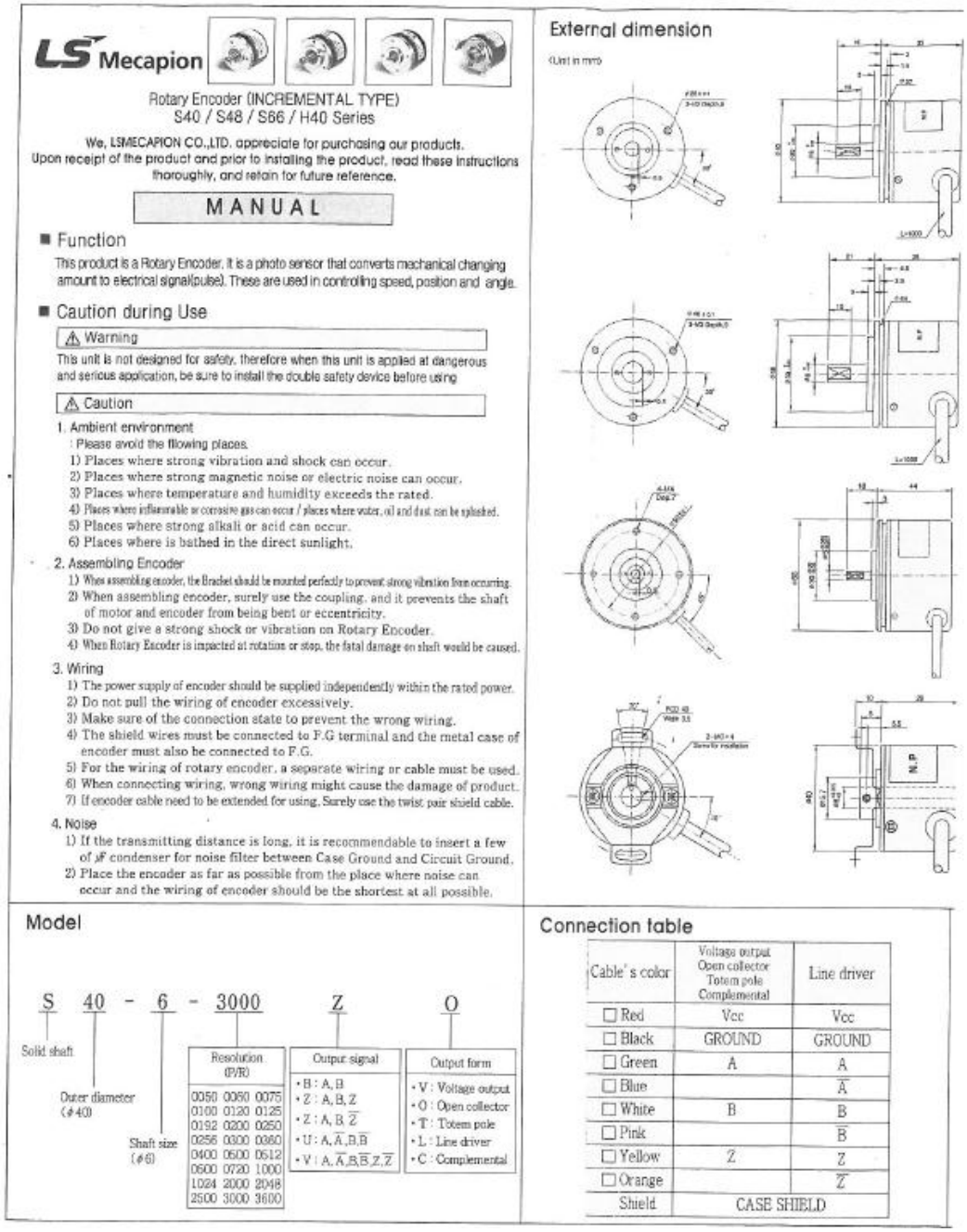

LS Mecapion

Rotary Encoder (INCREMENTAL TYPE)
S40 / S48 / S66 / H40 Series

We, LSMECAPION CO.,LTD. appreciate for purchasing our products.
Upon receipt of the product and prior to installing the product, read these instructions thoroughly, and retain for future reference.

MANUAL

■ Function

This product is a Rotary Encoder. It is a photo sensor that converts mechanical changing amount to electrical signal(pulse). These are used in controlling speed, position and angle.

■ Caution during Use

⚠ Warning

This unit is not designed for safety, therefore when this unit is applied at dangerous and serious application, be sure to install the double safety device before using

⚠ Caution

1. Ambient environment
   : Please avoid the flowing places.
   1) Places where strong vibration and shock can occur.
   2) Places where strong magnetic noise or electric noise can occur.
   3) Places where temperature and humidity exceeds the rated.
   4) Places where inflammable or corrosive gas can occur / places where water, oil and dust can be splashed.
   5) Places where strong alkali or acid can occur.
   6) Places where is bathed in the direct sunlight.
2. Assembling Encoder
   1) When assembling encoder, the Bracket should be mounted perfectly to prevent strong vibration from occurring.
   2) When assembling encoder, surely use the coupling, and it prevents the shaft of motor and encoder from being bent or eccentricity.
   3) Do not give a strong shock or vibration on Rotary Encoder.
   4) When Rotary Encoder is impacted at rotation or stop, the fatal damage on shaft would be caused.
3. Wiring
   1) The power supply of encoder should be supplied independently within the rated power.
   2) Do not pull the wiring of encoder excessively.
   3) Make sure of the connection state to prevent the wrong wiring.
   4) The shield wires must be connected to F.G terminal and the metal case of encoder must also be connected to F.G.
   5) For the wiring of rotary encoder, a separate wiring or cable must be used.
   6) When connecting wiring, wrong wiring might cause the damage of product.
   7) If encoder cable need to be extended for using, Surely use the twist pair shield cable.
4. Noise
   1) If the transmitting distance is long, it is recommendable to insert a few of μF condenser for noise filter between Case Ground and Circuit Ground.
   2) Place the encoder as far as possible from the place where noise can occur and the wiring of encoder should be the shortest at all possible.

External dimension

(Unit in mm)

Model

S 40 - 6 - 3000 Z O

- Solid shaft
- Outer diameter (φ40)
- Shaft size (φ6)

Resolution (P/R)			
0050	0060	0075	
0100	0120	0125	
0192	0200	0250	
0256	0300	0360	
0400	0500	0512	
0600	0720	1000	
1024	2000	2048	
2500	3000	3600	

Output signal
- B : A, B
- Z : A, B, Z
- Z : A, B, $\overline{Z}$
- U : A, $\overline{A}$, B, $\overline{B}$
- V : A, $\overline{A}$, B, $\overline{B}$, Z, $\overline{Z}$

Output form
- V : Voltage output
- O : Open collector
- T : Totem pole
- L : Line driver
- C : Complemental

Connection table

Cable's color	Voltage output Open collector Totem pole Complemental	Line driver
☐ Red	Vcc	Vcc
☐ Black	GROUND	GROUND
☐ Green	A	A
☐ Blue		$\overline{A}$
☐ White	B	B
☐ Pink		$\overline{B}$
☐ Yellow	Z	Z
☐ Orange		$\overline{Z}$
Shield	CASE SHIELD	

Figure C1: Data Sheet and Manual for LS Mecapion Rotary Encoder (Pg 1)

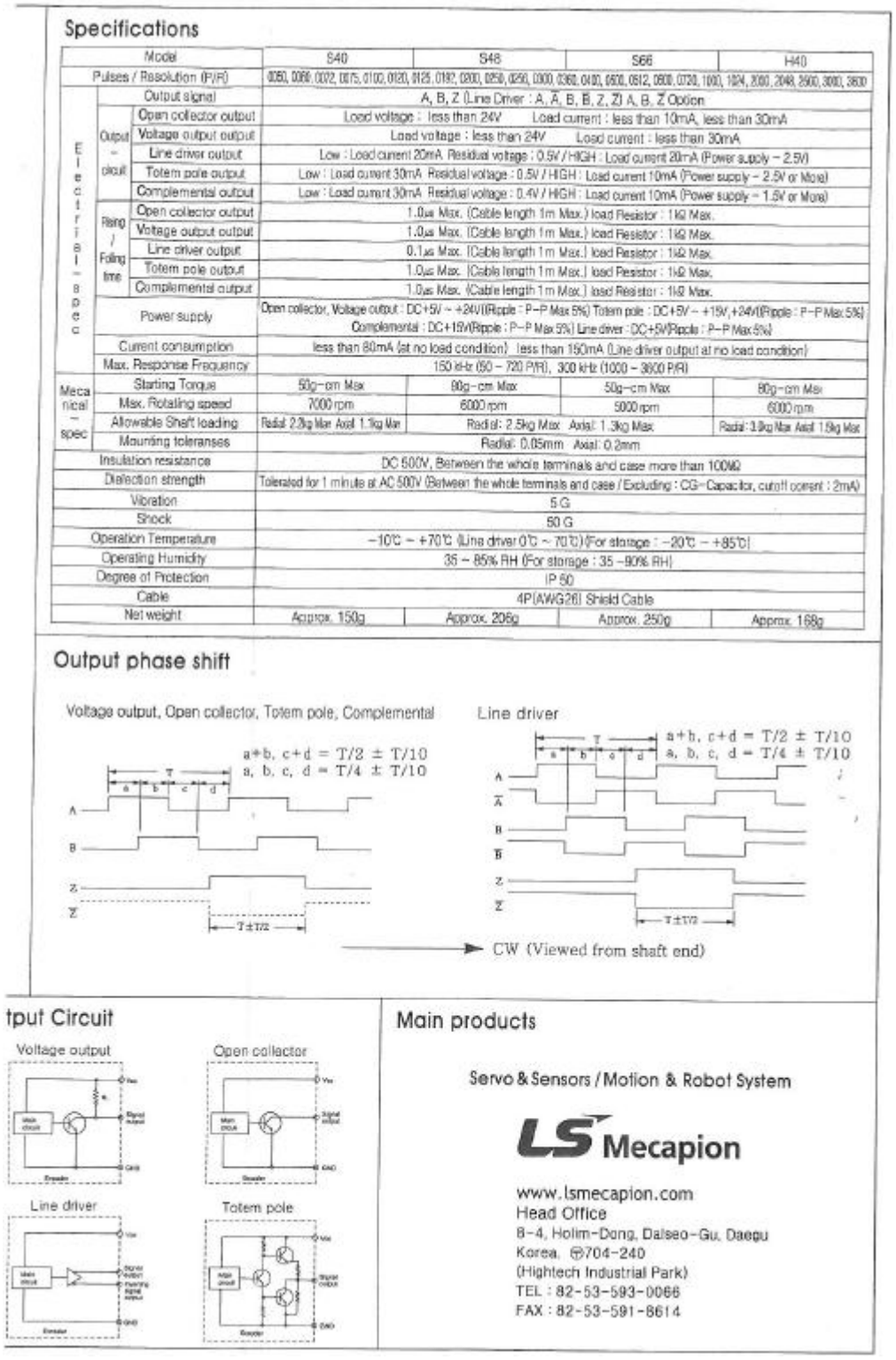

Specifications

Model			S40	S48	S66	H40
Pulses / Resolution (P/R)			0050, 0060, 0072, 0075, 0100, 0120, 0125, 0192, 0200, 0250, 0256, 0300, 0360, 0400, 0500, 0512, 0600, 0720, 1000, 1024, 2000, 2048, 2500, 3000, 3600			
Electrical-spec	Output signal		A, B, Z (Line Driver : A, Ā, B, B̄, Z, Z̄) A, B, Z Option			
	Output circuit	Open collector output	Load voltage : less than 24V Load current : less than 10mA, less than 30mA			
		Voltage output output	Load voltage : less than 24V Load current : less than 30mA			
		Line driver output	Low : Load current 20mA Residual voltage : 0.5V / HIGH : Load current 20mA (Power supply – 2.5V)			
		Totem pole output	Low : Load current 30mA Residual voltage : 0.5V / HIGH : Load current 10mA (Power supply – 2.5V or More)			
		Complemental output	Low : Load current 30mA Residual voltage : 0.4V / HIGH : Load current 10mA (Power supply – 1.5V or More)			
	Rising / Falling time	Open collector output	1.0μs Max. (Cable length 1m Max.) load Resistor : 1kΩ Max.			
		Voltage output output	1.0μs Max. (Cable length 1m Max.) load Resistor : 1kΩ Max.			
		Line driver output	0.1μs Max. (Cable length 1m Max.) load Resistor : 1kΩ Max.			
		Totem pole output	1.0μs Max. (Cable length 1m Max.) load Resistor : 1kΩ Max.			
		Complemental output	1.0μs Max. (Cable length 1m Max.) load Resistor : 1kΩ Max.			
	Power supply		Open collector, Voltage output : DC+5V ~ +24V(Ripple : P-P Max 5%) Totem pole : DC+5V ~ +15V, +24V(Ripple : P-P Max 5%) Complemental : DC+15V(Ripple : P-P Max 5%) Line driver : DC+5V(Ripple : P-P Max 5%)			
	Current consumption		less than 80mA (at no load condition) less than 150mA (Line driver output at no load condition)			
	Max. Response Frequency		150 kHz (50 ~ 720 P/R), 300 kHz (1000 ~ 3600 P/R)			
Mechanical-spec	Starting Torque		50g-cm Max	80g-cm Max	50g-cm Max	80g-cm Max
	Max. Rotating speed		7000 rpm	6000 rpm	5000 rpm	6000 rpm
	Allowable Shaft loading		Radial: 2.0kg Max Axial: 1.0kg Max	Radial: 2.5kg Max Axial: 1.3kg Max		Radial: 3.0kg Max Axial: 1.5kg Max
	Mounting toleranses		Radial: 0.05mm Axial: 0.2mm			
Insulation resistance			DC 500V, Between the whole terminals and case more than 100MΩ			
Dielectric strength			Tolerated for 1 minute at AC 500V (Between the whole terminals and case / Excluding : CG-Capacitor, cutoff current : 2mA)			
Vibration			5 G			
Shock			50 G			
Operation Temperature			-10℃ ~ +70℃ (Line driver 0℃ ~ 70℃) (For storage : -20℃ ~ +85℃)			
Operating Humidity			35 ~ 85% RH (For storage : 35 ~ 90% RH)			
Degree of Protection			IP 50			
Cable			4P(AWG26) Shield Cable			
Net weight			Approx. 150g	Approx. 206g	Approx. 250g	Approx. 168g

Output phase shift

Voltage output, Open collector, Totem pole, Complemental

a+b, c+d = T/2 ± T/10
a, b, c, d = T/4 ± T/10

Line driver

a+b, c+d = T/2 ± T/10
a, b, c, d = T/4 ± T/10

CW (Viewed from shaft end)

tput Circuit

Voltage output

Open collector

Line driver

Totem pole

Main products

Servo & Sensors / Motion & Robot System

LS Mecapion

www.lsmecapion.com
Head Office
8-4, Holim-Dong, Dalseo-Gu, Daegu
Korea. ㊥704-240
(Hightech Industrial Park)
TEL : 82-53-593-0066
FAX : 82-53-591-8614

Figure C2: Data Sheet and Manual for LS Mecapion Rotary Encoder (Pg 2)

APPENDIX D: LEM Voltage and Current Transducers

LEM

Voltage Transducer LV 25-P

I_{PN} = 10 mA
V_{PN} = 10..500 V

For the electronic measurement of voltages : DC, AC, pulsed..., with a galvanic isolation between the primary circuit (high voltage) and the secondary circuit (electronic circuit).

16084

Electrical data

I_{PN}	Primary nominal current rms		10		mA
I_{PM}	Primary current, measuring range		0 .. ± 14		mA
R_M	Measuring resistance		$R_{M\,min}$	$R_{M\,max}$	
	with ± 12 V	@ ± 10 mA	30	190	Ω
		@ ± 14 mA	30	100	Ω
	with ± 15 V	@ ± 10 mA	100	350	Ω
		@ ± 14 mA	100	190	Ω
I_{SN}	Secondary nominal current rms		25		mA
K_N	Conversion ratio		2500 : 1000		
V_C	Supply voltage (± 5 %)		± 12 .. 15		V
I_C	Current consumption		10 @ ± 15 V) + I_S		mA

Accuracy - Dynamic performance data

X_G	Overall Accuracy @ I_{PN}, T_A = 25°C	@ ± 12 .. 15 V	± 0.9		%
		@ ± 15 V (± 5 %)	± 0.8		%
ε_L	Linearity error		< 0.2		%
			Typ	Maxi	
I_O	Offset current @ I_P = 0, T_A = 25°C			± 0.15	mA
I_{OT}	Temperature variation of I_O	0°C .. + 25°C	± 0.06	± 0.25	mA
		+ 25°C .. + 70°C	± 0.10	± 0.35	mA
t_r	Response time [1] to 90 % of I_{PN} step		40		µs

General data

T_A	Ambient operating temperature		0 .. + 70	°C
T_S	Ambient storage temperature		- 25 .. + 85	°C
R_P	Primary coil resistance @ T_A = 70°C		250	Ω
R_S	Secondary coil resistance @ T_A = 70°C		110	Ω
m	Mass		22	g
	Standards		EN 50178: 1997	

Note: [1] R_t = 25 kΩ (L/R constant, produced by the resistance and inductance of the primary circuit).

Features

- Closed loop (compensated) voltage transducer using the Hall effect
- Insulated plastic case recognized according to UL 94-V0.

Principle of use

- For voltage measurements, a current proportional to the measured voltage must be passed through an external resistor R_t, which is selected by the user and installed in series with the primary circuit of the transducer.

Advantages

- Excellent accuracy
- Very good linearity
- Low thermal drift
- Low response time
- High bandwidth
- High immunity to external interference
- Low disturbance in common mode.

Applications

- AC variable speed drives and servo motor drives
- Static converters for DC motor drives
- Battery supplied applications
- Uninterruptible Power Supplies (UPS)
- Power supplies for welding applications.

Application domain

- Industrial

Figure D1: LEM Voltage Transducer LV 25-P Data Sheet (Pg 1)

LEM

Voltage Transducer LV 25-P

Isolation characteristics

V_d	Rms voltage for AC isolation test, 50 Hz, 1 min	2.5 [2]	kV
$\hat{V}_w$	Impulse withstand voltage 1.2/50 µs	16	kV
		Mini	
dCp	Creepage distance	19.5	mm
dCl	Clearance distance	19.5	mm
CTI	Comparative Tracking Index (Group IIIa)	175	

Note: [2] Between primary and secondary.

Application examples

According to EN 50178 and IEC 61010-1 standards and following conditions:

- Over voltage category OV 3
- Pollution degree PD2
- Non-uniform field

	EN 50178	IEC 61010-1
dCp, dCl, $\hat{V}_w$	Rated isolation voltage	Nominal voltage
Single isolation	1600 V	1600 V
Reinforced isolation	800 V	800 V

Safety

This transducer must be used in electric/electronic equipment with respect to applicable standards and safety requirements in accordance with the manufacturer's operating instructions.

Caution, risk of electrical shock

When operating the transducer, certain parts of the module can carry hazardous voltage (eg. primary busbar, power supply).
Ignoring this warning can lead to injury and/or cause serious damage.
This transducer is a built-in device, whose conducting parts must be inaccessible after installation.
A protective housing or additional shield could be used.
Main supply must be able to be disconnected.

Figure D2: LEM Voltage Transducer LV 25-P Data Sheet (Pg 2)

Dimensions LV 25-P (in mm. 1 mm = 0.0394 inch)

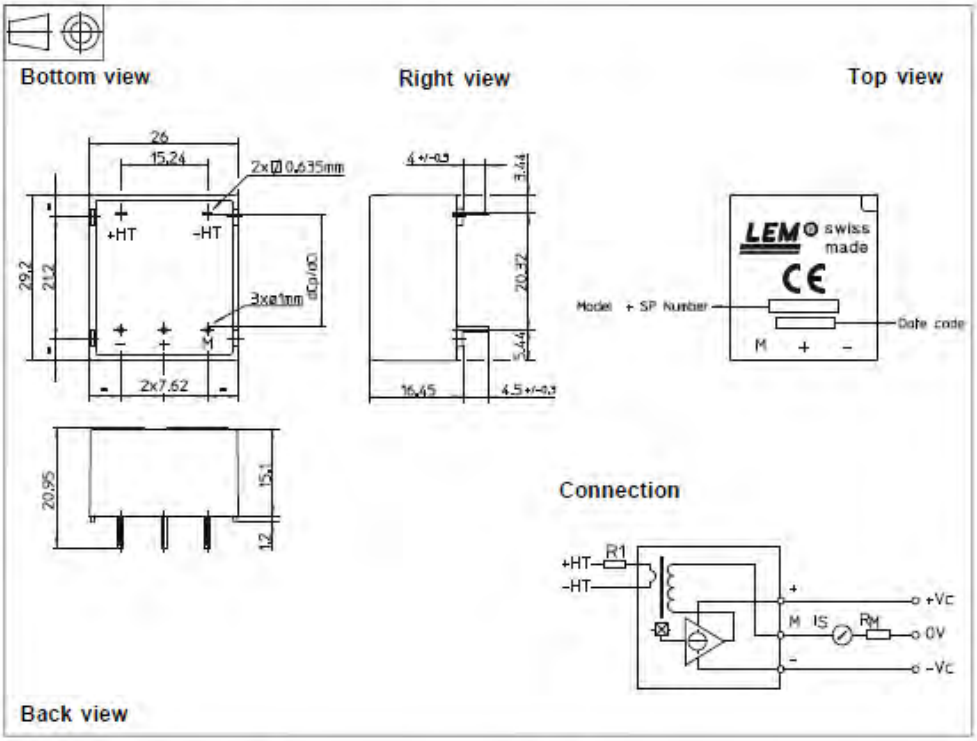

Mechanical characteristics

• General tolerance	± 0.2 mm
• Fastening & connection of primary	2 pins 0.635 x 0.635 mm
• Fastening & connection of secondary	3 pins ∅ 1 mm
• Recommended PCB hole	1.2 mm

Remarks

- I_s is positive when V_p is applied on terminal +HT.
- This is a standard model. For different versions (supply voltages, turns ratios, unidirectional measurements...), please contact us.

Instructions for use of the voltage transducer model LV 25-P

Primary resistor R_1 : the transducer's optimum accuracy is obtained at the nominal primary current. As far as possible, R_1 should be calculated so that the nominal voltage to be measured corresponds to a primary current of 10 mA.

Example: Voltage to be measured V_{PN} = 250 V
a) R_1 = 25 kΩ / 2.5 W, I_P = 10 mA Accuracy = ± 0.8 % of V_{PN} (@ T_A = +25°C)
b) R_1 = 50 kΩ / 1.25 W, I_P = 5 mA Accuracy = ± 1.6 % of V_{PN} (@ T_A = +25°C)

Operating range (recommended) : taking into account the resistance of the primary windings (which must remain low compared to R_1 in order to keep thermal deviation as low as possible) and the isolation, this transducer is suitable for measuring nominal voltages from 10 to 500 V.

Figure D3: LEM Voltage Transducer LV 25-P Data Sheet (Pg 3)

Current Transducer LA 25-NP

I_{PN} = 5-6-8-12-25 A

For the electronic measurement of currents : DC, AC, pulsed, mixed, with a galvanic isolation between the primary circuit (high power) and the secondary circuit (electronic circuit).

16080

Electrical data

I_{PN}	Primary nominal r.m.s. current			25			At
I_P	Primary current, measuring range			0 .. ± 36			At
R_M	Measuring resistance @		T_A = 70°C		T_A = 85°C		
			$R_{M\,min}$	$R_{M\,max}$	$R_{M\,min}$	$R_{M\,max}$	
	with ± 15 V	@ ± 25 At_{max}	100	320	100	315	Ω
		@ ± 36 At_{max}	100	190	100	185	Ω
I_{SN}	Secondary nominal r.m.s. current			25			mA
K_N	Conversion ratio			1-2-3-4-5 : 1000			
V_C	Supply voltage (± 5 %)			± 15			V
I_C	Current consumption			10 + I_S			mA
V_d	R.m.s. voltage for AC isolation test, 50 Hz, 1 mn			2.5			kV
V_b	R.m.s. rated voltage [1], safe separation			600			V
	basic isolation			1700			V

Accuracy - Dynamic performance data

X	Typical accuracy @ I_{PN}, T_A = 25°C		± 0.5		%
ε_L	Linearity error		< 0.2		%
			Typ	Max	
I_O	Offset current [2] @ I_P = 0, T_A = 25°C		± 0.05	± 0.15	mA
I_{OM}	Residual current [3] @ I_P = 0, after an overload of 3 x I_{PN}		± 0.05	± 0.15	mA
I_{OT}	Thermal drift of I_O	0°C .. + 25°C	± 0.06	± 0.25	mA
		+ 25°C .. + 70°C	± 0.10	± 0.35	mA
		- 25°C .. + 85°C		± 0.5	mA
		- 40°C .. + 85°C		± 1.2	mA
t_r	Response time [4] @ 90 % of I_{PN}		< 1		µs
di/dt	di/dt accurately followed		> 50		A/µs
f	Frequency bandwidth (- 1 dB)		DC .. 150		kHz

General data

T_A	Ambient operating temperature		- 40 .. + 85	°C
T_S	Ambient storage temperature		- 45 .. + 90	°C
R_P	Primary resistance per turn	@ T_A = 25°C	< 1.25	mΩ
R_S	Secondary coil resistance	@ T_A = 70°C	110	Ω
		@ T_A = 85°C	115	Ω
R_{is}	Isolation resistance @ 500 V, T_A = 25°C		> 1500	MΩ
m	Mass		22	g
	Standards		EN 50178 : 1997	

Notes : [1] Pollution class 2
[2] Measurement carried out after 15 mn functioning
[3] The result of the coercive field of the magnetic circuit
[4] With a di/dt of 100 A/µs.

Features

- Closed loop (compensated) multi-range current transducer using the Hall effect
- Insulated plastic case recognized according to UL 94-V0.

Advantages

- Excellent accuracy
- Very good linearity
- Low temperature drift
- Optimized response time
- Wide frequency bandwidth
- No insertion losses
- High immunity to external interference
- Current overload capability.

Applications

- AC variable speed drives and servo motor drives
- Static converters for DC motor drives
- Battery supplied applications
- Uninterruptible Power Supplies (UPS)
- Switched Mode Power Supplies (SMPS)
- Power supplies for welding applications.

Figure D4: LEM Current Transducer LA 25-NP Data Sheet (Pg 1)

Dimensions LA 25-NP (in mm. 1 mm = 0.0394 inch)

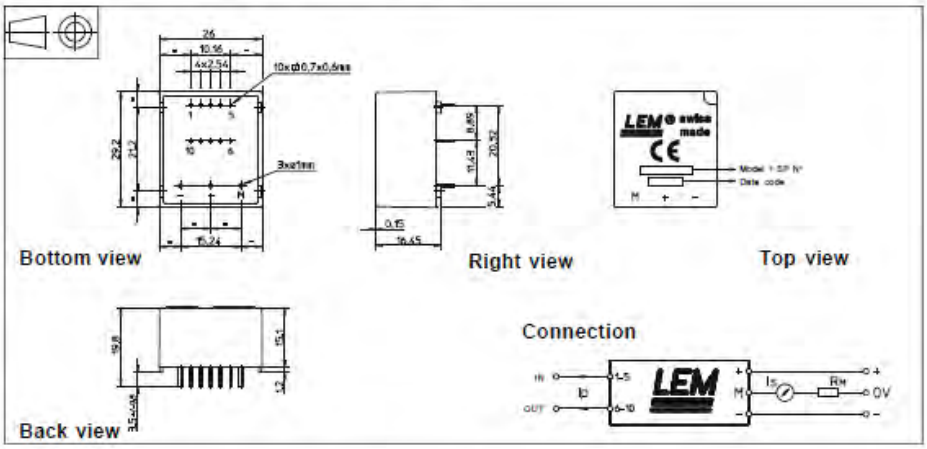

Number of primary turns	Primary current nominal I_{PN} [A]	Primary current maximum I_P [A]	Nominal output current I_{SN} [mA]	Turns ratio K_N	Primary resistance R_P [mΩ]	Primary insertion inductance L_P [µH]	Recommended connections
1	25	36	25	1/1000	0.3	0.023	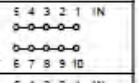
2	12	18	24	2/1000	1.1	0.09	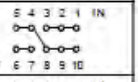
3	8	12	24	3/1000	2.5	0.21	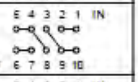
4	6	9	24	4/1000	4.4	0.37	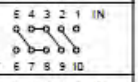
5	5	7	25	5/1000	6.3	0.58	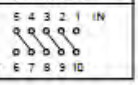

Mechanical characteristics

- General tolerance ± 0.2 mm
- Fastening & connection of primary 10 pins 0.7 x 0.6 mm
- Fastening & connection of secondary 3 pins ∅ 1 mm
- Recommended PCB hole 1.2 mm

Remarks

- I_S is positive when I_P flows from terminals 1, 2, 3, 4, 5 to terminals 10, 9, 8, 7, 6
- This is a standard model. For different versions (supply voltages, turns ratios, unidirectional measurements...), please contact us.

Figure D5: LEM Current Transducer LA 25-NP Data Sheet (Pg 2)